

# The FLAMINGO Project: Exploring the X-ray–cosmic-shear cross-correlation as a probe of large-scale structure

William McDonald,<sup>1</sup> Joop Schaye,<sup>1</sup> Konrad Kuijken,<sup>1</sup> John Helly,<sup>2</sup>

Joey Braspennincx,<sup>1,3</sup> and Matthieu Schaller,<sup>1,4</sup>

<sup>1</sup>Leiden Observatory, Leiden University, PO Box 9513, 2300 RA Leiden, the Netherlands

<sup>2</sup>Institute for Computational Cosmology, Department of Physics, University of Durham, South Road, Durham, DH1 3LE, UK

<sup>3</sup>Max-Planck-Institut für Astronomie, Königstuhl 17, D-69117 Heidelberg, Germany

<sup>4</sup>Lorentz Institute for Theoretical Physics, Leiden University, PO box 9506, 2300 RA Leiden, the Netherlands

Accepted XXX. Received YYY; in original form ZZZ

## ABSTRACT

Baryonic feedback processes associated with galaxy formation directly influence the large-scale structure by redistributing gas. Recent measurements of the kinetic Sunyaev-Zel'dovich effect and stacks of X-ray emission from optically selected galaxy clusters suggest that feedback from Active Galactic Nuclei (AGN) is more efficient at expelling gas from low-mass clusters than previously thought. The measurement of the cross-correlation between cosmic shear and diffuse X-ray emission provides a new probe of the distribution of gas in groups and clusters. We use the FLAMINGO cosmological, hydrodynamical simulations to examine the X-ray–cosmic-shear cross-correlation. The cross-correlation is most sensitive to the distribution of gas in haloes with masses  $10^{14} \leq M_{200c}/M_\odot \leq 10^{15}$ . It is sensitive to the strength of feedback, but the effects of variations in cosmology and baryonic physics are largely degenerate. We compare the FLAMINGO predictions with the cross-correlation between cosmic shear from the Dark Energy Survey and ROSAT all-sky X-ray maps. We find that, if we neglect the X-ray emission from AGN that would remain unresolved by ROSAT, then the fiducial FLAMINGO model is in excellent agreement with the data, while models with stronger or weaker feedback are ruled out. However, if we account for unresolved AGN, either using the direct FLAMINGO predictions or by abundance matching to the observed (extrapolated) AGN luminosity function, then models with stronger feedback are preferred. We conclude that to exploit the potential of the X-ray–lensing cross-correlation, it will be necessary to resolve fainter AGN, and to use external constraints to break the degeneracy between baryonic feedback and cosmology.

**Key words:** large-scale structure of Universe – cosmology: theory – methods: numerical – galaxies: clusters: general – X-rays: diffuse background – gravitational lensing: weak

## 1 INTRODUCTION

The current standard cosmological model;  $\Lambda$ CDM, is a highly successful yet relatively simple model that depicts a spatially flat universe whose energy-density is dominated by dark energy; described as a cosmological constant ( $\Lambda$ ), and a form of cold dark matter (CDM) that only interacts gravitationally. A minority of the energy density budget within the  $\Lambda$ CDM paradigm is comprised of baryons, photons, and neutrinos. The standard cosmological model reproduces a wealth of observational data to an impressive level of accuracy (for a relevant overview see Lahav & Liddle 2022). One key avenue in developing the  $\Lambda$ CDM paradigm is to exploit tensions between the best-fitting parameters of different probes, where deviations from the  $\Lambda$ CDM model may indicate shortcomings of the model (for overviews of such tensions see e.g. Abdalla et al. 2022; Peebles 2022; Perivolaropoulos & Skara 2022; Peebles 2025; Efstathiou 2025).

Modern and next-generation cosmology probes, so-called ‘Stage IV’ probes, are testing the standard model on progressively smaller

length scales, well into the non-linear regime ( $\lambda \lesssim 10$  Mpc). Part and parcel of testing  $\Lambda$ CDM is the accurate modelling of the formation and clustering of galaxies within dark matter haloes, which includes a multitude of complex physical processes such as those associated with the radiative heating and cooling of gas, the accretion of matter onto black holes (BH), Active Galactic Nuclei (AGN) feedback, the formation of stars and stellar feedback. As these baryonic ‘feedback processes’ are inherently complex in nature and can impact large-scale structure (LSS) over a large dynamical range of scales, they are a leading source of uncertainty in modelling LSS formation (see overviews by e.g. Chisari et al. 2019; Schneider et al. 2019, and references therein). Cosmological hydrodynamical simulations (and models calibrated on them) have shown that AGN feedback, which redistributes (and ejects) baryonic matter within (and out of) haloes, is a dominant source of baryonic suppression of the matter power spectrum on non-linear scales and is strongly linked to the baryonic mass fraction in clusters (e.g. van Daalen et al. 2011; Semboloni et al. 2011; Zentner et al. 2013; van Daalen et al. 2020; Schneider et al. 2019; Debackere et al. 2020; Aricò et al. 2021; Salcido et al. 2023; Schaller et al. 2025). Due to the large astrophysical uncertainties,

\* E-mail: mcdonald@strw.leidenuniv.nl

it is clear that in order to further understand baryonic feedback, a data-driven approach is of the utmost importance.

Large-volume cosmological hydrodynamical simulations self-consistently model the coupling between LSS formation and baryonic physics. However, hydrodynamic simulations have a finite resolution and therefore employ empirical subgrid models (prescriptions or recipes) to ‘mimic’ processes which originate on scales below the resolution limits and re-create their effective impact on the scales resolved by the simulation (see overviews given by e.g. [Vogelsberger et al. 2020](#); [Crain & van de Voort 2023](#)). Subgrid prescriptions typically involve free parameters that can be constrained via calibration of the hydrodynamical simulation to relevant observables. X-ray measurements provide some of the highest quality insights into the distribution and thermodynamic state of hot gas within clusters and groups, where the inferred gas mass fractions (e.g. [Eckert et al. 2016](#); [Akino et al. 2022](#); [Popesso et al. 2025](#)) have served as a benchmark for the calibration of subgrid prescriptions relevant to the efficiency of AGN feedback and, ultimately, the cluster gas mass fractions in cosmological hydrodynamical simulations (e.g., the BAHAMAS ([McCarthy et al. 2017](#)), FABLE ([Henden et al. 2018](#)) and FLAMINGO ([Schaye et al. 2023](#); [Kugel et al. 2025](#)) simulation suites).

Recent developments, such as those emanating from the joint analysis of the kinetic Sunyaev-Zel’dovich (kSZ) effect with galaxy-galaxy lensing measurements (e.g., see [McCarthy et al. 2025](#); [Bigwood et al. 2024, 2025](#); [Siegel et al. 2025a](#)) and stacks of optically selected eROSITA (X-ray observations of) galaxy groups/clusters by [Popesso et al. \(2025\)](#), suggest that AGN feedback is more efficient at expelling gas from low-mass clusters than previously thought. However, it has been shown by [Eckert et al. \(2025\)](#) that the X-ray luminosity and temperature scaling relations of low-redshift galaxy groups from the *XMM-Newton* Group AGN Project (X-GAP [Eckert et al. 2024](#)) do not advocate for an increased efficiency of AGN feedback and instead are in line with the predictions of hydrodynamical simulations calibrated on cluster gas fractions inferred from pre-eROSITA X-ray-measurements. This discrepancy could indicate shortcomings in the simulations, but it may also be a symptom of different observables (and measurements) having different systematic errors and being sensitive to different halo masses, redshifts and radii of groups/clusters (e.g., see relevant discussions in [Eckert et al. 2025](#); [Lucie-Smith et al. 2025](#); [Siegel et al. 2025b](#)). This emphasises that employing multiple, different observational probes is crucial to effectively examine how baryonic feedback influences LSS.

The angular auto- and cross-power spectra of any given observables that trace properties of the matter density field can, depending on the observables, encode a wealth of information about the role of cosmology and baryonic physics in the formation of LSS. X-ray measurements are sensitive to the thermodynamic properties and spatial distribution of gas in galaxy groups/clusters, in a manner that is complementary to other low-redshift probes such as the thermal Sunyaev-Zel’dovich (tSZ) and kSZ effect measurements. Angular auto-spectra of and cross-spectra with the observed background of soft X-ray emission from groups/clusters can provide additional constraints on cosmology and baryonic physics that are complementary to, widely adopted, adjacent low-redshift probes (e.g. with cosmic shear, tSZ and kSZ effect measurements).

In the recent literature there are only a few instances of auto- and cross-correlations utilising soft X-ray emission as probes of LSS. This is in large part due to the limited sensitivity and redshift depth of the ROSAT all-sky survey which was the only X-ray survey with sufficient on-sky coverage until the more recent eROSITA all-sky survey. Using a halo model formalism (for a recent review see e.g. [Asgari et al. 2023](#)), measured X-ray auto-correlations have been utilised to

initially place upper bounds (due to limitations of ROSAT; see [Diego et al. 2003](#)) and then set constraints (with the greater sensitivity of eROSITA) on cosmology (in particular the  $\sigma_8$  and  $S_8$  parameters<sup>1</sup>; [Lau et al. 2025](#)). Likewise, with a halo model, the measured angular cross-spectra of X-rays, the tSZ effect and weak-lensing of the cosmic microwave background (CMB) have been shown to be sensitive to changes in cosmology (in particular the  $\sigma_8$  parameter), and to provide insights into the thermodynamic properties of gas in galaxy clusters and cluster scaling relations ([Hurier et al. 2015, 2017](#)). As noted by [Hurier et al. \(2015\)](#), the uncertainty in the cosmological constraints set by X-ray–tSZ cross-spectra are large relative to other probes due to the limitations of the instruments. Furthermore, halo models constrained on the cross-spectra of X-rays and cosmic shear detected by [Ferreira et al. \(2024\)](#), and the joint analysis of X-ray, cosmic shear and tSZ cross-correlations presented by [La Posta et al. \(2025\)](#) have highlighted the sensitivity of these cross-spectra to the thermodynamic properties and spatial distribution of gas in clusters. Both [Ferreira et al. \(2024\)](#) and [La Posta et al. \(2025\)](#) find a greater level of baryonic suppression than given by cosmological hydrodynamical simulations calibrated on pre-eROSITA cluster gas fractions. This discrepancy can be reduced by increasing the strength of AGN feedback within the simulations, although not to the extent suggested by recent kSZ measurements. Additionally, X-ray auto- and cross-spectra have been forecast with semi-analytic models, halo occupation distribution (HOD) and halo model formalisms (e.g. [Hurier et al. 2014](#); [Singh et al. 2016](#); [Shirasaki et al. 2020](#); [Lakey & Huffenberger 2023](#)). They have also been measured from small patches of the sky, however this leads to larger uncertainties on any extracted constraints due to cosmic variance (e.g. [Hajian et al. 2013](#); [Kolodzig et al. 2016, 2017](#); [Zhou et al. 2022](#)).

In this work, we specifically focus on the cross-correlation of diffuse soft X-ray emission and cosmic shear. [Ferreira et al. \(2024\)](#) presented the first – and, at present, only – detection of this cross-correlation, using maps from the ROSAT all-sky survey (RASS; [Voges 1993](#); [Voges et al. 1999](#)) and cosmic shear data from the Dark Energy Survey year-3 data release (DES-Y3; [Gatti et al. 2021](#); [Abbott et al. 2022](#)). This probe is of particular interest as it may break degeneracies between the effects of cosmology and baryonic physics given it is a measure of how hot gas (its spatial distribution and energy density) traces the underlying total matter field. Moreover, this probe is well positioned to further contribute to the discussion of the strength of AGN feedback and cluster gas fractions indicated by recent kSZ measurements and stacks of optically selected eROSITA clusters.

A potential major source of uncertainty in the observed X-ray–cosmic-shear cross-correlation (and for other X-ray auto- and cross-spectra) is contamination by unresolved point sources, particularly the X-ray emission from unresolved AGN. Large area X-ray surveys and measurements of clusters are highly susceptible to contamination from unresolved AGN and it is commonly accepted that AGN dominate the diffuse X-ray background (e.g. [Brandt & Hasinger 2005](#); [Boller et al. 2016](#); [Comparat et al. 2019](#); [Helgason et al. 2014](#); [Seppi et al. 2022](#); [Brandt & Yang 2022](#); [Comparat et al. 2023](#)). This poses the question of how much of the detected signal in the X-ray–cosmic-shear cross-correlation can be attributed to X-ray emission from unresolved AGN? This issue is not discussed by [Ferreira et al. \(2024\)](#). However, [La Posta et al. \(2025\)](#) found that unresolved AGN account

<sup>1</sup>  $S_8 = \sigma_8 \sqrt{\Omega_m/0.03}$  where;  $\Omega_m$  is the present day matter density and  $\sigma_8$  is the variance of the linear matter density field averaged over spheres of radius  $8h^{-1}$  Mpc extrapolated to the present day (redshift  $z = 0$ ).

for  $\approx 20\%$  of the X-ray–cosmic-shear cross-correlation and that X-ray emission from AGN is necessary to prevent internal tensions between their halo models constrained on X-ray, tSZ and cosmic shear data. Similarly, [Comparat et al. \(2025\)](#), used a halo model formalism to demonstrate that unresolved AGN can have a noticeable impact on X-ray–galaxy-clustering cross-correlations, specifically on small scales ( $< 80$  kpc). However, [Lau et al. \(2025\)](#) found, with a HOD model (following [Comparat et al. 2023](#)), that contamination from unresolved AGN has only a  $< 10\%$  effect on their eROSITA X-ray auto-correlation.

In this work we use full-sky lightcones from the FLAMINGO<sup>2</sup> suite of cosmological hydrodynamical simulations ([Schaye et al. 2023; Kugel et al. 2023](#)) to examine the efficacy of the X-ray–cosmic-shear cross-correlation as a probe of LSS and compare, for the first time, the predictions from self-consistent hydrodynamical simulations to the X-ray–cosmic-shear cross-correlation observed by [Ferreira et al. \(2024\)](#). The FLAMINGO suite includes hydrodynamical simulations with various box sizes, resolutions, different cosmologies, and systematic variations in the strength of baryonic feedback (both stellar and AGN feedback). Using the X-ray–cosmic-shear cross-correlations computed from the full-sky lightcones of FLAMINGO, we explore the sensitivity of this probe to changes in cosmology and baryonic feedback. We demonstrate that the X-ray–cosmic-shear cross-correlation is especially sensitive to changes in AGN feedback strength, but that this effect is largely degenerate with respect to changes in cosmology. Additionally, we explore the impact of the X-ray emission from unresolved AGN on the X-ray–cosmic-shear cross-correlation. Using an abundance matching approach, we estimate the X-ray emission from AGN and demonstrate that the X-ray emission from unresolved AGN can have a significant impact. From comparisons to the measurements of [Ferreira et al. \(2024\)](#), we show that FLAMINGO favours cluster gas fractions lower than derived from pre-eROSITA X-ray data, suggesting that AGN feedback is stronger than in the fiducial FLAMINGO model. However, we find that, depending on the level of contamination by unresolved AGN, both the fiducial model and the stronger feedback models that are preferred by observations of the kSZ effect and optically selected eROSITA clusters can be consistent with the measurements of [Ferreira et al. \(2024\)](#). On the other hand, weaker feedback, resulting in cluster gas fractions smaller than in the fiducial model, is ruled out.

This paper is organized as follows: In §2 we introduce the FLAMINGO suite of simulations and outline the lightcone data products that were used in this work. In §3 we describe our 2D map based approach for computing X-ray–cosmic-shear cross-correlations from simulated weak-lensing and X-ray all-sky maps. In §4 we present our main results, which include: the predicted cross-correlations, the dependence of said cross-correlations on cosmology and baryonic feedback, the impact of the X-ray emission from unresolved AGN on the cross-correlation, and comparisons to the observational data. In §5 we discuss our results in the context of other low-redshift probes and examine how to further mitigate the effects of contamination from unresolved AGN, before concluding in §6.

## 2 SIMULATION DATASETS

In this section, we introduce the FLAMINGO (Full-hydro Large-scale structure simulations with All-sky Mapping for the Interpretation of Next Generation Observations)

<sup>2</sup> Full-hydro Large-scale structure simulations with All-sky Mapping for the Interpretation of Next Generation Observations.

tation of Next Generation Observations) suite of simulations used in this paper (§2.1) and provide an overview of the different data structures of FLAMINGO lightcones utilised in this study (§2.2).

### 2.1 FLAMINGO simulations

Here we provide a short overview of the FLAMINGO simulations, for a complete description of the FLAMINGO simulations and their calibration methods we refer the reader to [Schaye et al. \(2023\)](#) and [Kugel et al. \(2023\)](#), respectively.

The FLAMINGO suite contains both hydrodynamical (N-body+Smooth Particle Hydrodynamic (SPH)) and gravity-only (N-body) cosmological simulations ([Schaye et al. 2023](#)) run with the open-source simulation code SWIFT<sup>3</sup> ([Schaller et al. 2024](#)) and the SPHENIX ([Borrow et al. 2022](#)) SPH scheme. Massive neutrinos are included as particles in SWIFT via the  $\delta f$  method ([Elbers et al. 2021](#)). Initial conditions are generated by MONOFONIC ([Hahn et al. 2021](#)). The FLAMINGO suite includes simulations with different cosmological volumes and mass resolutions, in this work we focus on the (1 Gpc)<sup>3</sup> volume (denoted as ‘L1’) intermediate resolution (labelled as ‘m9’, the number indicates  $\log_{10}$  of the mean baryonic particle mass) hydrodynamic simulations, hereafter referred to as L1\_m9. For the remainder of this paper, unless specified otherwise, L1\_m9 implies that the fiducial cosmological and hydrodynamical models have been assumed. The hydrodynamical simulations within FLAMINGO are calibrated on pre-eROSITA<sup>4</sup>, low-redshift cluster gas fractions ( $f_{\text{gas}}$ ) at  $R_{500c}$  and galaxy stellar mass functions ( $M^*$ ) at  $z = 0$  via tuning the AGN and stellar feedback through a machine learning assisted approach. The mass range that the cluster gas fraction is calibrated over has a lower limit of  $M_{500c} = 10^{13.5} M_{\odot}$  and a resolution dependent upper limit. The upper limit for the low (m10), intermediate (m9) and high (m8) resolutions are  $10^{13.73}, 10^{14.46}$  and  $10^{14.53} M_{\odot}$  respectively. Conversely, the stellar mass range used for the calibration of the galaxy stellar mass function has a constant upper limit of,  $M_* = 10^{11.5} M_{\odot}$  and a resolution dependent lower limit. For the low (m10), intermediate (m9) and high (m8) resolutions this is  $M_* > 10^{11.17}, 10^{9.92}$  and  $10^{8.67} M_{\odot}$ . We refer the reader to [Kugel et al. \(2023\)](#) for a complete description of the calibration methods.

The FLAMINGO hydrodynamical models include sub-grid prescriptions of radiative cooling ([Ploeckinger & Schaye 2020](#)), star formation ([Schaye & Dalla Vecchia 2008](#)), stellar mass loss ([Wiersma et al. 2009; Schaye et al. 2015](#)), supernova feedback ([Schaye & Dalla Vecchia 2008; Chaikin et al. 2022](#)), seeding and black hole growth ([Springel et al. 2005; Bahé et al. 2022](#)). Additionally, the FLAMINGO suite contains two different modes of AGN feedback: the fiducial thermally-driven AGN feedback ([Booth & Schaye 2009](#)) and the alternative kinetic AGN jet feedback ([Huško et al. 2022](#)). Note that, importantly for this study, the galaxy clusters from the fiducial FLAMINGO simulation have temperature, density, pressure, and entropy profiles that reproduce those derived from X-ray measurements (see [Braspenning et al. 2024](#)).

<sup>3</sup> Publicly available at <https://swift.strw.leidenuniv.nl/>

<sup>4</sup> The cluster gas mass fractions inferred from the stacking of optically selected eROSITA clusters are significantly lower than those FLAMINGO has been calibrated on for haloes with masses in the range of  $10^{13.5} \lesssim M_{500c}/M_{\odot} \lesssim 10^{14.5}$  ([Popesso et al. 2025](#))

### 2.1.1 Cosmology Variations

The assumed fiducial  $\Lambda$ CDM cosmology includes a single massive neutrino species, with a minimal neutrino mass  $\Sigma m_\nu = 0.06$  eV and two massless species. The cosmological parameters are derived from the maximum posterior likelihood values of the Dark Energy Survey Year 3 (DES-Y3)  $3 \times 2\text{pt} + \text{All ExternalConstraints}$  (see Abbott et al. 2022). The fiducial cosmological model is labelled as D3A. Table 1 (reproduced from Table 4 of Schaye et al. 2023) presents the parameters associated with the fiducial, D3A, cosmological model along with those of the six other alternate cosmological models used in this work.

Of the five cosmologies considered, three are variations of the best-fitting model of Planck Collaboration et al. (2020). The Planck Collaboration et al. (2020) model that adopts the minimum neutrino mass,  $\Sigma m_\nu = 0.06$  eV, is labelled ‘Planck’. We include two additional models based on the FLAMINGO Planck cosmology, where the massive neutrino species has a mass of  $\Sigma m_\nu = 0.24$  eV and 0.48 eV, whilst all other parameters are fixed to the values of the Planck model, except  $\Omega_{\text{CDM}}$ , which is reduced to accommodate the increased neutrino mass whilst maintaining  $\Omega_m$ . We denote these models as ‘PlanckNu0p24Fix’ and ‘PlanckNu0p48Fix’ (as described in Elbers et al. 2025), the neutrino mass (in eV) is indicated by the number value of each label.

Lastly, we include a ‘lensing cosmology’ from Amon et al. (2023) that has a reduced amplitude of the matter power spectrum, giving a lower  $S_8$  value,  $S_8 = 0.766$ , compared to 0.815 of the fiducial D3A cosmology and 0.833 from Planck. We denote this low  $S_8$  simulation as ‘LS8’. The LS8 simulation has been shown, at the power spectrum level, by Amon et al. (2023) to be consistent with observations of galaxy clustering from BOSS DR12 (Reid et al. 2016) and galaxy-galaxy lensing from DES-Y3 (Abbott et al. 2022), the Hyper Suprime-cam Survey (HSC; Aihara et al. 2018) and the Kilo Degree Survey 1000 square degree sample (KiDS-1000 Kuijken et al. 2019).

### 2.1.2 Baryonic feedback Variations

Variations of the fiducial model for baryonic feedback are created via shifting  $f_{\text{gas}}$  and  $M^*$  by a multiple of the uncertainty ( $\sigma$ ) ascribed to the value ( $f_{\text{gas}}$  and  $M^*$ ) and then re-calibrating the model to fit these new points. We denote these variations from the fiducial values with  $f_{\text{gas}} \pm N\sigma$  and  $M^* \pm N\sigma$ .

We consider all the hydrodynamic variations for L1\_m9 specified in Tables 1 and 2 of Schaye et al. (2023). We utilise simulations with  $N\sigma$  variations from the fiducial model in the cluster gas fraction; ‘ $f_{\text{gas}} \pm 2\sigma$ ’, ‘ $f_{\text{gas}} \pm 4\sigma$ ’, ‘ $f_{\text{gas}} \pm 8\sigma$ ’, stellar mass function: ‘ $M^* - \sigma$ ’, and a combination of the two; ‘ $M^* - \sigma - f_{\text{gas}} - 4\sigma$ ’. Furthermore, we incorporate simulations with the AGN jet feedback models (as opposed to the fiducial thermal feedback model) calibrated on the fiducial cluster gas fractions: ‘Jet’. We also include two simulations introduced by McCarthy et al. (2025); the first combines the lensing cosmology with strong baryonic feedback (‘LS8\_fgas–8 $\sigma$ ’), whilst the other is an Adiabatic (‘no-cooling’) simulation using the fiducial D3A cosmology. The LS8\_fgas–8 $\sigma$  simulation combines the LS8 cosmological (see §2.1.1) model with sub-grid parameters calibrated to reproduce a significantly reduced cluster gas fraction,  $f_{\text{gas}} - 8\sigma$ . The intention of this simulation is to explore degeneracies between astrophysical parameters and cosmology through comparing it to both the LS8 and fgas–8 $\sigma$  variations. The ‘no-cooling’ simulation, sets the net radiative heating+cooling rate to zero for gas where the net rate would be negative. The consequence is that there is no

cooling, star formation, BHs and feedback present in the simulation. This simulation is non-physical and serves as an extreme boundary condition.

## 2.2 FLAMINGO Lightcones

A key feature of FLAMINGO is the lightcone output, which can be used to construct all-sky maps and is therefore ideal for our X-ray–shear cross-correlations. These lightcones are built on-the-fly (OTF) and store information in two formats: either as raw particle data (i.e. akin to a simulation snapshot) or compiled as HEALPix maps (Górski et al. 2005) for various observable features (e.g. X-ray photon count rates, total mass, gas temperature) along the line of sight. These lightcones are constructed by recording particles crossing the past lightcone of an observer (excluding a sphere with a radius of 3 Mpc centred on the observer). The crossing particles are stored in the particle lightcone (PLC) and HEALPix maps are constructed by projecting said particles’ properties onto the sky in concentric spherical shells that are equally spaced in redshift ( $\Delta z_{\text{shell}} = 0.05$ ). These HEALPix maps have  $N_{\text{side}} = 16384$ , corresponding to  $12 \times (N_{\text{side}})^2$  pixels with a maximum radius of 13.46 arcseconds. We point the reader to Appendix A of Schaye et al. (2023) for further information on lightcone generation and the construction of HEALPix maps within FLAMINGO. In this work, we utilise both forms of the lightcones: the shells of HEALPix maps and the particle data.

The box sizes of the L1\_m9 simulations are not large enough to contain the cosmological volume of a singular lightcone over the redshift ranges required for this work. To counter this, when the comoving radius of the lightcone surpasses the box side length, the box is replicated, which leads to the same structures being observed multiple times, albeit at different cosmological times and thus at different stages in their evolution. This can increase the correlation within full-sky maps on large scales. To account for this box replication we rotate the lightcone shell (either the HEALPix maps or the particle’s coordinates on the sky) via a randomised latitude and longitude each time the lightcone’s diameter crosses a single box length (e.g. Bernyk et al. 2016; Upadhye et al. 2024; Broxterman et al. 2024).

### 2.2.1 X-ray models and X-ray lightcone data

The FLAMINGO hydrodynamical datasets contain both X-ray intrinsic-energy and photon flux estimates for gas particles in three different energy bands; eROSITA low (0.2–2.3 keV), eROSITA high (2.3–8.0 keV) and ROSAT (0.5–2 keV). In this paper we make use of the ROSAT band. The lightcones contain all-sky maps (in shells of width  $\Delta z_{\text{shell}} = 0.05$ ) of each energy band for redshift,  $z \leq 3$ . The individual photon flux maps are generated –the same way as all smoothed HEALPix maps (see appendix A of Schaye et al. 2023)– from the X-ray luminosities of ‘hot’ gas particles, as detailed by Braspenning et al. (2024), using emissivity tables from CLOUDY (version 17.02 Ferland et al. 2017) and are consistent with the radiative cooling rates of Ploeckinger & Schaye (2020) that are used in the FLAMINGO simulations. X-ray luminosities are only determined for ‘hot’ gas particles that have not been recently heated by AGN and are not star-forming (i.e. the star formation rate is zero). Gas particles that have been recently heated by AGN feedback can temporarily have extreme temperatures and densities, leading to these particles being unrealistically X-ray bright. A gas particle is considered ‘hot’ or of a relevant temperature for X-ray clusters if it has a temperature ( $T$ ) in the range  $10^5 \text{ K} < T < 10^{9.5} \text{ K}$ . Gas particles are considered

**Table 1.** The values of the cosmological parameters used in different simulations. The columns list the prefix used to indicate the cosmology in the simulation name (note that, for brevity the prefix ‘D3A’ that indicates the fiducial cosmology is omitted from the simulation identifiers); the dimensionless Hubble constant,  $h$ ; the total matter density parameter,  $\Omega_m$ ; the dark energy density parameter,  $\Omega_\Lambda$ ; the baryonic matter density parameter,  $\Omega_b$ ; the sum of the particle masses of the neutrino species,  $\sum m_\nu c^2$ ; the amplitude of the primordial matter power spectrum,  $A_s$ ; the power-law index of the primordial matter power spectrum,  $n_s$ ; the amplitude of the initial power spectrum parametrized as the r.m.s. mass density fluctuation in spheres of radius  $8 h^{-1}$  Mpc extrapolated to  $z = 0$  using linear theory,  $\sigma_8$ ; the amplitude of the initial power spectrum parametrized as  $S_8 \equiv \sigma_8 \sqrt{\Omega_m/0.3}$ ; the neutrino matter density parameter,  $\Omega_\nu \cong \sum m_\nu c^2/(93.14 h^2 \text{ eV})$ . Note that the values of the Hubble and density parameters are given at  $z = 0$ .

Identifier	$h$	$\Omega_m$	$\Omega_\Lambda$	$\Omega_b$	$\sum m_\nu c^2$	$A_s$	$n_s$	$\sigma_8$	$S_8$	$\Omega_\nu$
D3A	0.681	0.306	0.694	0.0486	0.06 eV	$2.099 \times 10^{-9}$	0.967	0.807	0.815	$1.39 \times 10^{-3}$
Planck	0.673	0.316	0.684	0.0494	0.06 eV	$2.101 \times 10^{-9}$	0.966	0.812	0.833	$1.42 \times 10^{-3}$
PlanckNu0p24Fix	0.673	0.316	0.684	0.0494	0.24 eV	$2.101 \times 10^{-9}$	0.966	0.769	0.789	$5.69 \times 10^{-3}$
PlanckNu0p48Fix	0.673	0.316	0.684	0.0494	0.48 eV	$2.101 \times 10^{-9}$	0.966	0.709	0.728	$11.4 \times 10^{-3}$
LS8	0.682	0.305	0.695	0.0473	0.06 eV	$1.836 \times 10^{-9}$	0.965	0.760	0.766	$1.39 \times 10^{-3}$

recently heated if they have been directly heated by energy from AGN feedback within the last 15 Myr and have a temperature of  $10^{-1} \Delta T_{\text{AGN}} < T < 10^{0.3} \Delta T_{\text{AGN}}$ , where (in the fiducial hydrodynamical model)  $\Delta T_{\text{AGN}} = 10^{7.78}$  K and is a calibrated sub-grid parameter for the thermal mode AGN feedback temperature.

## 2.2.2 Halo-lightcones and Halo catalogues

In addition to the PLC data and shells of all-sky maps, we make use of the FLAMINGO halo-lightcones. The FLAMINGO suite employs a modified version of the Hierarchical Bound-Tracing (HBT+, Han et al. 2012, 2018) structure finding scheme; HBT-HERONS as introduced by Forouhar Moreno et al. (2025). Furthermore, the FLAMINGO data products contain a larger catalogue of halo properties computed using the Spherical Overdensity Aperture Processor (SOAP, McGibbon et al. 2025). The SOAP catalogues contain properties measured from either particles bound to subhaloes or all particles within apertures of a specified radius about a given subhalo. The halo-lightcones link both HBT-HERONS and SOAP catalogues to on-sky coordinates, which allows for a comparison between a subhalo’s three-dimensional quantities (from the simulation snapshots) and the two-dimensional, on-sky, counterparts (e.g. as seen in the lightcones). The halo-lightcones are constructed (using the LIGHTCONEIO<sup>5</sup> package) by linking each HBT-HERONS output from a given snapshot to the PLC via a tracer particle. In this case the tracer particle is the most bound black hole (BH) particle in a subhalo that exists in both the preceding and proceeding snapshots<sup>6</sup>. For each snapshot (and its associated HBT-HERONS catalogue) we read in a spherical shell of the BH PLC that spans half the redshift range to the adjacent snapshots, then for each subhalo in the HBT-HERONS catalogue, each time its tracer particle appears in the PLC the subhalo is placed onto the lightcone at the position of the particle. For redshifts  $z \leq 3$  the snapshots and therefore the halo-lightcones have the same output cadence as the lightcone shells;  $\Delta z = 0.05$ . The same rotation scheme as mentioned above (§2.2) is applied to the halo-lightcones.

<sup>5</sup> <https://github.com/jchelly/LightconeIO>

<sup>6</sup> This choice is made to handle the fact that most subhaloes contain multiple BHs. If the most bound BH is not present in the proceeding snapshot, then the second most bound BH is identified as the tracer particle. This iterative searching for the tracer particle continues until a suitable BH is identified.

## 3 METHODS: COMPUTATION OF FLAMINGO OBSERVABLES AND CROSS-CORRELATIONS

In this section we describe the various simulated all-sky maps used in this work and provide an overview of the 2D map based approach we use to compute the X-ray–cosmic-shear cross-correlation,  $C_\ell^{X\kappa}$ . In this paper we assume the observed diffuse X-ray background ( $\mathbf{X}(\theta)$ ) is comprised of X-ray emission from: only hot gas, observationally unresolved AGN or a combination of both hot gas and unresolved AGN. We assume that XRBs (X-ray binaries) have a negligible impact on the measured X-ray–cosmic-shear cross-correlation (see Appendix A) and given that the total X-ray luminosity from point sources is dominated by AGN (e.g., see relevant discussions in Comparat et al. 2025). Additionally, we do not consider any effects related to the lensing of X-ray emission from hot gas or point sources (e.g., see relevant discussions in Yang et al. 2025). In §3.1 we describe how each of the simulated X-ray observables are constructed and introduce a simple model to estimate the intrinsic photon flux expected from AGN from BH particles within a lightcone. In §3.2 we describe the different populations of BHs used in this paper and in §3.3 we provide the framework required to estimate the various X-ray–cosmic-shear cross-correlations utilised in this study.

### 3.1 X-ray all-sky maps

#### 3.1.1 Hot gas all-sky maps

Two of the core goals of this paper are predicated on making comparisons between the X-ray–cosmic-shear cross-correlation predicted by the FLAMINGO simulation suite and the measurements presented by Ferreira et al. (2024). In order to make these comparisons the simulated X-ray all-sky maps need to reflect the RASS data (ROSAT all-sky survey Voges 1993; Voges et al. 1999) utilised by Ferreira et al. (2024). As such, the diffuse gas component of the FLAMINGO X-ray all-sky maps must, at a bare minimum, meet two basic requirements: first, it needs to be in the same energy band (0.5–2 keV) and second, it must account for the effective detector area along with the beam of ROSAT. FLAMINGO’s on-the-fly lightcones, as outlined in §2.2.1, meet the first requirement, but not the second.

To account for the effective detector area of ROSAT, we construct a new ‘ROSAT-like’ set of all-sky photon flux HEALPix maps in the ROSAT soft X-ray band (0.5–2 keV) from the gas particle data. For each redshift shell ( $\Delta z_{\text{shell}} = 0.05$ ) we simply recompute the intrinsic photon flux of each gas particle using a slightly modified approach to that used in the FLAMINGO model (i.e. Braspenning et al. 2024), by convolving the emitted photon energy with the ef-

fective area of the ROSAT detector response matrix<sup>7</sup>. For each recomputed shell we create a HEALPix map using the same method as all other smoothed maps in FLAMINGO (see appendix A of Schaye et al. 2023), except we correct the scale used to determine whether X-ray emission from a gas particle should be smoothed over multiple pixels or be contained within a singular pixel. Note that this correction is inconsequential for the results of this paper (see Appendix A). We refer to these new maps (lightcones and resultant cross-correlations) as ‘ROSAT-like’ given that they account for the effective area of the detector. The ROSAT-like all-sky maps give the photon flux in terms of photon s<sup>-1</sup> (pixel area)<sup>-1</sup>, whereas the base, non-instrument specific photon flux all-sky maps have units of photon s<sup>-1</sup> cm<sup>-2</sup> (pixel area)<sup>-1</sup>. Throughout this paper, unless stated otherwise, the reader can assume that all comparisons to observations are made with the ROSAT-like lightcones, all-sky maps and cross-correlations (convolved with the ROSAT response matrix).

We construct a synthetic all-sky map of the soft X-ray emission from gas ( $\mathbf{X}_{\text{gas}}(\theta)$ ) by integrating along the line of sight,

$$\mathbf{X}_{\text{gas}}(\theta) = \int_0^{\chi(z_{\text{max}})} \mathbf{x}(\chi, \theta) d\chi, \quad (1)$$

where  $\mathbf{x}(\chi, \theta)$  is the photon count rate on the sky at a given comoving distance from the observer,  $\chi$ . When computing  $\mathbf{X}_{\text{gas}}(\theta)$ , we downgrade (or create, in the case of the ROSAT-like maps) each of the constituent  $\mathbf{x}(\chi, \theta)$  maps from  $N_{\text{side}} = 16384$  to  $N_{\text{side}} = 4096$  (corresponding to an angular resolution of 0.85 arcmin) using the ‘ud\_grade’ function from the HEALPix package. This downgrading is done for the sake of computational efficiency, whilst maintaining sufficient angular resolution to compare to the observational data.

In the process of integrating along the line of sight, we rotate each shell,  $\mathbf{x}(\chi, \theta)$ , on the sky (as given in §2.2) via the ROTATOR functions within the HEALPix package and set a maximum multipole (or minimum angular scale) of  $\ell_{\text{max}} = 2N_{\text{side}}$ . This scale cut is made to mitigate the additional noise over smaller angular scales (larger  $\ell$  values) that is introduced by rotating the  $\mathbf{x}(\chi, \theta)$  maps. The remaining angular scales,  $\ell \leq 2N_{\text{side}}$ , where  $N_{\text{side}} = 4096$ , are more than sufficient for this study.

Lastly, we note two limitations of gas particle data contained within the PLC of the (1Gpc)<sup>3</sup> FLAMINGO simulations. Firstly, the lightcones of the Planck, LS8 and massive neutrino simulations do not contain any gas particle data. Secondly, for the remaining simulations, the redshift range of the gas particle data stored in the PLC varies with the simulations resolution and box size. The L1\_m9 PLC contains all gas particles for redshifts  $0 \lesssim z \lesssim 0.25$ , whilst only storing the X-ray bright gas particles between redshifts  $0.25 \lesssim z \lesssim 0.5$  (Appendix A of Schaye et al. 2023). Given the shallow redshift depth of the RASS data, the redshift range of  $0 \lesssim z \lesssim 0.5$  is more than sufficient for this study, as verified in Fig. 3.

### 3.1.2 AGN all-sky maps

To account for the X-ray emission from AGN, we estimate the photon flux (or photon count rate) from the BH (AGN) particles within the PLC and construct an AGN ‘ROSAT-like’ all-sky map,  $\mathbf{X}_{\text{AGN}}(\theta)$ , as done for the hot gas in §3.1.1.

<sup>7</sup> FLAMINGO outputs a single artificial wide band, not a spectrum as would be observed, hence only the effective area per incident photon energy is required. We adopt the effective area information from the publicly available ‘pspc’ ROSAT response matrices (the main detector for the data utilised in Ferreira et al. 2024): <https://heasarc.gsfc.nasa.gov/FTP/caldb/data/rosat/pspc/cpf/matrices/>

The photon count rate specific to ROSAT ( $\dot{n}_{\text{ROSAT}}$ ) is determined by integrating the expected AGN photon emission spectra ( $f_E$ ) over the soft band (0.5 - 2 keV) convolved with the ROSAT response matrix,

$$\dot{n}_{\text{ROSAT}} = \int_{(0.5\text{keV})(1+z)}^{(2.0\text{keV})(1+z)} \mathbf{A}_{\text{eff}} \left( \frac{E_\gamma}{1+z} \right) \frac{f_E}{E_\gamma} dE_\gamma. \quad (2)$$

Here  $E_\gamma$  is the energy of an emitted photon in the rest-frame (the photon energy measured by the emitting source),  $z$  is the redshift at which the BH entered the lightcone, and  $A_{\text{eff}}$  is the effective area of the ROSAT response matrix, which depends on the photon energy in the observer-frame (the photon energy measured at the observer),  $E_\gamma/(1+z)$ . We assume a power law for the AGN emission spectra (in the rest-frame),  $f_E \propto (E_\gamma \text{ keV})^{1-\Gamma}$ , normalised by the total intrinsic X-ray flux in the rest-frame ( $f_{x, \text{AGN}}$ ) and we adopt a typical value for the photon index<sup>8</sup>  $\Gamma = 1.8$  (e.g. Boller et al. 2016; Faucher-Giguère 2020).

For each AGN point source we compute the total intrinsic X-ray flux ( $f_{x, \text{AGN}}$ ) from the estimated total X-ray luminosity ( $L_x$ ) given  $f_{x, \text{AGN}} = L_x/(4\pi\chi^2(1+z)^2)$  erg/cm<sup>2</sup>s, where  $\chi$  is the comoving distance from the BH to the observer. Since  $L_x$  is not directly measurable from the BH particles, we instead compute the total bolometric luminosity ( $L_{\text{bol}}$ ) of each BH particle and then estimate  $L_x$  as  $L_x = L_{\text{bol}}/K(L_{\text{bol}})$ , where  $K(L_{\text{bol}})$  is a bolometric correction factor. We adopt the correction function (equation 5) and the best fitting parameters (Table 1) of Shen et al. (2020). Additionally, to allow for a wider range of bolometric luminosities than fit by Shen et al. (2020), we extend the bolometric correction function by ensuring the function asymptotes towards  $K(L_{\text{bol}} = 10^{42})$  and  $K(L_{\text{bol}} = 10^{49})$  for  $L_{\text{bol}} < 10^{42}$  erg s<sup>-1</sup> and  $L_{\text{bol}} > 10^{48}$  erg s<sup>-1</sup> respectively (following the correction functions given by López et al. (2024) and Zou et al. (2024)). We extend the lower bound of the function to include the extremely low-luminosity AGN, which, as a whole, may be consequential to the final all-sky X-ray map in the form of unresolved AGN contamination. Additionally, the asymptotic upper bound prevents an exponential and potentially non-physical increase in X-ray luminosities for BHs with extremely high bolometric luminosities.

We subdivide the PLC into shells of equal width in redshift,  $\Delta z_{\text{shell}} = 0.05$ , for  $z \leq 8$  and create ROSAT-like AGN photon flux ( $\dot{n}_{\text{ROSAT}}$ ) maps for each shell, as done in §3.1.1. Note that we treat each BH particle (or AGN) as a point source and do not smooth the estimated  $\dot{n}_{\text{ROSAT}}$  values over neighbouring pixels within each HEALPix map. We then sum over each of these maps (as in §3.1.1, see equation 1) to compute a total all-sky map of the AGN soft X-ray photon count rate:  $\mathbf{X}_{\text{AGN}}(\theta)$ . We physically rotate the BH particles’ on-sky coordinates (with the same rotation matrices used for the gas particles) to avoid replication of the simulation box.

### 3.1.3 AGN contaminated X-ray all-sky maps

It is well understood that AGN dominate the soft X-ray background (CXB) and that unresolved AGN are the dominant contaminant in X-ray all-sky surveys (for overviews see Brandt & Hasinger 2005; Brandt & Yang 2022; Bourne & Yang 2023, and the references therein). Hence, to compare the predictions from FLAMINGO with

<sup>8</sup> It is also common to assume a photon index of  $\Gamma = 1.9$  (e.g. Aird et al. 2015; Shen et al. 2020), we find that the difference between assuming  $\Gamma = 1.8$  and 1.9 is negligible. A similar conclusion is reached by Lau et al. (2025) for the range  $\Gamma = 1.5, 1.9$

measurements and examine the impact of contamination from unresolved AGN on the measured cross-correlation, we must incorporate some level of contamination from unresolved AGN in the X-ray all-sky maps.

We create an AGN contaminated X-ray all-sky map by combining both the AGN ( $\mathbf{X}_{\text{AGN}}(\theta)$ ) and hot gas ( $\mathbf{X}_{\text{gas}}(\theta)$ ) maps with the binary point source masking scheme employed by Ferreira et al. (2024)<sup>9</sup>. We initially downgrade both  $\mathbf{X}_{\text{AGN}}(\theta)$  and  $\mathbf{X}_{\text{gas}}(\theta)$  from  $N_{\text{side}} = 4096$  to 2048 before summing them and masking all pixels that contain a point source above the threshold of 0.02 photon s<sup>-1</sup>, matching the limits imposed by both Ferreira et al. (2024) and the RASS diffuse X-ray background maps of Snowden et al. (1997). The final masked map contains both the X-ray emission from hot gas and unresolved AGN. Pixels that contain point sources (e.g. resolved AGN) are identified using the pixel values of  $\mathbf{X}_{\text{AGN}}(\theta)$ .

### 3.2 Black Hole Luminosities and Abundances

In this paper we estimate the X-ray emission from AGN, as described above, using three different populations of BHs: *i*) a base set, which includes all BH particles as they ‘naturally’ exist within the FLAMINGO PLCs, *ii*) a simple abundance matched (AM) set, in which we reassign BH bolometric luminosities to match observations; and *iii*) an extension of this abundance matched set,  $\Delta\text{AM}$ , where we intentionally alter the contamination from unresolved AGN by perturbing the scatter in the BH Luminosity – maximum circular velocity relation. We adopt these three different approaches to: *i*) attain a ‘natural’ FLAMINGO prediction of the X-ray emission from AGN; *ii*) correct the abundances of AGN luminosities in FLAMINGO to agree with observed luminosity functions; and *iii*) explore the extent to which X-ray contamination from unresolved AGN can alter the predicted X-ray–lensing cross-correlations.

#### 3.2.1 The Luminosities and Abundances of Black Holes in FLAMINGO

The bolometric luminosities of the ‘base’ BH particles in FLAMINGO are computed from the BH mass accretion rates ( $\dot{M}_{\text{accr}}$ ) as  $L_{\text{bol}} = \dot{M}_{\text{accr}}\epsilon_{\text{r}}c^2$ , where we assume a constant radiation efficiency of  $\epsilon_{\text{r}} = 0.1$  (the relations between  $L_{\text{bol}}$ ,  $L_{\text{x}}$  and  $\dot{M}_{\text{accr}}$  are depicted in Appendix A). The mass accretion rates are given by the FLAMINGO BH subgrid prescriptions (see Schaye et al. 2023). In this paper we refer to these BHs as the base BHs and by extension the base AGN.

As shown by Ding et al. (2025), these base BHs have an underabundance of both bright and faint quasars relative to observations for redshifts  $z \gtrsim 1$  (we confirm the same underabundance is replicated by the PLCs in Appendix B). The lack of bright quasars is predominantly driven by the spatial and temporal resolution of FLAMINGO being insufficient to resolve the small-scale variability of the processes surrounding BH mass accretion, which drive fluctuations in quasar luminosity. Hence, FLAMINGO is unable to capture the peaks of these fluctuations and instead underestimates the variability in quasar bolometric luminosity, which contributes to the observed underabundance of bright quasars. Given these ‘missing’ bright quasars occupy sufficiently high redshifts, the observed photon flux from these quasars may then fall below the minimum flux at which point sources can be resolved. As such, the base AGN may

underestimate the total X-ray emission from unresolved AGN. Accounting for these ‘missing’ bright quasars may increase the impact of AGN contamination on the measured cross-correlation.

#### 3.2.2 Matching Black Hole Abundances with Observations

Here, we introduce a simple abundance matching approach to repopulate the lightcones with quasars such that they reproduce, at individual redshifts, the quasar luminosity functions (QLFs) given by Shen et al. (2020, equation 11 and Table 3, local ‘polished’ fits). These QLFs are provided at multiple redshifts from  $z = 0.2$  to 6.0 in intervals of  $\Delta z = 0.2$  and are fit independently at each redshift (see the description of the local fits in Table 2 of Shen et al. 2020).

For a given model QLF, at redshift  $z_{\text{qlf}}$ , we sample bolometric luminosities and assign them to BHs based on their host halo properties as follows:

(i) For each halo in the lightcone with at least one BH particle<sup>10</sup> at redshift  $z = z_{\text{qlf}} \pm 0.1$ ,<sup>11</sup> we place a quasar in the lightcone at the location of the halo’s most massive BH (MMBH).

(ii) We then use the observed QLF to iteratively sample new bolometric luminosities in discrete logarithmic luminosity bins of width 0.1 dex. In each luminosity bin,  $N_i$  new bolometric luminosities are sampled from a uniform distribution that spans the width of the bin.  $N_i$  is determined by sampling a Poisson distribution with a mean of  $\lambda = \langle N_i \rangle$ , where  $\langle N_i \rangle$  is the expected number of quasars with luminosities that fall within bin  $i$  and is determined from the integral of the observed QLF over the range of the luminosity bin. Starting with the maximum luminosity bin, which is centred on  $L_{\text{max}} = 1 \times 10^{50}$  erg s<sup>-1</sup> we then continuously repeat this sampling, shifting the centre of each bin by 0.1 dex for each iteration until the total number of sampled bolometric luminosities is equal to the number of selected MMBHs. Across all redshifts, we find that the maximum bolometric luminosity sampled does not exceed  $L_{\text{max}} = 2 \times 10^{49}$  erg s<sup>-1</sup> (this corresponds to a BH mass of  $\sim 10^{11} M_{\odot}$  given the Eddington rate limited Bondi-Hoyle rate used within FLAMINGO) whilst the minimum luminosity fluctuates within the range  $1 \times 10^{39} \lesssim L_{\text{min}}/\text{erg s}^{-1} \lesssim 1 \times 10^{41}$ .

(iii) The sampled bolometric luminosities are ranked in descending order, whilst the selected MMBHs are ranked in descending order of mass accretion rate. The sampled luminosities are assigned to the BHs via rank, i.e. the MMBH with the greatest mass accretion rate is assigned the highest bolometric luminosity.

In this paper we will refer to this method and these abundance matched BHs (and by extension AGN), where bolometric luminosities are assigned based on mass accretion rates, as the AM model and AM BHs (and AM AGN).

By design, the AM model imparts the BH Luminosity–halo mass relation inherent to each FLAMINGO simulation onto the AM BHs. The BH Luminosity–halo mass relation is tied to the contribution from unresolved AGN to the contaminated X-ray–lensing cross-correlation. BH Luminosity is explicitly related to BH X-ray emission (see §3.1.2) and as halo mass scales with density, it is therefore linked to the strength of the lensing signal (see equation 3). In general, decreasing (increasing) the intrinsic scatter in the BH Luminosity–halo mass relation will strengthen (diminish) the correlation between the

<sup>9</sup> Whilst not out-right specified in Ferreira et al. (2024), we have confirmed via private communication that the same masking procedure and data is replicated in La Posta et al. (2025).

<sup>10</sup> In the L1\_m9 FLAMINGO simulations BHs are seeded in haloes more massive than  $\approx 2.76 \times 10^{11} M_{\odot}$  (Schaye et al. 2023).

<sup>11</sup> For the lowest redshift QLF,  $z_{\text{qlf}} = 0.2$ , we use all haloes within the lightcone at redshifts  $z < 0.3$ .

X-ray emission from unresolved AGN and the lensing signal therefore, elevating (lowering) the impact of unresolved AGN on the resultant X-ray–lensing cross-correlation. Predicated on this idea we now expand on the aforementioned abundance matching approach and intentionally perturb the BH Luminosity–halo mass relation in order to explore the extent to which AGN contamination can impact FLAMINGO’s X-ray–lensing cross-correlations.

In this alternate approach we now rank selected BHs by the host haloes’ maximum circular velocity<sup>12</sup> instead of the mass accretion rate. Additionally, prior to ranking each halo, we now perturb the intrinsic scatter in the BH Luminosity – maximum circular velocity by inducing a log-normal scatter onto the haloes’ maximum circular velocities. The level of log-normal scatter is given by a free parameter,  $\sigma_r$ . We refer to these abundance matched BHs and the resultant AGN as  $\Delta\text{AM}$  BHs and  $\Delta\text{AM}$  AGN.

The maximum circular velocity is a robust proxy for the total dynamical mass within a halo (see Appendix B). Of course, a natural choice would be to rank via halo mass; however, this is rather ambiguous to define in a physically meaningful way (e.g. in terms of  $M_{200c}$ ), given we use all gravitationally bound haloes with at least one BH particle and the SOAP catalogues only contain  $M_{200c}$  values for central haloes. Hence, we adopt maximum circular velocity as a proxy for halo mass. Additionally, the choice to induce a log-normal scatter on only the maximum circular velocity does not fully constrain the BH Luminosity - halo maximum circular velocity relation (or, by extension the BH Luminosity - halo mass relation), which can be done with a more sophisticated model (e.g. Ren et al. 2020; Ren & Trenti 2021; Pizzati et al. 2024). However, we do not require this level of specificity, given the intended use of this abundance matching model is to simply examine what is possible when it comes to AGN contamination (as will be shown in §4.3) and not to constrain an exact level of intrinsic scatter in the BH Luminosity–halo mass relation.

We choose to include all three sets of BHs in our analysis, as each has their own pros and cons. The unresolved AGN given by the base BHs are self-consistent with the FLAMINGO simulations and maintain a ‘natural’ distribution of bolometric luminosities that reflects the different cosmologies and baryonic feedback variations in FLAMINGO. However, the base BHs do not reproduce the observed QLFs. Both sets of abundance matched BHs (AM and  $\Delta\text{AM}$ ) are fixed to reproduce the observed quasar abundances and offer an increased flexibility to explore the potential effects of AGN contamination, but are reliant on some strong assumptions, e.g., only allowing one black hole per halo or that we can sample the model QLF models below the minimum luminosity they are fit to.

### 3.3 Computing X-ray – lensing cross-correlations from FLAMINGO

Here we describe the map-based methodology used in this paper to compute X-ray–lensing cross-correlations from the FLAMINGO lightcones. In §3.1 we discussed the various integrated X-ray all-sky maps ( $\mathbf{X}(\theta)$ ) that will be cross-correlated with our FLAMINGO

<sup>12</sup> maximum circular velocity is calculated as  $v_{\max} = \sqrt{GM(\leq r)/r}$  using all particles bound to the subhalo within the radius  $r$ , that are further than one softening length from the centre of potential and  $r = 0$  at the centre of potential.

based weak-lensing observable, an all-sky map of the convergence field,  $\kappa(\theta)$ <sup>13</sup>.

We construct convergence maps ( $\kappa(\theta)$ ) from the lightcone total mass maps (total mass implying all matter along the line of sight, including neutrinos) using the Born approximation. As outlined by McCarthy et al. (2018),  $\kappa(\theta)$  can be computed by integrating  $\delta(\theta)$  along the line of sight weighted by the lensing kernel (window Function),  $W^{\gamma_i}(\chi)$ , of the  $i$ -th tomographic source sample,

$$\kappa(\theta) = \int_0^{\chi(z_{\max})} W^{\gamma_i}(\chi) \delta(\chi, \theta) d\chi, \quad (3)$$

where  $\delta(\chi, \theta)$  is the 2D projected density contrast map at comoving distance  $\chi$ , which can be computed from the surface mass density ( $\Sigma(\chi, \theta)$ ) as  $\delta(\chi, \theta) \equiv (\Sigma(\chi, \theta) - \bar{\Sigma}(\chi))/\bar{\Sigma}(\chi)$  where  $\bar{\Sigma}(\chi)$  is the mean surface density. The window function  $W^{\gamma_i}(\chi)$  is given by

$$W^{\gamma_i}(\chi) = \frac{3}{2} \left( \frac{H_0}{c} \right)^2 \Omega_m \frac{\chi}{a(\chi)} \int_{z(\chi)}^{z_{\max}} n_{s,i}(z') \left( \frac{\chi(z') - \chi(z)}{\chi(z')} \right) dz', \quad (4)$$

where  $a(\chi)$  is the scale factor at a comoving distance  $\chi$ ,  $z_{\max} = 3$  is the maximum redshift of the L1\_m9 lightcone and  $n_{s,i}(z)$  is the normalised redshift source distribution of the  $i$ -th sample. We adopt the redshift source distribution of DES-Y3 as given by Doux et al. (2022) (see the inset panel of Fig. 1 for a normalised version of the source distribution given in figure 2 Doux et al. 2022). As in §3.1, we compute  $\kappa$  by downgrading each constituent over-density map ( $\delta(\chi, \theta)$ ) to  $N_{\text{side}} = 4096$  and applying the same rotation scheme. The  $\kappa(\theta)$  and  $\mathbf{X}(\theta)$  all-sky maps (including the binary mask for resolved point sources, if applicable) are then downgraded to  $N_{\text{side}} = 1024$  in order to match the angular resolution of the maps used by Ferreira et al. (2024). We then compute the X-ray–convergence cross-correlation with the COMPUTE\_FULL\_MASTER function of the NAMASTER<sup>14</sup> package (Alonso et al. 2019), using the same binning scheme as García-García et al. (2021) (i.e. Table 2 of Nicola et al. 2021) over the angular scales  $30 \leq \ell \leq 3N_{\text{side}}$ , giving us 24 binned points per  $C_{\ell}^{\kappa\kappa}$  computed. We assume a flat-sky when computing the angular cross-power spectrum, which is sufficiently accurate for angular scales given by  $\ell \gtrsim 30$ .

Finally, for all ROSAT-like X-ray–lensing cross-correlations, in order to make a fair comparison and match the analysis of Ferreira et al. (2024), we do not deconvolve the pixel window function from the cross-correlation, but instead apply a Gaussian beam (using the GAUSS\_BEAM function from the HEALPix package) with a full-width-half-max of  $1.8'$  to account for the ROSAT point-spread function (i.e. Snowden et al. 1997). In contrast, for all normalised X-ray–lensing cross-correlations (which are not compared to the observational datasets) we deconvolve the pixel window function using the PIXWIN function in the HEALPix package and do not apply a Gaussian beam.

<sup>13</sup> We make the distinction of using convergence instead of cosmic shear ( $\gamma$ ), as cosmic shear is not directly measurable from the lightcones 2D maps, whilst the convergence ( $\kappa(\theta)$ ) can be easily computed from the matter over-density ( $\delta$ ). Given the flat-sky limit implicit in our 2D map-based analysis the resulting E-mode auto(cross)-correlations,  $C_{\ell}$ , with convergence are equivalent to those obtained from cosmic shear (e.g Kilbinger 2015; Kilbinger et al. 2017).

<sup>14</sup> <https://namaster.readthedocs.io/en/latest/>

## 4 RESULTS

In this section we present the primary results of this study in three parts. In §4.1 we present the X-ray–lensing cross-correlation for the fiducial L1\_m9 simulation and demonstrate the FLAMINGO simulation’s ability to reproduce the directly measured cross-correlation of Ferreira et al. (2024). In §4.2 we identify the contribution from hot gas in different halo masses and examine the cross-correlation’s sensitivity to both cosmology and baryonic feedback. Finally, in §4.3 we compare the predictions from FLAMINGO to the measurements of Ferreira et al. (2024). Through these comparisons we will examine the impact of contamination from unresolved AGN on the measured cross-correlation and look to constrain the role of baryonic feedback in the suppression of large-scale structure (LSS) formation.

### 4.1 Comparison of the fiducial model to observations

We begin by presenting the predicted ROSAT–DES-Y3 X-ray–lensing cross-correlation ( $C_\ell^{XK}$ ) for the fiducial L1\_m9 simulation and making a simple comparison to the measurements of Ferreira et al. (2024). With this comparison we will demonstrate FLAMINGO’s capacity to reproduce observations and introduce the different ROSAT-like cross-correlations that we will utilise throughout this paper. We compute a ROSAT-like X-ray–lensing cross-correlation, as outlined in §3.3, for two different scenarios: *i*) where we only include the X-ray emission from hot gas (see §3.1.1) and *ii*) when the soft X-ray emission from hot gas is contaminated by unresolved AGN (see §3.1.3). In the latter scenario we compute an AGN contaminated cross-correlation using the base AGN and abundance matched AGN given by both the AM BHs and  $\Delta$ AM BHs (see §3.2).

In Fig. 1 we show the predicted ROSAT–DES-Y3 cross-correlation for the L1\_m9 simulation when the soft X-ray background is uncontaminated (solid curve) and when it is contaminated by unresolved AGN given by either the base FLAMINGO BHs (dotted curve) or abundance matched BHs (dashed curve and shaded regions) in comparison to the measurements of Ferreira et al. (2024) (triangle markers and error bars). The dashed curve (labelled, AM) corresponds to the AGN contamination from the AM BHs (see §3.2). The shaded regions (labelled  $\Delta$ AM) correspond to the range of cross-correlations given from the  $\Delta$ AM model (see §3.2.2), where we intentionally perturb the intrinsic scatter in the BH Luminosity – maximum circular velocity relation whilst constructing a set of abundance matched BHs;  $\Delta$ AM BHs. The upper (and lower) bound of the shaded regions correspond to when the intrinsic scatter is minimised (and maximised) within the confines of the model. The tomographic bin number is shown in the upper left hand corner of each panel (X-ray source distribution – lensing source distribution) and in the top right panel we display (inset) the normalised form of the DES-Y3 redshift source distribution of each tomographic bin given by Fig. 2 of Doux et al. (2022). Furthermore, in Table 2, we show the  $\chi^2$  values computed in each tomographic bin and, for all tomographic bins combined, the number of standard deviations ( $N_\sigma$ ) offset of the predicted L1\_m9 cross-correlations with respect to the measurements. We compute the  $\chi^2$  values using the covariance matrices of Ferreira et al. (2024)<sup>15</sup> with 24 degrees of freedom per tomographic bin and 96 for the whole dataset. The  $N_\sigma$  values are computed from the sum of the  $\chi^2$  values.

In Fig. 1 it is evident that the uncontaminated (hot gas only) cross-correlation reproduces the measurements of Ferreira et al. (2024)

remarkably well, as summarised in Table 2, the predicted cross-correlation is within  $0.3\sigma$  of the observational data points. The cross-correlation increases in power for more distant (i.e. higher redshift) tomographic bins (depicted by the inset in Fig. 1). The longer path to more distant galaxies allows for a greater lensing effect, which in turn increases the measured cross-correlation. Moreover, a greater number of lensing sources at redshifts further than  $z = 0.5$  can increase the spatial overlap between the sources of X-ray emission and the intervening mass that produces the lensing signal, allowing for a greater signal of the cross-correlation. Recall that the L1\_m9 particle lightcones only store hot gas particles for  $z \leq 0.5$  (see §3.1). Note for the predicted cross-correlations in bin x-3 and x-4 a majority of the lensing sources are found at redshifts greater than (e.g. behind) the highest redshift X-ray source. In Table 2 we find that the cross-correlations in the x-1 bin has a significantly lower  $\chi^2$  value (i.e. a better match between L1\_m9 and the measurements) compared to other tomographic bins. However, we may assume this is primarily driven by the larger uncertainty from the DES-Y3 cosmic shear data for the lowest redshift bin, which is visible in Fig. 1.

The comparison of the predicted gas-only cross-correlation does not account for AGN that remain unresolved in the RASS dataset. As illustrated by the shaded region, dotted and dashed curves in Fig. 1, the inclusion of unresolved AGN increases the power of the cross-correlation over all angular scales shown, such that the predicted cross-correlations are now discrepant with the observed dataset. This is summarised in the bottom row of Table 2 by the increased  $N_\sigma$  values for the Base AGN, AM and  $\Delta$ AM curves compared to the gas only cross-correlation. The ‘boost’ in power from unresolved AGN increases towards both larger and smaller angular scales on either side of  $\ell \approx 600$ , with the increase in power being largest for the larger angular scales we consider (e.g.  $30 < \ell \lesssim 3 \times 10^2$ ). Across all four tomographic bins the unresolved AGN given by the base and AM AGN, on average, account for  $\approx 22\%$  (ranging between  $\approx 12 - 40\%$ ) and  $\approx 30\%$  (ranging between  $\approx 21 - 55\%$ ) of the measured cross-correlation’s power, respectively. In particular, the large increase in power due to the AGN contamination given by the AM BHs results in the predicted cross-correlation for the L1\_m9 simulation being incompatible with the measurements of Ferreira et al. (2024). If we view the limits of the  $\Delta$ AM AGN cross-correlations as the total scatter or uncertainty about the AM AGN contaminated cross-correlation, then for the minimum contamination given by the  $\Delta$ AM AGN (shown by the lower bounds of the shaded regions in Fig. 1) the L1\_m9 simulation is offset from observations by  $1.96\sigma$ , as shown in Table 2. However, if we consider the upper bounds set by the  $\Delta$ AM AGN cross-correlations (when AGN contamination is maximised within the  $\Delta$ AM model), the increase in power results in L1\_m9 significantly overestimating the measured dataset ( $N_\sigma = 11.1$ ). As a whole this demonstrates that contamination from unresolved AGN has the potential to significantly alter the power of the X-ray–lensing cross-correlation and must not be neglected. We leave all further discussion of unresolved AGN for §4.3.

### 4.2 Origin and robustness of the uncontaminated signal

Here we examine the sensitivity of the predicted FLAMINGO X-ray–lensing cross-correlation to baryonic feedback and develop an understanding of where the hot gas (baryonic matter) traced by this probe resides within the LSS. Contrary to §4.1, we will use idealised X-ray–lensing cross-correlations (computed as outlined in §3.3), meaning the X-ray all-sky map,  $\mathbf{X}(\theta)$  [ $\text{photon s}^{-1} \text{cm}^{-2}$  (pixel area) $^{-1}$ ] is not convolved with the ROSAT response matrix and only includes

<sup>15</sup> The covariance matrices corresponding to the measurements of Ferreira et al. (2024) have been made publicly available by La Posta et al. (2025)

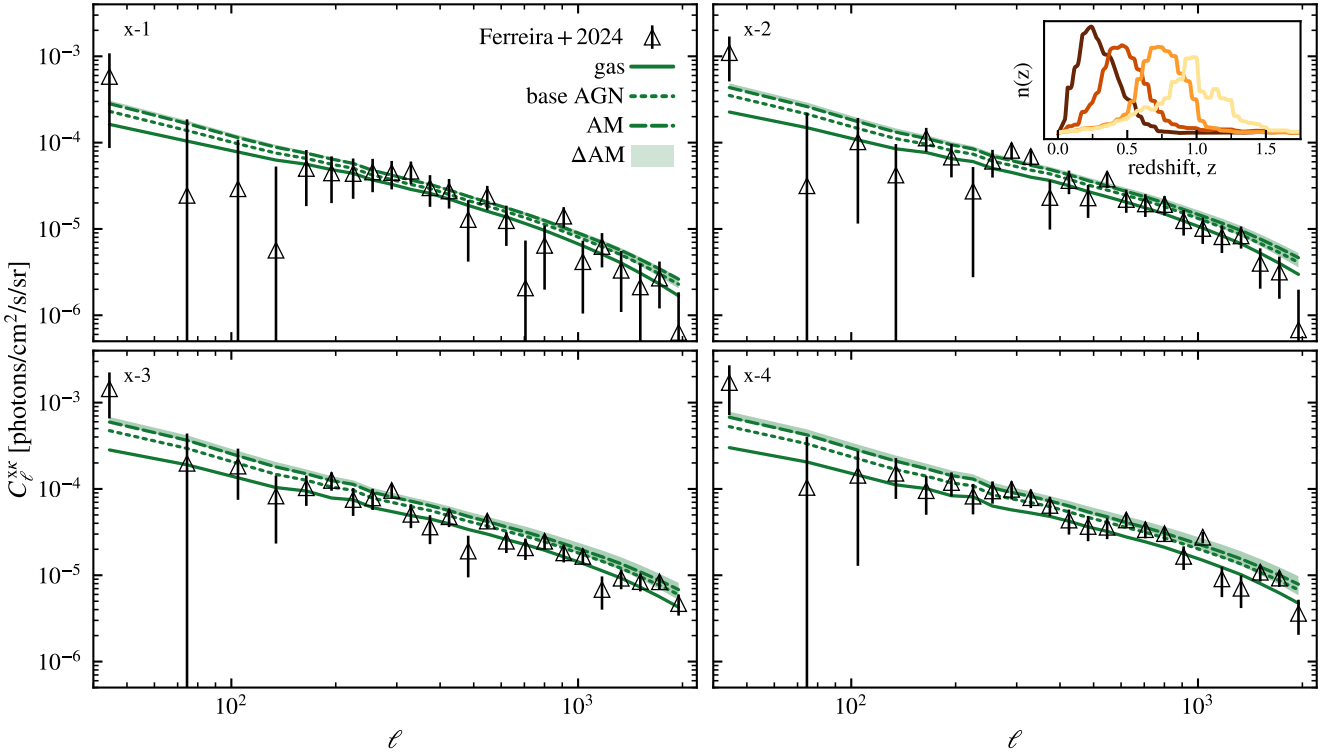


**Figure 1.** The predicted ROSAT-DES-Y3 X-ray-lensing cross-correlation from the L1\_m9 fiducial FLAMINGO simulation (green curves) compared to the observational data points of Ferreira et al. (2024) (black points and error bars). The numbers in the upper left corner of each panel indicate the DES-Y3 tomographic bin of the shown cross-correlations (e.g. x-1, indicates the cross-correlation of the X-ray signal with the first tomographic bin of the lensing data). Here, the X-ray emission of the L1\_m9 simulation is convolved with the ROSAT response matrix (see §3.1.1). The solid curves correspond to the predicted cross-correlation if only the X-ray emission from hot gas is included, i.e. it is contamination free. The dotted curves include the X-ray emission from unresolved AGN given by the base FLAMINGO BHs. The dashed curves (AM) depict the AGN contaminated cross-correlations when the unresolved AGN are given by the AM BHs. The shaded regions ( $\Delta$ AM) indicate the full range of possible cross-correlations from minimising and maximising the AGN contamination given by the  $\Delta$ AM BHs as described in the text. All sets of BHs (base, AM and  $\Delta$ AM) are described in §3.2). The inset in the top right panel depicts the normalised DES-Y3 source distribution, given by figure 2 of Doux et al. (2022), and each tomographic bin (1 through 4, moving left to right) is individually coloured. Without the inclusion of unresolved AGN the simulation reproduces the measurements. However, AGN contamination increases the power of the cross-correlation over all angular scales considered, reducing the agreement with the data.

the X-ray emission from hot gas (i.e. uncontaminated by unresolved AGN).

#### 4.2.1 Decomposition of the soft X-ray flux

As shown by McCarthy et al. (2023), the cosmic shear auto-correlation has a very weak dependence on baryonic physics for the angular scales we consider. Hence, we can expect the majority of the X-ray-lensing cross-correlation's dependence on baryonic physics to stem from the X-ray component. The range of angular scales, halo masses and redshifts that the angular (and 3D) power spectra from cosmic shear probes are sensitive to is well known (see relevant discussions in e.g. Joachimi et al. 2021; Broxterman et al. 2024; Doux & Karwal 2026), however, we have less intuition when it comes to diffuse X-ray emission. To understand where the hot gas traced by our FLAMINGO X-ray-lensing cross-correlation comes from, we decompose the X-ray emission by both redshift and halo mass before recomputing the cross-correlation.

We decompose the X-ray all-sky map by the redshift of the gas into 10 shells of equal width ( $\Delta z = 0.05$ ; i.e. the same as the concentric shells of the FLAMINGO lightcones) for all gas along the line of sight between  $z = 0$  and  $z = 0.5$ . With the L1\_m9 simulation, we

compute the X-ray-lensing cross-correlation (as described in §3.3) between the photon flux from each shell ( $\mathbf{x}(\chi(z), \theta)$ ) and the total convergence map ( $\kappa(\theta)$ ; equation 3). The total convergence map is computed from the full redshift range of the lightcones,  $z \leq 3$ , as done in §3.3.

The resultant cross-correlations are presented in Fig. 2. The colour of each cross-correlation shown corresponds to the redshift range of the gas as given by the colour bar (each colour indicates a different redshift shell within the lightcone). The tomographic bin number is indicated in the upper right corner of each panel. As a point of comparison, we overlay the X-ray-lensing cross-correlations corresponding to the total X-ray emissions from gas for all redshifts  $z \leq 0.5$  (grey dot-dashed curve) and  $z \leq 3.0$  (black dotted curve). These redshift ranges correspond to the maximum redshift of hot gas particles in the PLC and the on-the-fly HEALPix maps of the lightcone.

There are a few notable trends displayed in Fig 2. Firstly, across all tomographic bins the power of the cross-correlation decreases as the redshift of the gas increases, which is expected given that photon flux scales as  $\propto (\chi(z)^2(1+z))^{-1}$ , where  $\chi$  is the comoving distance of the source from the observer. This is made apparent in Fig. 2, where  $\gtrsim 94\%$  of the total soft X-ray contribution to the cross-correlation comes from gas at  $z \leq 0.5$ . Secondly, the contribution from gas at  $z \leq 0.1$  decreases with  $\ell$  for  $\ell \gtrsim 200$ . For  $z \leq 0.1$  there is simply less

**Table 2.** The  $\chi^2$  values ( $\chi^2$ ), within each tomographic bin, and number of standard deviations ( $N_\sigma$ ) of the predicted X-ray–lensing cross-correlation (as shown in Fig. 1) with respect to the measurements of Ferreira et al. (2024). We compute both of the  $\chi^2$  for each tomographic bin (rows 1 through 4) and  $N_\sigma$  values from the sum of the  $\chi^2$  values across all tomographic bins (bottom row). There are a total of 24 data points per tomographic bin and 96 in total, the  $\chi^2$  values are computed from the diagonal covariance matrices of Ferreira et al. (2024). From left to right we give the summary statistics for the predicted cross-correlations when we only consider the X-ray emission from hot gas (Gas) and when we include the X-ray emission from the base unresolved AGN (Base AGN, dotted curve in Fig. 1) and abundance matched unresolved AGN (AM  $\pm$   $\Delta$ AM). We show the summary statistics computed for the contaminated cross-correlations given by the AM BHs (AM, dashed curve in Fig. 1), whilst the super (sub) scripts given indicate the upper (lower) bounds of the cross-correlations for the  $\Delta$ AM BHs (the shaded regions in Fig. 1).

Bin	Gas	Base AGN	AM $\pm$ $\Delta$ AM
x-1	15.8	19.9	$26.9^{+7.1}_{-3.1}$
x-2	23.7	29.9	$42.8^{+27.6}_{-9.4}$
x-3	24.8	29.0	$53.1^{+69.8}_{-16.0}$
x-4	34.8	27.0	$44.7^{+67.2}_{-13.8}$
$N_\sigma$	0.3	0.7	$4.3^{+6.8}_{-2.3}$

structure that is able to contribute to the cross-correlation on these scales given the smaller cosmic volume and at such low redshifts, a portion of these angular scales ( $\ell > 200$ ) correspond to physical scales which are unresolved in the lensing signal. Note, the lack of structure is due to the cosmological volume, the halo mass function remains consistent for each shell of the lightcone (see FLAMINGO halo mass functions given by Schaye et al. 2023). Lastly, with increasing tomographic bin number, the contribution to the measured cross-correlation from higher redshift gas increases relative to lower redshift gas. As the bin number increases, the distribution of lensing source galaxies and structures that produce the lensing effect (the lensing signal) stretch to higher redshifts (see inset in Fig. 1). At higher redshifts a greater volume of X-ray emitting hot gas is coincident with the lensing signal and therefore the cross-correlation of the two fields increases.

Continuing in a similar manner, we decompose the X-ray all-sky map by total halo mass,  $M_{200c}$  (i.e. the total mass encompassed by the radius,  $R_{200c}$ , within which the mean mass is 200 times the critical density) and compute the cross-correlation with the total convergence map ( $\kappa(\theta)$ ; equation 3). We match the gas particles in the lightcones to the nearest redshift occurrence of the same particle, by particle ID<sup>16</sup>, in the snapshot data. We allow a maximum difference between the redshift of the snapshot and the redshift at which the particle entered the lightcone of  $\Delta z = 0.025$ , as the snapshots are output with a cadence of  $\Delta z = 0.05$  for the needed redshift range. Using the snapshot data, we identify a gas particle as ‘belonging’ to a halo if the distance ( $r$ ) between the particle and the halo’s centre is less than  $R_{200c}$  for the given halo. If a gas particle ‘belongs’ to multiple haloes, we assign the particle to the closest halo in terms of  $r/R_{200c}$ . We consider only central (field) haloes.

Fig. 3 compares the contribution to the cross-correlation from the X-ray signal of gas inside  $R_{200c}$  of all haloes ( $r \leq R_{200c}$ , all  $M_{200c}$ , black dashed curve), haloes within a given mass range ( $r \leq R_{200c}(M_{200c})$ , indicated by the colour bar) and gas outside of haloes ( $r > R_{200c}$ , dot-dashed curves). The cross-correlation computed from

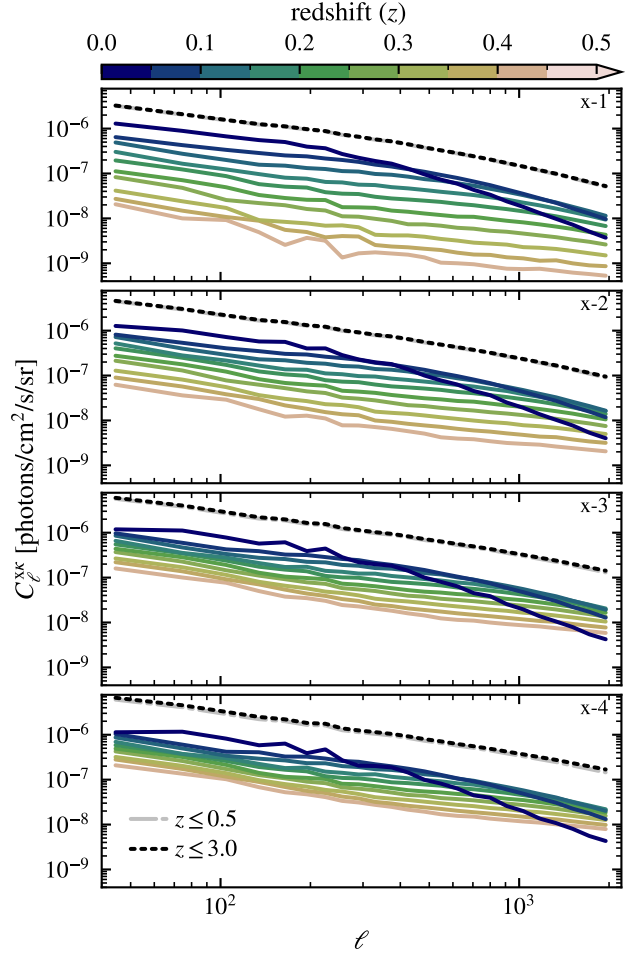


**Figure 2.** The contribution of the diffuse X-ray emission to the X-ray–lensing cross-correlation, predicted by the L1\_m9 simulation, decomposed by the redshift of the X-ray emitting hot gas. It is assumed that the X-ray signal is uncontaminated by unresolved AGN. The redshift range of the hot gas is indicated by the colour bar. Additionally, the cross-correlations computed from the total diffuse X-ray signal integrated over the redshift ranges  $0 \leq z \leq 0.5$  (grey dot-dashed) and  $0 \leq z \leq 3.0$  (black dotted) are overlaid for a point of reference. Note that the lensing signal is computed for the maximum redshift depth of the L1\_m9 lightcone ( $z \leq 3.0$ ). The tomographic bin number of each panel is displayed in the upper right corner. The contribution to the cross-correlation decreases with the redshift of the X-ray emitting gas and more than 90% of the cross-correlation is due to gas at  $z \leq 0.5$ .

all hot gas within the PLC (L1\_m9) is overlaid in green. We only display the third tomographic bin (x-3) as there is little difference between bins (we repeat this figure for all tomographic bins in Appendix C).

From Fig. 3 it is clear that the cross-correlation is dominated by gas within  $R_{200c}$  of haloes, which accounts for 90–97% of the signal. Specifically, we find that haloes with  $M_{200c} \sim 10^{14} M_\odot$  dominate for  $\ell > 250$ , and haloes of mass  $M_{200c} \geq 10^{14} M_\odot$  dominate for larger angular scales, where  $\ell < 250$ . X-ray emission from haloes of  $M_{200c} < 10^{13.5} M_\odot$  accounts for less than 5% of the total cross-correlation. As such, we can expect the X-ray–lensing cross-correlation to be most sensitive to baryonic feedback processes that are closely linked to cluster gas fractions. The cross-correlation from haloes with  $M_{200c} < 10^{13} M_\odot$  is noisier than the cross-correlation for any other mass range shown in Fig. 3. At a glance this may appear

<sup>16</sup> A unique identifying number for each particle.

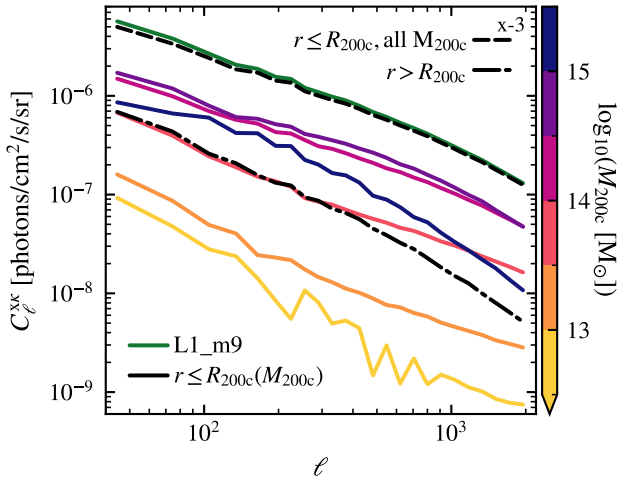


**Figure 3.** The contribution to the X-ray-lensing cross-correlation of the L1\_m9 simulation decomposed by the mass ( $M_{200c}$ ) of the halo responsible for the X-ray emission. Here, it is assumed that the X-ray emission is only due to hot gas (i.e. uncontaminated by unresolved AGN). The X-ray all-sky map is decomposed into the contributions from gas within  $R_{200c}$  of all haloes ( $r \leq R_{200c}$ , all  $M_{200c}$ , dashed black curve), haloes of a given mass, ( $r > R_{200c}$  ( $M_{200c}$ ), solid curves) and outside of haloes ( $r > R_{200c}$ , dot-dashed black curve). The colour of each solid curve corresponds to the halo mass range shown in the colour bar. Additionally the cross-correlation computed using all gas is overlaid in green. The X-ray emission from gas within haloes of masses  $10^{14} \leq M_{200c}/M_{\odot} < 10^{15}$  dominates the predicted cross-correlation.

strange as there are many more haloes with  $M_{200c} < 10^{13} M_{\odot}$  in the lightcone than haloes with  $M_{200c} \geq 10^{13} M_{\odot}$ , however because of their low luminosities, only a limited number of these haloes at very low redshifts significantly contribute to the cross-correlation.

#### 4.2.2 Sensitivity to cosmology and baryonic feedback

Armed with some intuition about the X-ray-lensing cross-correlation's sensitivity to hot gas within haloes of different masses, we now explore the baryonic feedback and cosmology dependence of this probe. We particularly wish to identify the extent to which the cross-correlations can break degeneracies between the effects of varying either the cosmology or baryonic feedback.

In Fig. 4 we compare the X-ray-lensing cross-correlations for the different L1\_m9 simulations, showing the dependence on cosmology and baryonic physics (i.e. subgrid prescriptions). Each of the simulations shown, as indicated by colour, is described further in §2.1. Note that here the soft X-ray emission only traces hot gas, i.e. it is uncontaminated by unresolved AGN, and it is not convolved with the response matrix from any telescope. For simplicity only the third tomographic bin (x-3) is shown, but there is little evolution between bins (the cross-correlations in all four bins can be found in Appendix C). The left panel of Fig. 4 examines the dependence on the strength of stellar and AGN feedback parametrized through the cluster gas fraction used to calibrate the subgrid prescriptions. The gas fraction is primarily mediated via the strength of AGN feedback. We compare the X-ray-lensing cross-correlations for each of the cluster gas fraction variations in FLAMINGO (the gas fraction is varied over the range of  $+2\sigma$  to  $-8\sigma$  from the observed halo mass - gas fraction relation). There is a clear dependence on the AGN feedback strength, where decreasing the cluster gas fraction (increasing the strength of

feedback) leads to an almost uniform suppression of the predicted cross-correlation over all angular scales considered. The inverse is shown for an increased gas fraction. A similar effect is identified by Shirasaki et al. (2020) (Fig. 5), where, using a halo model formalism, the computed X-ray-lensing cross-correlation decreases almost uniformly when the model allows for a greater amount of energy to be injected into a halo by AGN and supernova feedback.

The centre panel of Fig. 4 shows the remaining baryonic feedback models. This includes the  $-1\sigma$  variations in the stellar mass function ( $M^*-\sigma$  and  $M^*-\sigma_{fgas}-4\sigma$ ) the kinetic jet model of AGN feedback calibrated on the fiducial cluster gas fraction (Jet) and the adiabatic (no-cooling) simulation. The no-cooling simulation demonstrates that ignoring baryonic feedback and cooling results in a dramatic increase in power over all angular scales. Reducing the stellar mass function (SMF) suppresses the predicted cross-correlation on all scales, as seen by the orange curve in Fig. 4. However, the cross-correlation is less sensitive to variations in the SMF in comparison to the cluster gas fraction. This can be understood with our conclusions from Fig. 3. The X-ray component is dominated by hot gas in haloes with mass  $M_{200c} \sim 10^{14} M_{\odot}$ . As such, for the angular scales we consider in this paper, the X-ray-lensing cross-correlation is more sensitive to baryonic feedback processes that can more efficiently alter the cluster gas fraction, i.e. AGN feedback. The physical processes, such as supernova feedback, which mediate the SMF characteristically impact the distribution of baryonic matter on smaller physical scales than AGN feedback. We find that the mode of AGN feedback only has a minor effect with the jet mode of AGN feedback (Jet) having a small increase in power relative to the thermal mode (the fiducial L1\_m9 simulation) at both the largest (small  $\ell$ ) and smallest (large  $\ell$ ) angular scales shown. As discussed by Braspenning et al. (2024), the two AGN feedback modes redistribute and expel gas from clusters in different ways, which results in the cluster temperature and density profiles for each AGN feedback mode slightly diverging within cluster cores. Such changes in the core temperatures and densities could drive the minor differences we see in the X-ray-lensing cross-correlations.

We now turn our attention to the dependence on cosmology. The right panel of Fig. 4 compares the cross-correlations for the fiducial D3A cosmology (L1\_m9), the ‘Planck’ cosmology with varying neutrino masses; 0.06, 0.24 and 0.48 eV (Planck, PlanckNu0p24Fix and PlanckNu0p48Fix respectively) and the ‘lensing’ cosmological model for calibrated on the fiducial and  $-8\sigma$  cluster gas fractions (LS8 and LS8\_fgas- $8\sigma$ , respectively). We see a clear dependence on cosmology and the summed neutrino mass. The near uniform offset of the cross-correlations for each cosmology shown relative to the prediction for the fiducial D3A cosmology are ranked in order of the  $\sigma_8$  cosmological parameter (see Table 1).

Comparing between the sub panels of Fig. 4, it becomes apparent that the effects of cosmology and baryonic physics are largely degenerate, at least for the angular scales considered in this study, as both result in offsets from the fiducial model that are of similar magnitude and are nearly independent of angular scale.

#### 4.2.3 Sensitivity to box size and resolution

In Fig. 5 we examine the dependence on the simulation box size and resolution. Here the soft X-ray emission only originates from hot gas, i.e. it is uncontaminated, and it has not been convolved with the response matrix from any telescope. Again, for clarity only the third tomographic bin (x-3) is shown as there is little difference between the four tomographic bins (we compare all four tomographic bins in Appendix C). The blue shaded region and curve correspond to the

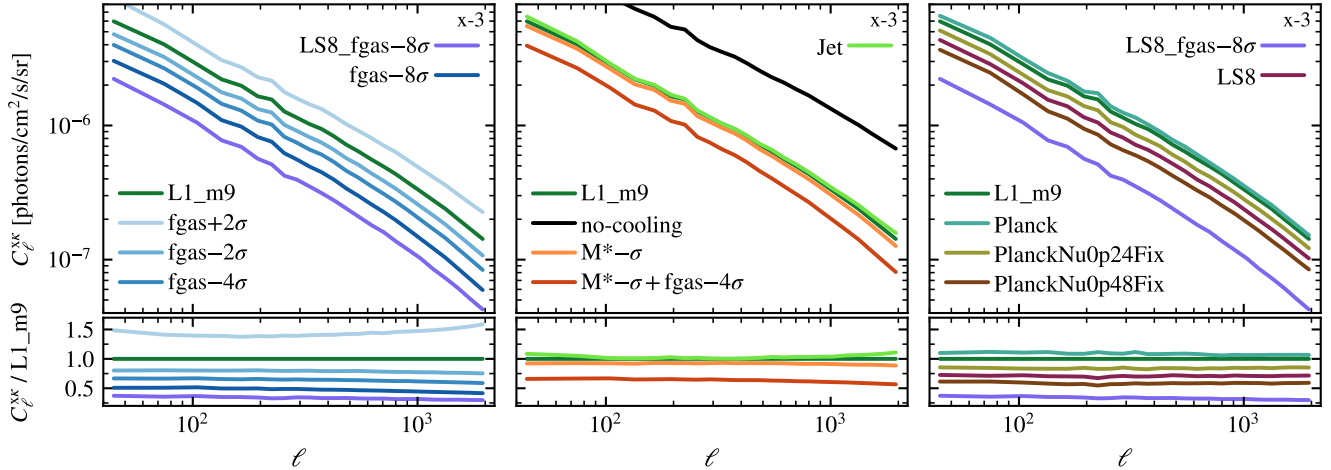


**Figure 4.** The cosmology and baryonic feedback dependence of the predicted X-ray–lensing cross-correlation. In each main panel, the coloured curves correspond to the predicted cross-correlations in the third tomographic bin (x-3) for the different L1\_m9 simulations as indicated by the legend (see §2.1 and Table 1). The lower sub-panels compare the variations to the fiducial L1\_m9 (dark green) simulation (i.e.  $C_\ell^{\text{XK}} / \text{L1\_m9}$ ). Note we only consider the X-ray emission from hot gas and do not convolve the X-ray emission with the response matrix of any telescope. *Left:* The dependence on the cluster gas fraction (fgas) that the model has been calibrated to. Reducing the cluster gas fraction (mainly by increasing the strength of AGN feedback) suppresses the power of the cross-correlation over all angular scales considered. *Centre:* The predicted cross-correlations for the remaining baryonic feedback variations. Reducing the stellar mass function suppresses the signal on all scales, however this effect is secondary to varying the cluster gas fraction. The choice of AGN feedback model (jet or thermal mode of feedback) has a very minor scale-dependent effect. *Right:* The dependence on cosmology and neutrino mass. The cross-correlation for the LS8 cosmology is suppressed relative to the fiducial model over all scales shown. Reducing the cluster gas fraction for the LS8 cosmology (LS8\_fgas – 8 $\sigma$ ) further suppresses the signal. Increasing the summed neutrino mass relative to the fiducial value (0.06 eV) reduces the power over all scales shown. Comparing between the three panels, it is clear that the effects of varying the cosmology and baryonic feedback are largely degenerate.

median and scatter of the X-ray–lensing cross-correlations for the 8 different lightcones of the larger box size (L2p8\_m9) simulation. The remaining solid coloured curves are the predictions for a singular lightcone for a simulation with a given resolution (indicated by the legend), whilst the grey curves (dot, dashed and dot-dashed) indicate different cluster gas fraction variations of the fiducial L1\_m9 simulation. We show each simulation relative to L1\_m9 in the bottom panel. Recall that the subgrid prescriptions (e.g. the baryonic feedback models) have been calibrated on the same observed cluster gas fractions for each resolution; low (L1\_m10), intermediate (L1\_m9 and L2p8\_m9) and high (L1\_m8). Therefore, the different resolutions should be considered as separate models of baryonic physics.

From Fig. 5 we see that the predicted X-ray–lensing cross-correlations are converged with box size, but not with resolution. The features seen in shaded region for  $\ell \lesssim 400$  indicate that cosmic variance – while decreasing towards smaller scales – is driven by the presence of a few, rare, massive clusters which have a disproportionate impact on the power of the cross-correlation. This is supported by the conclusions from Fig. 3, where a few hundred haloes of mass  $M_{200c} > 10^{15} \text{ M}_\odot$  (that is  $\lesssim 2\%$  of haloes more massive than  $M_{200c} > 10^{13} \text{ M}_\odot$ ) account for 15 – 20% of the X-ray signal in the cross-correlation for  $\ell \lesssim 400$ . Relative to the cross-correlation for the intermediate-resolution (L1\_m9) simulation, the high-resolution (L1\_m8) simulation has less power on all scales and shows a general trend decreasing more for smaller angular scales. This trend is mirrored by the low-resolution (L1\_m10) prediction.

This lack of convergence with resolution is likely not directly caused by the mass resolution itself, but is instead due to the imperfect recalibration of the subgrid models and the differences in the thermodynamic profiles for fixed gas fractions (see relevant discussions by Schaye et al. 2023; Kugel et al. 2023). As shown in Kugel et al. (2023), at redshift  $z = 0.1$ , the median gas fraction ( $f_{\text{gas}, M_{500c}}$ )

of haloes with mass  $M_{500c} > 1.5 \times 10^{14} \text{ M}_\odot$  for L1\_m8 is less than that of L1\_m9. Note, that L1\_m8 is calibrated to reproduce the cluster gas fractions for haloes with masses between  $M_{500c} = 10^{13.5}$  and  $10^{13.75} \text{ M}_\odot$ , therefore the divergence from L1\_m9 occurs outside the calibrated halo mass range. Additionally,  $f_{\text{gas}, M_{500c}}$  of haloes with  $M_{500c} > 5 \times 10^{14} \text{ M}_\odot$  for the fgas-2 $\sigma$  variation of L1\_m9 is comparable to the gas fractions of L1\_m8. Given that both the gas fraction (Fig. 4) and haloes within these mass ranges (see Fig. 3) are significant for the cross-correlation, it is understandable that the X-ray–lensing cross-correlation of the high-resolution simulation is suppressed relative to the fiducial L1\_m9 simulation and is similar to the fgas-2 $\sigma$  simulation (further discussion can be found in Appendix D). If we compare the differences between the cross-correlations for the different resolutions with those between the different baryonic feedback variations and cosmologies in Fig. 4, we find that the effect of varying the mass resolution is secondary to both cosmology and baryonic feedback.

#### 4.3 Comparing FLAMINGO feedback variations to observations

Having examined the sensitivity of the X-ray–lensing cross-correlation to both cosmology and baryonic feedback, we now turn our attention to making comparisons to observational data. Through these comparisons we explore which, if any, of the baryonic feedback variations in FLAMINGO are incompatible with the measurements of Ferreira et al. (2024). To compare the predictions from the FLAMINGO suite with these measurements, we now include unresolved AGN and convolve the X-ray emission (from both hot gas and unresolved AGN) with the ROSAT response matrix before computing the ROSAT–DES-Y3 X-ray–lensing cross-correlation.

As noted in §2.1, the PLCs of the Planck, PlanckNu0p24Fix,

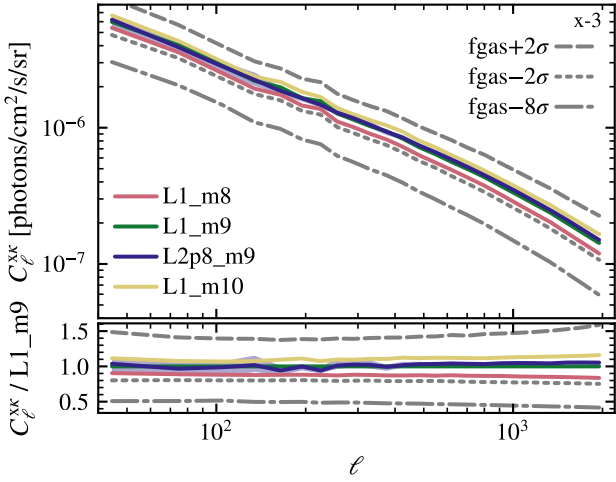


**Figure 5.** The dependence of the predicted X-ray-lensing cross-correlation on the simulation box size and numerical resolution. For clarity we show only the third tomographic bin and assume the soft X-ray emission is uncontaminated by unresolved AGN. The blue shaded region and solid curve correspond to the scatter and median for each of the 8 individual observers (lightcones) for the L2p8\_m9 simulation. The remaining solid curves correspond to a single lightcone for a given resolution model at a fixed box side length of 1 Gpc. The grey curves correspond to varying the cluster gas fraction by  $\pm 2\sigma$  (dashed),  $\pm 2\sigma$  (dotted) and  $\pm 8\sigma$  (dot-dashed) from the fiducial L1\_m9 model. In the bottom panel each simulation is shown relative to L1\_m9. The cross-correlation is converged with box size but not with resolution, as shown by the suppressed (elevated) signal of the high (low) resolution, L1\_m8 (L1\_m10), model relative to the intermediate resolution (L1\_m9 and L2p8\_m9) models. The dependence on resolution is likely indirect, reflecting residual differences in cluster gas profiles despite the recalibration. However, the differences between the different resolutions are smaller than the differences between the feedback variations.

PlanckNu0p48Fix and LS8 FLAMINGO simulations do not store any information about the gas particles. As such, for the remainder of this section we will only utilise the FLAMINGO simulations with variations of the cluster gas fraction ( $\text{fgas} - N\sigma$ ) for the fiducial D3A cosmology and the  $\text{fgas} - 8\sigma$  variation for the lensing cosmology: LS8\_fgas-8 $\sigma$ . We opt to exclude the stellar mass function variations ( $M^* - N\sigma$ ) as the X-ray-lensing cross-correlation is significantly more sensitive to changes in the cluster gas fraction (see Fig. 4). Additionally, we do not include the adiabatic (no-cooling) simulation because it is not realistic and, given the discussion in §4.2, we omit the jet mode of AGN feedback (Jet) as there is only a minor deviation from the cross-correlation of the fiducial L1\_m9 simulation.

In Fig. 6 we compare the predicted ROSAT-DES-Y3 X-ray-lensing cross-correlations for each of the cluster gas fraction variations to the measurements of Ferreira et al. (2024) (black points and error bars). Note that all X-ray emission (from both hot gas and unresolved AGN) is convolved with the ROSAT response matrix and for clarity we only show the cross-correlations in the third tomographic bin. The solid curves show the cross-correlations for each gas fraction variation (indicated by colour) when we only account for the X-ray emission from hot gas (top panel) and when we include the X-ray emission from unresolved AGN given by the base BHs (centre panel) or AM BHs (bottom panel). Both sets of models for unresolved AGN are described in §3.2. The dotted curves give the AGN X-ray-lensing cross-correlation,  $C_\ell^{\text{AGN}K}$ , which is the cross-correlation between the X-ray emission from unresolved AGN and the FLAMINGO lensing all-sky maps. Finally, for each simulation

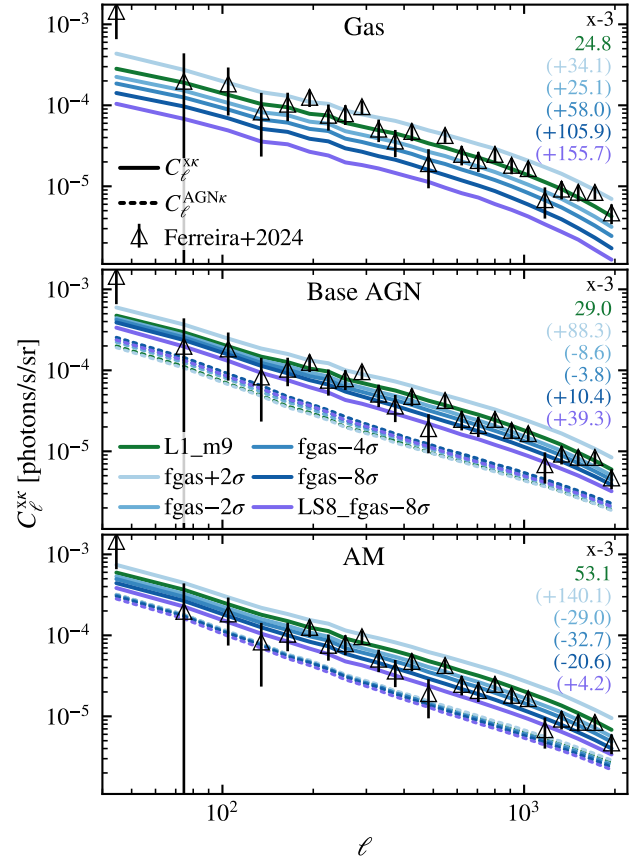


**Figure 6.** The predicted ROSAT-DES-Y3 X-ray-lensing cross-correlation, in the third tomographic bin (x-3), for the gas fraction variations ( $\text{fgas} \pm N\sigma$ ) and fiducial L1\_m9 simulation (solid curves) compared to the measurements of Ferreira et al. (2024) (black points and error bars). All X-ray emission is convolved with the ROSAT response matrix. *Top:* The predicted cross-correlation when only the X-ray emission from hot gas is included. *Centre:* We include the X-ray emission from both hot gas and unresolved AGN given by the base BHs. *Bottom:* The same as the centre panel, but the AGN contamination is given by the AM BHs. The base BHs and AM BHs are described in §3.2. The dotted curves give the cross-correlation of the X-ray emission from each set of unresolved AGN and DES-Y3 all-sky maps ( $C_\ell^{\text{AGN}K}$ ) for the simulation of the corresponding colour. The  $\chi^2$  value of the cross-correlation, in the third tomographic bin, for the fiducial L1\_m9 simulation (dark green) and the observational data is printed on the right hand side of each panel. The values in parentheses are the  $\Delta\chi^2$  (see text) for each cluster gas fraction (indicated by colour). The inclusion of unresolved AGN increases the power of the cross-correlation and more so for the AM BHs.

we compute the  $\chi^2$  value between the predicted X-ray-lensing cross-correlation and the covariance matrices of the X-ray-cosmic-shear data in each tomographic bin. The  $\chi^2$  value for the fiducial L1\_m9 simulation, computed for the third tomographic bin, is printed on the right hand side of each panel. The values listed below in parentheses indicate the difference between the  $\chi^2$  values for each gas fraction variation (indicated by colour) and the fiducial L1\_m9 simulation;  $\Delta\chi^2 = \chi^2 - \chi^2_{\text{L1\_m9}}$  in the third tomographic bin. A negative  $\Delta\chi^2$  indicates an improvement in agreement with the data points, whilst the inverse is true for a positive  $\Delta\chi^2$  value. We repeat Fig. 6 for all four tomographic bins in Appendix C. Table 3, presents the sum of the  $\chi^2$  values in each tomographic bin and the number of standard deviations ( $N\sigma$ ) between each predicted ROSAT-DES-Y3 X-ray-lensing cross-correlation and the measurements of Ferreira et al. (2024). In

Table 3, all values of  $N_\sigma$  that are inconsistent with observations, which we define as greater than  $2\sigma$  deviation ( $N_\sigma > 2$ ), are printed in bold.

In the top panel of Fig. 6, we find the same dependencies on the strength of baryonic feedback (parametrised through the cluster gas fraction used to calibrate the subgrid prescriptions) as for the idealised counterparts depicted in Fig. 4. When we neglect AGN contamination, the fiducial L1\_m9 model fits the observed data points more closely than the other cluster gas fraction variations, as demonstrated by the positive  $\Delta\chi^2$  values. As summarised in Table 3, in this gas-only scenario, only the fiducial L1\_m9 simulation is compatible (i.e.  $N_\sigma \leq 2$ ) with the observations.

When we include AGN contamination in the predicted cross-correlations, as shown in the centre and bottom panels of Fig. 6, the power of the cross-correlation increases on all angular scales (as discussed in §4.1). In comparison to the uncontaminated cross-correlations in the top panel, the AGN-contaminated cross-correlations are shifted upwards with respect to the observed data points. By comparing the  $C_\ell^{\text{AGNk}}$  curves in the centre and bottom panels we see that the AM AGN boost the signal of the X-ray-lensing cross-correlation more than the base AGN. This boost in power is reflected by the  $\chi^2$  values in Fig. 6, e.g., the base AGN cross-correlation for the fiducial L1\_m9 simulation ( $\chi^2 = 29.0$ ) overestimates the data-points by less than the AM AGN counterpart ( $\chi^2 = 69.6$ ).

The  $\Delta\chi^2$  values listed within each panel of Fig. 6 indicate that increasing the level of AGN contamination, which elevates the signal of the cross-correlation, results in simulations calibrated on lower cluster gas fractions (i.e. with an increased strength of baryonic feedback) being more compatible with the observations. Additionally, contamination from unresolved AGN (for both the base AGN and AM AGN) obscures the sensitivity of the X-ray-lensing cross-correlation to changes in the strength of baryonic feedback (cluster gas fraction). In comparison to the uncontaminated cross-correlations (top panel of Fig. 6), we find there is a smaller offset between the cluster gas fraction variations within both sets of contaminated cross-correlations. This decreased sensitivity to changes in baryonic feedback strength reduces the constraining power of the observed dataset.

The boost in power and reduced sensitivity to changes in the strength of baryonic feedback due to AGN contamination results in the X-ray-lensing cross-correlations for multiple L1\_m9 simulations being far more compatible with the measurements of Ferreira et al. (2024) as opposed to only the fiducial L1\_m9 simulation when AGN contamination is neglected. As summarised in Table 3, when we include X-ray emission from the base AGN, fgas+2 $\sigma$  ( $N_\sigma = 11.1$ ), fgas-8 $\sigma$  ( $N_\sigma = 3.6$ ) and LS8\_fgash-8 $\sigma$  ( $N_\sigma = 7.4$ ) are incompatible with the observations. However, with the contamination from the AM AGN, L1\_m9 ( $N_\sigma = 4.3$ ), fgas+2 $\sigma$  ( $N_\sigma = 16.7$ ) and LS8\_fgash-8 $\sigma$  ( $N_\sigma = 6.0$ ) are all clearly incompatible with the observations. The increased level of AGN contamination from the AM AGN results in fgash-8 $\sigma$  being offset from the observed dataset by  $2.3\sigma$ . We find that fgash-2 $\sigma$  and fgash-4 $\sigma$  are consistent with the observations for both sets of contaminated cross-correlations, in contrast to LS8\_fgash-8 $\sigma$ , which cannot be reconciled with the observations.

In §4.2 we highlighted that the effects of variations in cosmology and baryonic physics are largely degenerate for the angular scales considered. Given these degeneracies and the assumption that the effects of AGN contamination and the ROSAT response matrix (see Appendix A) are consistent across all FLAMINGO simulations we can extend the conclusions about the different cluster gas fraction variations in Fig. 6 to the different cosmologies based on the simi-

**Table 3.** The  $\chi^2$  values and number of standard deviations,  $N_\sigma$ , between the predicted ROSAT-DES-Y3 X-ray-lensing cross-correlations for the cluster gas fraction variations of the L1\_m9 simulation shown in Fig. 6 and the measurements of Ferreira et al. (2024). The  $\chi^2$  and  $N_\sigma$  values are for the dataset as whole, combining the values computed in each tomographic bin (24 data points per bin) with the covariance matrices given by Ferreira et al. (2024). From left to right, the summary statistics shown are computed for when the cross-correlation is uncontaminated (Gas), contaminated by the unresolved AGN given by the Base BHs (Base AGN) or from the AM BHs (AM). Values of  $N_\sigma$  that are inconsistent with the observations,  $N_\sigma > 2$ , are printed in bold.

Identifier	Gas		Base AGN		AM	
	$\chi^2$	$N_\sigma$	$\chi^2$	$N_\sigma$	$\chi^2$	$N_\sigma$
L1_m9	99.0	0.3	105.8	0.7	167.5	<b>4.3</b>
fgash+2 $\sigma$	191.7	<b>5.5</b>	338.3	<b>11.1</b>	539.1	<b>16.7</b>
fgash-2 $\sigma$	171.0	<b>4.5</b>	88.9	0.0	95.8	0.0
fgash-4 $\sigma$	264.5	<b>8.5</b>	107.6	0.9	91.3	0.0
fgash-8 $\sigma$	398.7	<b>12.9</b>	153.6	<b>3.6</b>	130.3	<b>2.3</b>
LS8_fgash-8 $\sigma$	537.1	<b>16.6</b>	237.9	<b>7.4</b>	202.6	<b>6.0</b>

larities of the idealised cross-correlations shown in Fig. 4. We can therefore assume in a gas only scenario, that the Planck simulation, which most resembles the fiducial L1\_m9 simulation, would be the only cosmology variation consistent with the observations. Conversely, for the AM AGN-contaminated cross-correlations we assume that only the Planck simulation would be clearly inconsistent with the observations as it overestimates the fiducial L1\_m9 simulation on large scales (see Fig. 4). Given the idealised cross-correlations for the remaining cosmology variations (i.e. LS8, PlanckNu0p24Fix and PlanckNu0p48Fix) are suppressed relative to the fiducial L1\_m9 simulation most similarly to the fgash-2 $\sigma$  and fgash-4 $\sigma$  simulations we would not expect any of them to be clearly inconsistent with the observations when contaminated with unresolved AGN given by either the base BHs or AM BHs.

#### 4.3.1 Varying the contamination by unresolved AGN

As indicated by Fig. 6 contamination from unresolved AGN can have a notable impact on the X-ray-lensing cross-correlation. To estimate this effect we utilise the  $\Delta$ AM BHs introduced in §3.2.2, these are similar to the AM BHs, except that we perturb the BH Luminosity – maximum circular velocity relation (the maximum circular velocity is a robust proxy for halo mass) to alter the impact of contamination from unresolved  $\Delta$ AM AGN on the X-ray-lensing cross-correlation. Recall that for each population of  $\Delta$ BHs, we induce a log-normal scatter onto the maximum circular velocities of all haloes prior to re-assigning the BH luminosities by the rank order of the selected haloes' maximum circular velocities. The level of log-normal scatter is given by a free parameter,  $\sigma_r$ .

In Fig. 7 we use the fiducial L1\_m9 simulation to demonstrate how the contribution from unresolved AGN to the measured cross-correlation varies with  $\sigma_r$ . Here, we show the cross-correlation of the X-ray emission from only unresolved  $\Delta$ AM AGN and the lensing signal,  $C_\ell^{\text{AGNk}}$ , as a fraction of the ‘full’ X-ray – lensing cross-correlation (i.e. the X-ray component includes the X-ray emission from both hot gas and unresolved AGN),  $C_\ell^{\text{Xk}}$ . For clarity we only show the third tomographic bin. Each dot-dashed curve corresponds to a different population of  $\Delta$ AM BHs parametrised by  $\sigma_r$ , which is indicated by the colour bar. Additionally, as a point of reference,

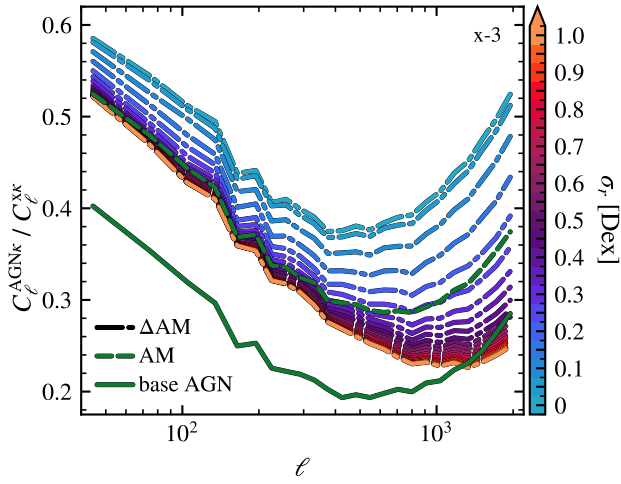


**Figure 7.** The contribution from unresolved AGN to the predicted ROSAT-DES-Y3 X-ray-lensing cross-correlation for the fiducial L1\_m9 simulation. Each curve shows the fraction of the predicted cross-correlation that is attributed to the cross-correlation of the X-ray emission from unresolved AGN and the lensing signal ( $C_\ell^{\text{AGN}k} / C_\ell^{\text{X}k}$ ) for the value of  $\sigma_r$  (indicated by colour). The tomographic bin is indicated in the upper right corner. The solid and dashed green dashed curves show the contributions from unresolved AGN as given by the base BHs and AM BHs respectively (as shown in Fig. 6). A larger value of  $\sigma_r$  increases the intrinsic scatter of the BH Luminosity–halo mass relation, which reduces the contribution from unresolved AGN to the X-ray-lensing cross-correlation. AGN contamination is maximised when  $\sigma_r = 0$  dex.

we overlay the contributions from unresolved AGN for the base BHs (solid green curve) and the AM BHs (dashed green curve).

Fig. 7 highlights that the level of AGN contamination can be increased or decreased relative to that from the AM AGN by decreasing and respectively increasing the intrinsic scatter of the BH Luminosity – maximum circular velocity relation. Incremental changes in  $\sigma_r$  alter the level of AGN contamination on all angular scales, however, the effect is greater on smaller angular scales. The level of AGN contamination is maximised when we set  $\sigma_r = 0$  dex, i.e. when we minimise the scatter in the BH Luminosity – maximum circular velocity (and halo mass) relation and therefore maximise the correlation between the X-ray emission from AGN and the lensing signal. In Fig. 7 we see that the relation between  $\sigma_r$  and the level of AGN contamination from  $\Delta\text{AM}$  AGN saturates for  $\sigma_r > 0.4$  dex. For larger  $\sigma_r$  the rankings (or distribution) of the maximum circular velocities becomes so ‘shuffled’ by the induced log-normal scatter that any underlying (or pre-existing) correlation between the unperturbed (i.e. before including log-normal scatter) maximum circular velocities and BH luminosities is now highly disrupted.

In Fig. 8 we compare the range of  $\Delta\text{AM}$  AGN contaminated cross-correlations, in the third tomographic bin, for the fiducial L1\_m9 simulation and our most extreme cluster gas fraction variations,  $\text{fgas}+2\sigma$  and  $\text{fgas}-8\sigma$ , to the measurements of Ferreira et al. (2024). The coloured shaded regions outline the  $\Delta\text{AM}$  AGN contaminated cross-correlations corresponding to the range  $\sigma_r = 1$  dex (minimum contamination) to  $\sigma_r = 0$  dex (maximum contamination). Additionally, we overlay the AM AGN contaminated cross-correlations (as shown in the bottom panel of Fig. 6) as solid curves where the colour corresponds to the simulation. The bottom panel gives the ratio of the X-ray-lensing cross-correlation when only the X-ray emission

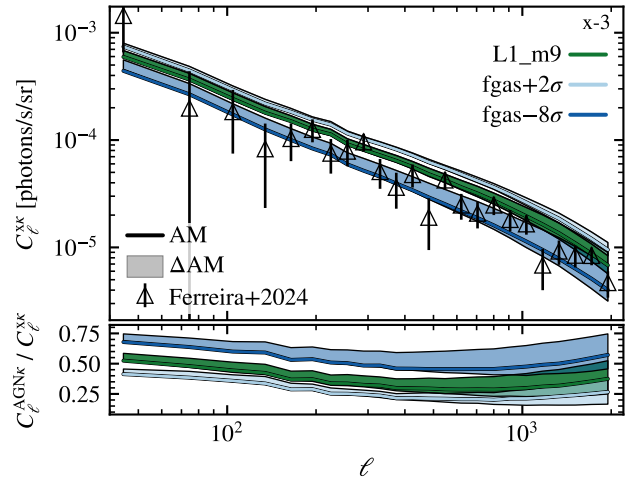


**Figure 8.** The ROSAT-DES-Y3 X-ray-lensing cross-correlations, in the third tomographic bin (x-3), for the  $\text{fgas}+2\sigma$  and  $\text{fgas}-8\sigma$  variations of the L1\_m9 simulation compared to the measurements of Ferreira et al. (2024) (black points and error bars). All X-ray emission is convolved with the ROSAT response matrix. The shaded regions correspond to the range of X-ray-lensing cross-correlations contaminated by  $\Delta\text{AM}$  AGN with  $0 \leq \sigma_r \leq 1$  dex (see description in the text). The solid curves correspond to the cross-correlation contaminated by AM AGN (the same as shown in Fig. 6). The sub-panels show the ratio of the X-ray-lensing cross-correlations when only the X-ray emission from unresolved AGN is included ( $C_\ell^{\text{AGN}k}$ ) and when both the X-ray emission from hot gas and unresolved AGN are accounted for ( $C_\ell^{\text{X}k}$ ).

from unresolved AGN is included ( $C_\ell^{\text{AGN}k}$ ) and when both the X-ray emission from hot gas and unresolved AGN is accounted for.

As shown by the spread of the shaded regions in Fig. 8, the X-ray-lensing cross-correlations for simulations calibrated to reproduce lower cluster gas fractions are more sensitive to changes in the contamination by unresolved AGN. Additionally, the relative contribution from unresolved AGN increases with the strength of baryonic feedback. This is simply a result of the signal from hot gas decreasing with increased baryonic feedback strength whilst the X-ray emission from the unresolved  $\Delta\text{AM}$  AGN remains mostly consistent for each simulation. Moreover, the contribution of unresolved AGN to the cross-correlation increases in higher redshift tomographic bins (see §4.1 and Appendix C). Interestingly, within the confines of the  $\Delta\text{AM}$  model, the X-ray emission from the unresolved  $\Delta\text{AM}$  AGN contribute more to the cross-correlation than the gas. In such a scenario the X-ray-lensing cross-correlation may be more a probe of quasar clustering than a measure of how hot gas traces the matter density field.

Finally, for each of the  $\Delta\text{AM}$  AGN contaminated cross-correlations we compute the sum of the  $\chi^2$  values in each tomographic bin and the number of standard deviations ( $N_\sigma$ ) with respect to the measurements of Ferreira et al. (2024) (as done for Table 3). In Fig. 9 we visualise the range of  $N_\sigma$  values computed for each of the simulations listed in Table 3 (additionally, the  $\chi^2$  and  $N_\sigma$  are given in Table C1 of Appendix C). As an additional point of comparison, we overlay, for each cluster gas fraction variation, the  $N_\sigma$  values computed for the AM AGN (circular markers), base AGN (triangular markers) and uncontaminated (gas only; star markers) cross-correlations, which are listed in Table 3. The grey shaded regions overlaid in Fig. 9 outline  $N_\sigma \pm 2$  and  $N_\sigma \pm 1$ . In Fig. 9 we assign a negative sign to  $N_\sigma$  values to indicate that the FLAMINGO cross-correlation underestimates the observations (e.g. if the power of the cross-correlation is

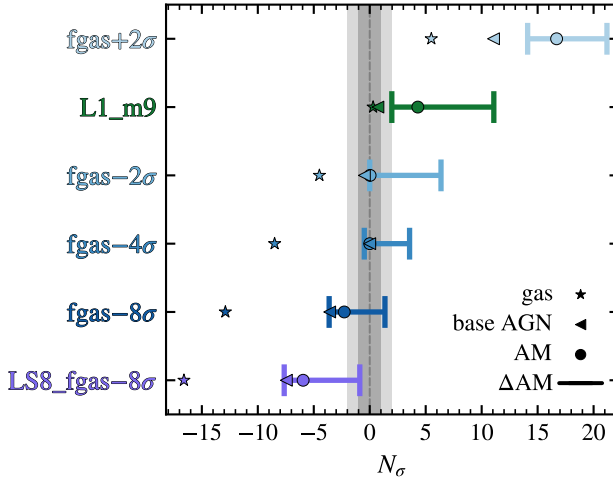


**Figure 9.** The number of standard deviations ( $N_\sigma$ ) between the FLAMINGO X-ray-lensing cross-correlations and the measurements of Ferreira et al. (2024) when unresolved AGN are neglected (Gas; star markers) and when the X-ray emission from unresolved AGN is given by: the base AGN (triangle markers), AM BHs (circle markers) and  $\Delta$ AM BHs (error bar). Values of  $N_\sigma$  are computed from the sum of the  $\chi^2$  values across all tomographic bins. The minimum (maximum)  $N_\sigma$  values, i.e. the left (right) tick on the error bar, for the  $\Delta$ AM AGN contaminated cross-correlations correspond to the AGN contamination being maximised (minimised) within the confines of the  $\Delta$ AM AGN model (see §3.2). A positive  $N_\sigma$  value indicates that the predicted cross-correlation over estimates the observations and the inverse is true for negative values.

increased then  $N_\sigma$  would decrease), whilst a positive  $N_\sigma$  value points to FLAMINGO overestimating the observations. The minimum  $N_\sigma$  values (left most tick) of each error bar correspond to the  $\Delta$ AM AGN cross-correlation when AGN contamination is minimised ( $\sigma_r = 1.0$  dex) within the confines of our abundance matching approach. Conversely, the maximum (right most tick) values of the error bar are given by the  $\Delta$ AM AGN cross-correlation when AGN contamination is maximised ( $\sigma_r = 0$  dex). Note that an incremental change in  $\sigma_r$  does not have a uniform effect on the measured cross-correlation (as demonstrated in Fig. 7) and sensitivity of the X-ray – lensing cross-correlation to changes in  $\sigma_r$  has some dependence on the strength of baryonic feedback (see relevant discussions on Fig. 8). As such, an incremental change in  $N_\sigma$  does not scale with  $\sigma_r$  the same way for each simulation.

As indicated by the large number of standard deviations spanned by the error bars in Fig. 9, perturbing the intrinsic scatter in the BH Luminosity – circular velocity relation can have significant consequences for the resultant X-ray – lensing cross-correlation. If we consider the full range of  $\Delta$ AM AGN contaminated cross-correlations, only  $\text{fgas}+2\sigma$  is clearly incompatible with the measurements of Ferreira et al. (2024). The fiducial L1\_m9 simulation is within  $2\sigma$  of the observed dataset when the contamination is from unresolved  $\Delta$ AM AGN parametrised by  $\sigma_r \geq 0.9$  dex. When we minimise the contamination from the unresolved  $\Delta$ AM AGN (i.e.  $\sigma_r = 1.0$  dex) L1\_m9,  $\text{fgas}-2\sigma$  and  $\text{fgas}-4\sigma$  simulations are all consistent with the observations to  $2\sigma$ . Conversely, for  $\sigma_r = 0$  dex we find only  $\text{fgas}-8\sigma$  and  $\text{LS8}_\text{fgas}-8\sigma$  are compatible with the observations, where  $N_\sigma = 1.4$  and 0.9 respectively. Moreover, we find that  $\text{fgas}-8\sigma$  is consistent to  $2\sigma$  with the observations when  $\sigma_r \leq 0.3$ , whilst, for  $\text{LS8}_\text{fgas}-8\sigma$  we find that  $N_\sigma$  is less than  $2\sigma$  for  $\sigma_r \leq 0.15$ .

If we reject the extremes of the  $\Delta$ AM model and instead assume a

‘most plausible’ small range of  $\Delta$ AM AGN (based on mean impact of the X-ray emission from unresolved  $\Delta$ AM AGN) when  $\sigma_r = 0.25 – 0.3$  dex we find that stronger AGN feedback than given by the L1\_m9 simulation is required to be consistent with Ferreira et al. (2024). Here, the  $\text{fgas}-2\sigma$ ,  $\text{fgas}-4\sigma$  and  $\text{fgas}-8\sigma$  simulations are consistent with the observed cross-correlation (we find  $N_\sigma = 0 – 0.1$ , 1.4 – 1.9, respectively), whilst the L1\_m9,  $\text{fgas}+2\sigma$  and  $\text{LS8}_\text{fgas}-8\sigma$  are incompatible (we find  $N_\sigma = 4.3 – 3.6$ , 16 – 15.5 and 5.1 – 5.8, respectively).

As summarised in Fig. 9, when AGN contamination is neglected only the X-ray–lensing cross-correlation for the fiducial L1\_m9 simulation is consistent with the observations. Simulations parametrised to have a greater strength of baryonic feedback underestimate the observations, as ‘stronger’ baryonic feedback suppresses the X-ray–lensing cross-correlation. The X-ray emission from unresolved AGN elevates the signal of the measured cross-correlations, such that the inclusion of the unresolved AGN given by the base BHs allows for simulations with stronger baryonic feedback (i.e.  $\text{fgas}-2\sigma$  and  $\text{fgas}-4\sigma$ ) to also be consistent with the observations. However, when we account for the underabundance of bright quasars in the base BH, by fixing their abundances to those of observed QLFs, the X-ray emission from the unresolved AM AGN further elevates the cross-correlation. As such, with the AM AGN contaminated cross-correlations simulations with a more ‘extreme’ parametrisation of baryonic feedback (e.g.  $\text{fgas}-8\sigma$ ) become more compatible with the observations whilst the fiducial L1\_m9 simulation is no longer consistent with the same dataset. We built on this abundance matching approach by inducing scatter in the BH Luminosity – circular velocity relation (a proxy for the BH Luminosity–halo mass relation). Within the confines of this abundance matching approach we find that the impact of AGN contamination can be increased such that only the simulations with the most ‘extreme’ baryonic feedback ( $\text{fgas}-8\sigma$  and  $\text{LS8}_\text{fgas}-8\sigma$ ) are compatible with the observations or, conversely, minimised (again, within the confines of our abundance matching approach) such that the fiducial L1\_m9 simulation is reconciled with the same measurements. However, we find it is not possible to sufficiently increase the intrinsic scatter in the BH Luminosity – circular velocity relation to allow for simulations with weaker baryonic feedback ( $\text{fgas}+2\sigma$ ) to be reconciled with the observations. The stronger baryonic feedback variations of the L1\_m9 simulation ( $\text{fgas}-2\sigma$  and  $\text{fgas}-4\sigma$ ) remain consistent with the observations provided the intrinsic scatter is not sufficiently lowered (i.e. increasing the impact of AGN contamination).

## 5 DISCUSSION AND OUTLOOK

In §5.1 we review our conclusions from §4 within the context of the AGN feedback strength required by recent studies utilising X-ray, weak-lensing and kSZ datasets. Then, in §5.2, we discuss possible improvements that can minimise the uncertainty about the impact of unresolved AGN, and we highlight a potential pitfall associated with the use of binary masks in this paper.

### 5.1 Comparing the X-ray–lensing cross-correlation to adjacent low redshift probes

In the recent literature there is a discrepancy in the required strength of AGN feedback and cluster gas mass fractions: kSZ measurements and selections of clusters observed by eROSITA require stronger, more efficient AGN feedback to expel gas from low-mass clusters than indicated by gas fractions inferred from pre-eROSITA X-ray

measurements and the scaling relations in low redshift clusters. Here we examine if the FLAMINGO X-ray–cosmic-shear cross-correlations presented in §4.3 can provide new insights on the topic given this new probe is orthogonal to kSZ measurements and sensitive to the strength of AGN feedback.

The joint modelling of kSZ measurements by [Schaan et al. \(2021\)](#) (from the Atacama Cosmology Telescope (ACT); specifically the maps of [Naess et al. 2020](#), *Planck* and the Baryon Oscillation Spectroscopic Survey (BOSS; as given by [Ahn et al. 2014](#))) with cosmic shear data from KiDS-1000 ([Asgari et al. 2021](#)) and DES (in particular the data summarised by [Sevilla-Noarbe et al. 2021](#)) by [Schneider et al. \(2022\)](#) and [Bigwood et al. \(2024\)](#) find a preference for stronger baryonic feedback (and lower cluster gas fractions) than prescribed by hydrodynamical simulations with cluster gas fractions akin to those of FLAMINGO’s fiducial L1\_m9 simulation. This conclusion is reaffirmed by [McCarthy et al. \(2025\)](#) who finds, through like-for-like comparisons of kSZ profiles measured from samples of haloes matched in mass via galaxy-galaxy lensing measurements (from both KiDS-1000 and DES-Y3 data, see [Amon et al. 2023](#)), that the fgas-8 $\sigma$  FLAMINGO simulation is consistent with [Schaan et al. \(2021\)](#), whilst the fiducial L1\_m9 simulation is discrepant, at a 7 $\sigma$  level in each halo mass samples. Additionally, [Siegel et al. \(2025a\)](#) find that the fgas-8 $\sigma$  FLAMINGO simulation is consistent with their joint analysis of SDSS/DESI+ACT kSZ profiles (given by [Schaan et al. 2021; Guachalla et al. 2025; Hadzhiyska et al. 2025](#)), eROSITA X-ray halo gas masses ([Bulbul et al. 2024](#)), and mean halo masses given by galaxy-galaxy lensing measurements (from regions overlapping with KiDS-1000, DES-Y3 and HSC [Giblin et al. 2021; Gatti et al. 2021; Li et al. 2022](#)). The fiducial L1\_m9 simulation is found to be a combined (from each halo mass sample)  $> 8\sigma$  discrepant from the observed kSZ profiles. Similar findings are, yet again, presented by [Bigwood et al. \(2025\)](#), whose systematic comparison of simulations to observed kSZ profiles (given by [Schaan et al. 2021; Guachalla et al. 2025; Hadzhiyska et al. 2025](#)) finds that the fiducial L1\_m9 FLAMINGO simulation is offset by 3.4 $\sigma$  from observations, whilst fgas-8 $\sigma$  is consistent (at a level of 1.2 $\sigma$ ). Together, these kSZ measurements appear to be inconsistent with the fiducial L1\_m9 simulation from FLAMINGO, which was calibrated on cluster gas fractions inferred from pre-eROSITA X-ray measurements (see [Kugel et al. 2025](#)), whilst preferring the lower cluster gas fractions and stronger AGN feedback of the fgas-8 $\sigma$  simulation. This preference for reduced cluster gas fractions is supported by the gas fractions inferred from the stacking of optically selected eROSITA clusters by [Popesso et al. \(2025\)](#). Specifically, [Popesso et al. \(2025\)](#) finds the gas fractions of low-mass clusters ( $M_{500c} \approx 10^{13.5-14.5} M_\odot$ ) are lower than those of the fiducial L1\_m9 simulation and are instead more consistent with the fgas-8 $\sigma$  simulation (see comparison in figure 5 of [Siegel et al. 2025a](#)).

It is shown by [Eckert et al. \(2025\)](#) that the X-ray luminosity and X-ray temperature scaling relations in low redshift galaxy groups (from the *XMM-Newton* Group AGN Project, X-GAP; see [Eckert et al. 2024](#)) are inconsistent with the stronger AGN feedback required by kSZ measurements and gas fractions from optically selected clusters. [Eckert et al. \(2025\)](#) finds their scaling relations are consistent with those from the fiducial L1\_m9 FLAMINGO simulation, whilst the fgas-8 $\sigma$  simulation underestimates both scaling relations such that it is discrepant at the 5.7 $\sigma$  level. Moreover, [Eckert et al. \(2025\)](#) cautions that the challenge of deriving cluster mass and gas fraction estimates can introduce large systematic uncertainties, which combined with bias from selection effects may be a contributing factor of this discrepancy.

As summarised in Fig. 9, given the assumed uncertainty in the level

of X-ray contamination from unresolved AGN, the X-ray–lensing cross-correlations for all but the fgas+2 $\sigma$  FLAMINGO simulation can be made consistent with the measurements of [Ferreira et al. \(2024\)](#). If we adopt the level of AGN contamination given by AM AGN or assume the more plausible median (exclude the less likely extremes) given by the  $\Delta$ AM AGN (assume an induced scatter of  $\sigma_r = 0.25 - 0.3$  dex) we find the X-ray–lensing cross-correlation has a preference for stronger AGN feedback than given by the fiducial L1\_m9 simulation, yet not to the same extreme as required by kSZ measurements. Here, compared to the measurements of [Ferreira et al. \(2024\)](#), the fgas-2 $\sigma$  and fgas-4 $\sigma$  simulations are more preferable (consistent at a  $< 0.1\sigma$  level) than the fgas-8 $\sigma$  simulation (which is consistent at a 1.4 $\sigma$  – 2.3 $\sigma$  level), whilst the fiducial L1\_m9 simulation is incompatible at a  $> 4\sigma$  level.

Increasing the impact of X-ray contamination from unresolved AGN (by decreasing  $\sigma_r$  within the  $\Delta$ AM model) results in stronger AGN feedback being required to remain consistent with the measurements of [Ferreira et al. \(2024\)](#). Within the bounds of the  $\Delta$ AM model, when the level of AGN contamination is increased such that fgas-8 $\sigma$  is consistent with the observations at a  $\leq 1\sigma$  level (where  $\sigma_r = 0.05 - 0.2$  dex, from the sampled values of  $\sigma_r$ ), the fiducial L1\_m9 simulation is incompatible at a  $> 5\sigma$  level. In such scenarios the X-ray–lensing cross-correlations agree with the kSZ measurements and optically selected stacks of eROSITA clusters. However, the X-ray–lensing cross-correlations can agree with the scaling relations of [Eckert et al. \(2025\)](#) and therefore disagree with the requirements of the kSZ measurements when the level of AGN contamination is minimised (by increasing  $\sigma_r$ ) within the  $\Delta$ AM model. Here, the L1\_m9 simulation can be consistent with the observations of [Ferreira et al. \(2024\)](#) at a  $\leq 2\sigma$  level (when  $\sigma_r \geq 0.9$  dex), whilst the fgas-8 $\sigma$  simulation is discrepant at a  $> 3.5\sigma$  level.

Although the X-ray–lensing cross-correlations predicted by FLAMINGO prefer stronger AGN feedback than given by the fiducial L1\_m9 simulation, it is not to the same extent as that required by kSZ measurements or inferred from stacks of optically selected eROSITA clusters. However, given the uncertainty ascribed to the X-ray contamination from unresolved AGN the X-ray–lensing cross-correlation can be compatible with both sides of the disagreement. Plainly, for our results to significantly contribute to the discourse surrounding the required strength of AGN feedback we must improve the constraining power of the X-ray–cosmic-shear cross-correlation, which may be achieved by resolving fainter AGN.

## 5.2 Reducing the impact of unresolved AGN

As detailed in §4.3, the X-ray emission from unresolved AGN has a non-negligible effect on the X-ray–lensing cross-correlations. Moreover, this X-ray contamination is one of the largest sources of uncertainty with respect to the comparisons made between FLAMINGO and the measurements of [Ferreira et al. \(2024\)](#). As such, there is a clear need to limit and further constrain the impact of contamination from unresolved AGN. The most straightforward way to limit the impact of unresolved AGN is to improve the detection and masking of point sources within the X-ray all-sky map, something that is much easier said than done.

The most immediate way to achieve this, with respect to this paper, is to use a higher resolution X-ray all-sky survey dataset than RASS (ROSAT All-Sky Survey), such as the all-sky survey by the SRG/eROSITA telescope ([Sunyaev et al. 2021; Predehl et al. 2021](#)). The publicly available half-sky (western hemisphere) X-ray data and catalogues from the first public data release of eROSITA-DE All-

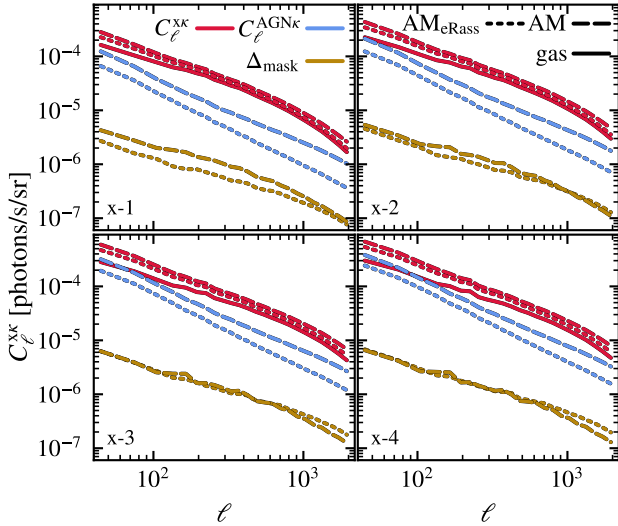


**Figure 10.** The ROSAT-DES-Y3 X-ray–lensing cross-correlations for the fiducial L1\_m9 simulation when we include only the X-ray emission from hot gas (solid red curve) and when contaminated by the X-ray emission from unresolved AGN (AM, see §3.2.2) for either the RASS (AM; dashed red curves, as used throughout this paper) or eRASS (AM<sub>eRASS</sub>; dotted red curves) resolution and flux limits (as discussed in the text). The tomographic bin is indicated in the lower left corner of each panel. The blue curves correspond to the cross-correlation between the lensing signal and the X-ray emission from the unresolved AM AGN,  $C_{\ell}^{\text{AGN}k}$  (as indicated by the legend). The golden coloured curves (labelled  $\Delta_{\text{mask}} C_{\ell}^{\text{XK}}$ ) show the impact of the binary mask (that is applied to the AGN contaminated X-ray maps) on the measured cross-correlation, as described in the text. The X-ray–lensing cross-correlation with eRASS-like masking is less effected by unresolved AGN due to the greater number of resolved point sources that are masked.

Sky Survey (eRASS1<sup>17</sup>, Merloni et al. 2024; Bulbul et al. 2024) have already been utilised to examine 2-point correlation functions (e.g. Seppi et al. 2024; Comparat et al. 2025), X-ray angular power spectra (e.g. Lau et al. 2025), cluster gas fractions (e.g. Popesso et al. 2025) and X-ray cluster scaling relations (e.g. Ramos-Ceja et al. 2025). Furthermore, the cluster catalogues of the currently available eRASS data releases have been mapped to the weak-lensing data from the overlapping footprints of the DES-Y3, KiDS (e.g., KiDS-1000 and KiDS-Legacy samples; Kuijken et al. 2019; Wright et al. 2025) and HSC (e.g., the year 3 data release Li et al. 2022) catalogues as demonstrated in the eRASS1 mass calibration (e.g. Grandis et al. 2024; Kleinebreil et al. 2025). It is possible to measure an X-ray–cosmic-shear cross-correlation with eROSITA as all the required data are currently available.

A greater number of point sources are able to be resolved, down to lower fluxes, in the eRASS data than in RASS as it is a deeper survey with better angular resolution (relevant discussions and comparisons by e.g. Merloni et al. 2024; Zheng et al. 2024). Therefore, adopting the improved resolution and lower flux limits of eRASS should reduce the impact of X-ray contamination from unresolved AGN on the X-ray–lensing cross-correlations. Here, we briefly examine what these potential improvements would imply for our results by recomputing the AM contaminated cross-correlation for the fiducial L1\_m9 simulation (as shown in Fig. 1) from X-ray all-sky maps at  $N_{\text{side}} = 8192$  (corresponding to a maximum pixel radius

of  $\sim 26.9 \approx \text{arcseconds}$ ) instead of 2048 and now masking (as outlined in §3.1.3) all AGN with flux (in the soft band,  $0.5 - 2.0 \text{ keV}$ ) above  $5 \times 10^{-14} \text{ erg s}^{-1} \text{ cm}^{-2}$ , matching the flux limits indicated by Seppi et al. (2022); Merloni et al. (2024); Lau et al. (2025); Toptun et al. (2025). The masked all-sky maps are then down sampled to  $N_{\text{side}} = 1024$  and the cross-correlation is re-computed. Even higher resolution maps (indicated by  $N_{\text{side}}$ ) are possible for the eRASS data, however that is not computationally feasible for this study. In Fig. 10 we show the impact of adopting this eRASS-like masking. Here, we compare the AM AGN contaminated cross-correlations with the eRASS-like masking of unresolved AGN (AM<sub>eRASS</sub>; dotted red curves) to the predicted AM AGN contaminated cross-correlation with RASS-like masking (AM; dashed red curves) and the uncontaminated (gas only) cross-correlation (gas; solid red curve). Additionally we overlay the predicted cross-correlation between cosmic shear and the X-ray emission from unresolved AGN (blue curves, indicated by the legend). The reader can ignore the golden coloured curves for now as we will return to them shortly. The tomographic bin is indicated in the lower left corner of each panel.

In Fig. 10, we see that masking with higher  $N_{\text{side}}$  maps and adopting lower flux limits within our analysis would reduce the impact of contamination from unresolved AGN on the X-ray–lensing cross-correlation over all angular scales considered. Specifically, we find this eRASS-like masking leads to a  $\approx 17\%$  reduction in the contaminated X-ray–lensing cross-correlations in each tomographic bin and suppresses the signal of the unresolved AGN only cross-correlation by  $\approx 47\%$  on average. However, the decrease in power of the X-ray–lensing cross-correlations presented in Fig. 10 is not only due to the reduced X-ray emission from unresolved AGN, it is partially due to the impact of the binary mask applied to the X-ray all-sky map.

As stated in §3.1.3, when we construct contaminated X-ray all-sky maps, we follow the binary masking scheme of Ferreira et al. (2024) and simply mask all pixels containing a resolved point source, i.e. any pixel containing an AGN above a given photon flux threshold ( $f_{\text{lum}} = 0.02 \text{ photon s}^{-1}$  for ROSAT-like all-sky maps). A consequence of masking all pixels that contain a resolved point source is that the desired X-ray emission from hot gas within the pixel is also masked. This limits the available information about the distribution of hot gas and reduces the power of the cross-correlation (see example in Appendix E). X-ray bright AGN are biased to lie within the central regions of gas-rich and likely X-ray bright haloes, where the lensing signal also peaks. Therefore the binary mask itself will also be correlated with both the lensing and X-ray maps. These additional correlations will affect the signal of the X-ray–lensing cross-correlation over specific ranges of angular scales, which we do not correct for in this paper.

We can reasonably approximate the total impact of the binary masks’ undesired effects (that is the correlations with the underlying maps and the loss of X-ray emission from hot gas) on the X-ray–lensing cross-correlation as the difference between the ‘full’ AGN contaminated cross-correlation (which utilises a masked X-ray map) and the sum of the gas only and unresolved AGN only cross-correlations,  $\Delta_{\text{mask}} = (C_{\ell}^{\text{gas}k} + C_{\ell}^{\text{AGN}k}) - C_{\ell}^{\text{XK}}$ . We overlay  $\Delta_{\text{mask}}$  in Fig. 10 to show the impact of the binary mask on the AM AGN contaminated cross-correlations in this work. Importantly, the undesired effects of the mask have only a minor impact on the results, as they account for a  $\leq 3\%$  change in the signal of the AM AGN contaminated cross-correlations. These effects are secondary to the binary masks’ main function, which is to remove the X-ray emission from resolved point sources. If we recompute the AM AGN contaminated cross-correlation (as shown in Fig. 10), without applying a binary mask (i.e. we include in the X-ray emission from resolved point sources),

<sup>17</sup> <https://erosita.mpe.mpg.de/dr1/>

then the cross-correlation (when assuming RASS-like masking) is increased by between 5% to 20%.

Finally, in Fig. 10 we can see that adopting the improved resolution and lower flux limit used in our eRASS-like masking approach further reduces the impact of the binary mask on some angular scales. However, if we apply our adopted eRASS flux limit to the lower resolution ROSAT X-ray all-sky maps ( $N_{\text{side}} = 2048$ ) we find, for both the AM and base AGN contamination cross-correlations, that such a significant portion of the sky is masked that the resultant contaminated cross-correlation has less power than the gas only cross-correlation at some angular scales (see appendix E). In future, studies should ensure that lower flux limits are accompanied by an increase in the resolution of the X-ray maps.

## 6 SUMMARY AND CONCLUSION

In this work we used the FLAMINGO suite of cosmological hydrodynamical simulations to explore the efficacy of the X-ray–cosmic-shear cross-correlation as a probe of large-scale structure and baryonic feedback. We computed the cross-correlation between synthetic X-ray and cosmic shear full-sky maps built from FLAMINGO’s suite of full-sky particle lightcones and HEALPix maps, as described in §3. We compared the predictions from FLAMINGO to the measurements of Ferreira et al. (2024). The X-ray all-sky maps were constructed in the soft band (0.5–2.0 keV) both with and without convolving the X-ray emission with the effective detector area of the ROSAT response matrix.

We explored the origin and robustness of the X-ray–lensing cross-correlation by decomposing the X-ray component of this probe by both halo mass and redshift before examining the cross-correlations’ sensitivity to systematic variations in the prescribed baryonic feedback, cosmology, simulation box size and resolution (§4.2). We found that the X-ray component of this cross-correlation is most sensitive to the distribution of hot gas in low redshift haloes with masses  $10^{14} \leq M_{200c}/M_{\odot} \leq 10^{15}$  (§4.2.1) and to changes in the strength of AGN feedback. However, we found the effects of variations in cosmology (specifically the  $\sigma_8$  parameter) and baryonic physics are largely degenerate (§4.2.2).

We compared the predictions from FLAMINGO with the cross-correlation, detected by Ferreira et al. (2024), between the cosmic shear data from the Dark Energy Survey (year 3 data release) and X-ray all-sky map from ROSAT (§4.3). We highlighted, through the use of a simple abundance matching approach (as described in §3.2.2), that the X-ray contamination from unresolved AGN cannot be neglected in such comparisons. The key finding is that an increased contribution from unresolved AGN to the cross-correlation, which is attainable by reducing the intrinsic scatter of the BH Luminosity – halo maximum circular velocity relation, allows FLAMINGO simulations calibrated to yield lower cluster gas fractions (parametrised to have stronger AGN feedback) to be consistent with the observations (§4.3.1).

In greater detail, our main findings are as follows:

- The X-ray component of the X-ray–lensing cross-correlation is dominated by the X-ray emission from hot gas within galaxy clusters at low redshifts (see §4.2.1). Decomposing a lightcone for the fiducial L1\_m9 FLAMINGO simulation by the redshift of the X-ray emitting gas reveals that hot gas at  $z \gtrsim 0.5$  is inconsequential for the cross-correlation. The contribution from hot gas decreases with redshift, however this redshift dependence is weaker for the cross-spectra in more distant (higher redshift) tomographic bins (Fig. 2).

- If we decompose the same lightcone by total halo mass,  $M_{200c}$ , we find that hot gas within  $R_{200c}$  of haloes accounts for 90–97% of the predicted cross-correlations signal for  $30 < \ell < 2048$  (Fig. 3). Moreover, haloes with  $M_{200c} \sim 10^{14} M_{\odot}$  dominate the cross-correlation at all angular scales, whilst more massive haloes,  $M_{200c} \geq 10^{15} M_{\odot}$ , are significant for  $\ell < 250$  but, their relative contribution diminishes towards smaller scales. The X-ray emission from haloes with  $M_{200c} < 10^{13.5} M_{\odot}$  accounts for  $\lesssim 5\%$  of the cross-correlation’s signal.

- The effects of variations in cosmology and baryonic physics on the X-ray–cosmic-shear cross-correlation are degenerate (§4.2.2). Relative to the fiducial L1\_m9 FLAMINGO simulation, varying either the cosmology or prescription of baryonic feedback results in changes to the predicted cross-correlation that are similar in magnitude and nearly independent of angular scale for  $30 < \ell < 2048$  (Fig. 4). Stronger AGN feedback (i.e. models calibrated on lower cluster gas fractions) suppresses the cross-correlation on all angular scales considered in this paper. Increasing the strength of stellar feedback has the same effect, but to a much lesser extent. The implementation of AGN feedback has a limited ( $\lesssim 10\%$ ) effect on the cross-correlation, where the cross-correlation for the ‘Jet’ mode of AGN feedback is slightly elevated relative to the fiducial thermal mode of feedback at both the smallest and largest angular scales considered ( $30 < \ell < 75$  and  $1720 \leq \ell < 2048$  respectively). Relative to the fiducial L1\_m9 FLAMINGO simulation, increasing the summed neutrino mass or adopting the ‘LS8’ lensing cosmology suppresses the cross-correlation, almost uniformly, across all angular scales.

- The predicted X-ray–lensing cross-correlations are converged with simulation box size but not with resolution (§4.2.3 and Fig. 5). However, this lack of convergence is the product of imperfect recalibration of the subgrid models at each resolution and differences in the thermodynamic profiles for fixed gas fractions. We find that an order of magnitude change in mass resolution, has a  $\approx 15\%$  effect on the measured cross-correlation whilst cosmic variance is a  $\leq 20\%$  effect and decreases with increasing  $\ell$  (Fig. 5). Both of cosmic variance and a change in mass resolution are secondary in effect to varying the cluster gas fraction in the simulations.

- Contamination in the form of X-ray emission from AGN unresolved by ROSAT has a non-negligible impact on the predicted X-ray–lensing cross-correlation and therefore must be considered when comparing model predictions with observations. We find that the X-ray emission from unresolved AGN ‘boosts’ the power of the X-ray–lensing cross-correlation on all angular scales included in this work (§4.1 and §4.3). The X-ray emission from unresolved AGN given by the ‘base’ black hole (BHs) particles (i.e. AGN as they naturally exist in FLAMINGO) has a smaller impact on the cross-correlation than the X-ray emission from unresolved AGN given by a simple abundance matching approach (Fig 1 and Fig. 6). These abundance matched (AM) AGN (i.e. BHs) are constrained to reproduce the observed quasar luminosity functions of Shen et al. (2020). The greater impact of the AM AGN is expected given that the base BHs underestimate the abundance of both bright and faint quasars (§3.2.2).

- Under the strong assumption that X-ray contamination from unresolved AGN is negligible we find the fiducial L1\_m9 FLAMINGO simulation is within  $0.3\sigma$  of the measurements by Ferreira et al. (2024) (Fig 1 and Table 2), whilst all other cluster gas fraction variations of the L1\_m9 simulation ( $f_{\text{gas}} \pm 2\sigma$ ,  $f_{\text{gas}} - 4\sigma$ ,  $f_{\text{gas}} - 8\sigma$ ) are discrepant by more than  $4.5\sigma$  (see the summary statistics in Table 3). On the other hand, accounting for the X-ray emission from unresolved AGN improves the agreement between the measured X-ray–lensing cross-correlation and the FLAMINGO simulations with

stronger baryonic feedback. If we include the X-ray contamination from unresolved AM AGN, the fiducial L1\_m9 simulation overestimates the observed data by  $4.3\sigma$ , however, the stronger baryonic feedback  $f_{\text{gas}}=2\sigma$  and  $f_{\text{gas}}=4\sigma$  simulations, are compatible with the observations (Fig. 6 and Table 3). In this scenario the strongest baryonic feedback variations in FLAMINGO ( $f_{\text{gas}}=8\sigma$  and LS8\_  $f_{\text{gas}}=8\sigma$ ) are discrepant with the observations to a  $2.3\sigma$  and  $7.4\sigma$  level respectively.

- The impact of X-ray emission from unresolved AGN on the X-ray–lensing cross-correlation can be increased or decreased by perturbing the intrinsic scatter in the BH Luminosity – halo maximum circular velocity relation (§4.3.1). Increasing (decreasing) the scatter reduces (boosts) the impact of contamination from unresolved  $\Delta\text{AM}$  AGN on the cross-correlation (Fig. 7). Irrespective of the scatter (at least within the confines of our  $\Delta\text{AM}$  model) the FLAMINGO simulation with weaker baryonic feedback than prescribed by the fiducial L1\_m9 simulation ( $f_{\text{gas}}+2\sigma$ ) is clearly irreconcilable with the measured dataset (discrepant at a  $> 14\sigma$  level; Fig. 8 and Fig. 9). However, within the range of sampled  $\Delta\text{AM}$  contaminated cross-correlations, the fiducial L1\_m9 simulation and all variations with stronger baryonic feedback ( $f_{\text{gas}}=2\sigma$ ,  $f_{\text{gas}}=4\sigma$ ,  $f_{\text{gas}}=8\sigma$  and LS8\_  $f_{\text{gas}}=8\sigma$ ) can be within  $2\sigma$  of the observations (Fig. 9).

- The X-ray–lensing cross-correlations predicted by FLAMINGO require stronger AGN feedback than given by the fiducial L1\_m9 model to be consistent with the measurements of Ferreira et al. (2024) (Fig. 8 and Fig. 9). Provided there is sufficient X-ray emission from unresolved AGN, the X-ray–lensing cross-correlation can be consistent with the strength of baryonic feedback (and cluster gas fractions) required by recent analyses of the kinetic Sunyaev-Zel'dovich (kSZ) effect (e.g. McCarthy et al. 2025; Bigwood et al. 2024, 2025; Siegel et al. 2025a) and inferred stacking of optically selected eROSITA clusters (Popesso et al. 2025). We find that, within the confines of the  $\Delta\text{AM}$  model, the impact of X-ray contamination from unresolved AGN can be increased (by reducing the induced scatter,  $\sigma_r$ ) such that the FLAMINGO simulations with the most extreme baryonic feedback (e.g.,  $f_{\text{gas}}=8\sigma$ ), which best reproduces kSZ effect measurements and stacks of eROSITA clusters, are consistent with the measurements of Ferreira et al. (2024) at a  $< 1\sigma$  level (when inducing a scatter of  $\sigma_r \approx 0.05 – 0.20$  dex), whilst the fiducial L1\_m9 simulation is discrepant by  $> 5\sigma$ . Conversely, we find the X-ray–lensing cross-correlations for the fiducial L1\_m9 simulation, which is fully consistent with the X-ray luminosity–halo mass and X-ray luminosity–temperature scaling relations of Eckert et al. (2025), can be compatible with the measurements of Ferreira et al. (2024) at a  $2\sigma$  level if we minimise the impact of X-ray contamination from unresolved AGN (an induced scatter of  $\sigma_r \geq 0.9$  dex in the  $\Delta\text{AM}$  model). In this scenario the  $f_{\text{gas}}=8\sigma$  simulation underestimates the observed X-ray–lensing cross-correlation by  $> 3.5\sigma$ .

We conclude that the X-ray–lensing cross-correlation is a potentially powerful probe of the distribution of hot gas in clusters relative to the underlying matter density field. However, the effectiveness of this probe is limited by the redshift depth and sensitivity to point source contamination of the X-ray all-sky measurements. With the currently published and upcoming, scheduled, data releases of the eRASS survey, we see opportunities to expand on the work presented in this paper. The eROSITA telescope will improve the constraining power of this probe as the impacts of unresolved AGN contamination are reduced due to the higher angular resolution and increased sensitivity relative to ROSAT. Moreover, as we venture further into the era of stage-IV galaxy surveys, the projected leaps in the precision and volume of the cosmic shear data, such as that offered by Eu-

clid (see relevant overviews in e.g. Euclid Collaboration et al. 2025; Prat & Bacon 2025), will complement the eROSITA X-ray surveys and maximise the effectiveness of X-ray–cosmic-shear joint analysis. As X-ray measurements remain one of the most valuable sources of information on the properties of hot gas in clusters, further exploration of X-ray all-sky measurements in joint analysis with adjacent low-redshift probes (such as the thermal Sunyaev-Zel'dovich e.g. La Posta et al. 2025) provides an exciting opportunity that may yield important insights into the interplay between baryonic feedback and large-scale structure.

## ACKNOWLEDGEMENTS

We thank David Alonso, Tassia Ferreira and Nora Elisa Chisari for allowing access to observed X-ray–cosmic-shear data and the useful discussions about the masking of point sources within the ROSAT all-sky maps. WM thanks Joey Braspenning, John Helly, Jeger Broxterman, Ian McCarthy and Rob McGibbon for the insightful discussions and assistance with (re-) computing both the ROSAT all-sky maps and cross-correlations used in this paper. This work is partly funded by the Dutch Research Council (NWO) programme Athena 184.034.002. WM acknowledges support by NWO through the Dark Universe Science Collaboration (OCENW.XL21.XL21.025). This work used the DiRAC@Durham facility managed by the Institute for Computational Cosmology on behalf of the STFC DiRAC HPC Facility ([www.dirac.ac.uk](http://www.dirac.ac.uk)). The equipment was funded by BEIS capital funding via STFC capital grants ST/K00042X/1, ST/P002293/1, ST/R002371/1 and ST/S002502/1, Durham University and STFC operations grant ST/R000832/1. DiRAC is part of the National e-Infrastructure.

## DATA AVAILABILITY

The data supporting the plots within this article are available on reasonable request to the corresponding author. The FLAMINGO simulation data (including the ROSAT-like X-ray all-sky maps created for this paper) will eventually be made publicly available, though we note that the data volume (several petabytes) may prohibit us from simply placing the raw data on a server. In the meantime, people interested in using the simulations are encouraged to contact the corresponding author.

## REFERENCES

Abbott T. M. C., et al., 2022, *Phys. Rev. D*, **105**, 023520  
 Abdalla E., et al., 2022, *Journal of High Energy Astrophysics*, **34**, 49  
 Ahn C. P., et al., 2014, *ApJS*, **211**, 17  
 Aihara H., et al., 2018, *PASJ*, **70**, S8  
 Aird J., Coil A. L., Georgakakis A., Nandra K., Barro G., Pérez-González P. G., 2015, *MNRAS*, **451**, 1892  
 Aird J., Coil A. L., Georgakakis A., 2017, *MNRAS*, **465**, 3390  
 Akino D., et al., 2022, *PASJ*, **74**, 175  
 Alonso D., Sanchez J., Slosar A., LSST Dark Energy Science Collaboration 2019, *MNRAS*, **484**, 4127  
 Amon A., et al., 2023, *MNRAS*, **518**, 477  
 Aricò G., Angulo R. E., Hernández-Monteagudo C., Contreras S., Zennaro M., 2021, *MNRAS*, **503**, 3596  
 Asgari M., et al., 2021, *A&A*, **645**, A104  
 Asgari M., Mead A. J., Heymans C., 2023, *The Open Journal of Astrophysics*, **6**, 39  
 Bahé Y. M., et al., 2022, *MNRAS*, **516**, 167

Bernyk M., et al., 2016, *The Astrophysical Journal Supplement Series*, 223, 9

Bigwood L., et al., 2024, *MNRAS*, 534, 655

Bigwood L., et al., 2025, *arXiv e-prints*, p. arXiv:2510.15822

Boller T., Freyberg M. J., Trümper J., Haberl F., Voges W., Nandra K., 2016, *A&A*, 588, A103

Booth C. M., Schaye J., 2009, *MNRAS*, 398, 53

Borrow J., Schaller M., Bower R. G., Schaye J., 2022, *MNRAS*, 511, 2367

Bourne M. A., Yang H.-Y. K., 2023, *Galaxies*, 11

Brandt W. N., Hasinger G., 2005, *ARA&A*, 43, 827

Brandt W. N., Yang G., 2022, in Bambi C., Sangangelo A., eds., *Handbook of X-ray and Gamma-ray Astrophysics*. Springer Nature Singapore, Singapore, p. 78, doi:10.1007/978-981-16-4544-0\_130-1

Braspenning J., et al., 2024, *MNRAS*, 533, 2656

Broxterman J. C., et al., 2024, *MNRAS*, 529, 2309

Bulbul E., et al., 2024, *A&A*, 685, A106

Chaikin E., Schaye J., Schaller M., Bahé Y. M., Nobels F. S. J., Ploeckinger S., 2022, *MNRAS*, 514, 249

Chisari N. E., et al., 2019, *The Open Journal of Astrophysics*, 2, 4

Comparat J., et al., 2019, *MNRAS*, 487, 2005

Comparat J., et al., 2023, *A&A*, 673, A122

Comparat J., et al., 2025, *A&A*, 697, A173

Crain R. A., van de Voort F., 2023, *ARA&A*, 61, 473

Debackere S. N. B., Schaye J., Hoekstra H., 2020, *MNRAS*, 492, 2285

Diego J. M., Sliwa W., Silk J., Barcons X., 2003, *MNRAS*, 344, 951

Ding B., Pizzati E., Schaye J., Hennawi J. F., McDonald W., Schaller M., 2025, *arXiv e-prints*, p. arXiv:2510.24283

Doux C., Karwal T., 2026, *The Open Journal of Astrophysics*, 9, 55045

Doux C., et al., 2022, *MNRAS*, 515, 1942

Eckert D., et al., 2016, *A&A*, 592, A12

Eckert D., Gastaldello F., O'Sullivan E., Finoguenov A., Brienza M., X-GAP Collaboration 2024, *Galaxies*, 12, 24

Eckert D., et al., 2025, *arXiv e-prints*, p. arXiv:2512.04203

Efstathiou G., 2025, *Philosophical Transactions of the Royal Society of London Series A*, 383, 20240022

Elbers W., Frenk C. S., Jenkins A., Li B., Pascoli S., 2021, *MNRAS*, 507, 2614

Elbers W., et al., 2025, *MNRAS*, 537, 2160

Euclid Collaboration et al., 2025, *A&A*, 697, A1

Faucher-Giguère C.-A., 2020, *Monthly Notices of the Royal Astronomical Society*, 493, 1614

Ferland G. J., et al., 2017, *Rev. Mex. Astron. Astrofis.*, 53, 385

Ferreira T., Alonso D., García-García C., Chisari N. E., 2024, *Phys. Rev. Lett.*, 133, 051001

Forouhar Moreno V. J., Helly J., McGibbon R., Schaye J., Schaller M., Han J., Kugel R., Bahé Y. M., 2025, *MNRAS*, 543, 1339

García-García C., Ruiz-Zapatero J., Alonso D., Bellini E., Ferreira P. G., Mueller E.-M., Nicola A., Ruiz-Lapuente P., 2021, *J. Cosmology Astropart. Phys.*, 2021, 030

Gatti M., et al., 2021, *MNRAS*, 504, 4312

Giblin B., et al., 2021, *A&A*, 645, A105

Grandis S., et al., 2024, *A&A*, 687, A178

Guachalla B. R., et al., 2025, *Phys. Rev. D*, 112, 103512

Górski K. M., Hivon E., Banday A. J., Wandelt B. D., Hansen F. K., Reinecke M., Bartelmann M., 2005, *The Astrophysical Journal*, 622, 759

Hadzhiyska B., et al., 2025, *Phys. Rev. D*, 112, 083509

Hahn O., Rampf C., Uhlemann C., 2021, *MNRAS*, 503, 426

Hajian A., Battaglia N., Spergel D. N., Bond J. R., Pfrommer C., Sievers J. L., 2013, *J. Cosmology Astropart. Phys.*, 2013, 064

Han J., Jing Y. P., Wang H., Wang W., 2012, *MNRAS*, 427, 2437

Han J., Cole S., Frenk C. S., Benítez-Llambay A., Helly J., 2018, *MNRAS*, 474, 604

Helgason K., Cappelluti N., Hasinger G., Kashlinsky A., Ricotti M., 2014, *The Astrophysical Journal*, 785, 38

Henden N. A., Puchwein E., Shen S., Sijacki D., 2018, *MNRAS*, 479, 5385

Hurier G., Aghanim N., Douspis M., 2014, *A&A*, 568, A57

Hurier G., Douspis M., Aghanim N., Pointecouteau E., Diego J. M., Macias-Perez J. F., 2015, *A&A*, 576, A90

Hurier G., Singh P., Hernández-Monteagudo C., 2017, *arXiv e-prints*, p. arXiv:1711.10774

Huško F., Lacey C. G., Schaye J., Schaller M., Nobels F. S. J., 2022, *MNRAS*, 516, 3750

Joachimi B., et al., 2021, *A&A*, 646, A129

Kilbinger M., 2015, *Reports on Progress in Physics*, 78, 086901

Kilbinger M., et al., 2017, *MNRAS*, 472, 2126

Kleinebreil F., et al., 2025, *A&A*, 695, A216

Kolodzig A., Gilfanov M., Hütsi G., Sunyaev R., 2016, *Monthly Notices of the Royal Astronomical Society*, 466, 3035–3059

Kolodzig A., Gilfanov M., Hütsi G., Sunyaev R., 2017, *Monthly Notices of the Royal Astronomical Society*, 473, 4653

Kugel R., et al., 2023, *MNRAS*, 526, 6103

Kugel R., Schaye J., Schaller M., Forouhar Moreno V. J., McGibbon R. J., 2025, *MNRAS*, 537, 2179

Kuijken K., et al., 2019, *A&A*, 625, A2

La Posta A., Alonso D., Chisari N. E., Ferreira T., García-García C., 2025, *Phys. Rev. D*, 112, 043525

Lahav O., Liddle A. R., 2022, *arXiv e-prints*, p. arXiv:2201.08666

Lake V., Huffenberger K. M., 2023, *MNRAS*, 518, 3251

Lau E. T., Bogdán Á., Nagai D., Cappelluti N., Shirasaki M., 2025, *ApJ*, 983, 8

Li X., et al., 2022, *PASJ*, 74, 421

López I. E., et al., 2024, *A&A*, 692, A209

Lucie-Smith L., et al., 2025, *Phys. Rev. D*, 112, 063541

McCarthy I. G., Schaye J., Bird S., Le Brun A. M. C., 2017, *MNRAS*, 465, 2936

McCarthy I. G., Bird S., Schaye J., Harnois-Deraps J., Font A. S., van Waerbeke L., 2018, *MNRAS*, 476, 2999

McCarthy I. G., et al., 2023, *MNRAS*, 526, 5494

McCarthy I. G., et al., 2025, *MNRAS*, 540, 143

McGibbon R., Helly J. C., Schaye J., Schaller M., Vandebroucke B., 2025, *Journal of Open Source Software*, 10, 8252

Merloni A., et al., 2024, *A&A*, 682, A34

Naess S., et al., 2020, *J. Cosmology Astropart. Phys.*, 2020, 046

Nicola A., García-García C., Alonso D., Dunkley J., Ferreira P. G., Slosar A., Spergel D. N., 2021, *Journal of Cosmology and Astroparticle Physics*, 2021, 067

Peebles P. J. E., 2022, *Annals of Physics*, 447, 169159

Peebles P. J. E., 2025, *Philosophical Transactions of the Royal Society of London Series A*, 383, 20240021

Perivolaropoulos L., Skara F., 2022, *New Astron. Rev.*, 95, 101659

Pizzati E., Hennawi J. F., Schaye J., Schaller M., 2024, *MNRAS*, 528, 4466

Planck Collaboration et al., 2020, *A&A*, 641, A6

Ploeckinger S., Schaye J., 2020, *MNRAS*, 497, 4857

Popesso P., et al., 2025, *A&A*, 704, A278

Prat J., Bacon D., 2025, *arXiv e-prints*, p. arXiv:2501.07938

Predehl P., et al., 2021, *A&A*, 647, A1

Ramos-Ceja M. E., et al., 2025, *arXiv e-prints*, p. arXiv:2511.14356

Reid B., et al., 2016, *MNRAS*, 455, 1553

Ren K., Trenti M., 2021, *The Astrophysical Journal*, 923, 110

Ren K., Trenti M., Di Matteo T., 2020, *ApJ*, 894, 124

Salcido J., McCarthy I. G., Kwan J., Upadhye A., Font A. S., 2023, *MNRAS*, 523, 2247

Schaan E., et al., 2021, *Phys. Rev. D*, 103, 063513

Schaller M., et al., 2024, *MNRAS*,

Schaller M., Schaye J., Kugel R., Broxterman J. C., van Daalen M. P., 2025, *MNRAS*, 539, 1337

Schaye J., Dalla Vecchia C., 2008, *MNRAS*, 383, 1210

Schaye J., et al., 2015, *MNRAS*, 446, 521

Schaye J., et al., 2023, *MNRAS*, 526, 4978

Schneider A., Teyssier R., Stadel J., Chisari N. E., Le Brun A. M. C., Amara A., Refregier A., 2019, *J. Cosmology Astropart. Phys.*, 2019, 020

Schneider A., Giri S. K., Amodeo S., Refregier A., 2022, *MNRAS*, 514, 3802

Semboloni E., Hoekstra H., Schaye J., van Daalen M. P., McCarthy I. G., 2011, *MNRAS*, 417, 2020

Seppi R., et al., 2022, *A&A*, 665, A78

Seppi R., et al., 2024, *A&A*, 686, A196

Sevilla-Noarbe I., et al., 2021, *The Astrophysical Journal Supplement Series*, 254, 24

Shen X., Hopkins P. F., Faucher-Giguère C.-A., Alexander D. M., Richards G. T., Ross N. P., Hickox R. C., 2020, *MNRAS*, 495, 3252

Shirasaki M., Lau E. T., Nagai D., 2020, *MNRAS*, 491, 235

Siegel J., et al., 2025a, *arXiv e-prints*, p. arXiv:2509.10455

Siegel J., et al., 2025b, *arXiv e-prints*, p. arXiv:2512.02954

Singh P., Refregier A., Majumdar S., Nath B. B., 2016, *Monthly Notices of the Royal Astronomical Society*, 466, 3961

Snowden S. L., et al., 1997, *ApJ*, 485, 125

Springel V., Di Matteo T., Hernquist L., 2005, *MNRAS*, 361, 776

Sunyaev R., et al., 2021, *A&A*, 656, A132

Toptun V., et al., 2025, *A&A*, 700, A167

Upadhye A., et al., 2024, *MNRAS*, 529, 1862

Vogelsberger M., Marinacci F., Torrey P., Puchwein E., 2020, *Nature Reviews Physics*, 2, 42

Voges W., 1993, *Advances in Space Research*, 13, 391

Voges W., et al., 1999, *A&A*, 349, 389

Wiersma R. P. C., Schaye J., Theuns T., Dalla Vecchia C., Tornatore L., 2009, *MNRAS*, 399, 574

Wright A. H., et al., 2025, *A&A*, 703, A158

Yang T., et al., 2025, *arXiv e-prints*, p. arXiv:2512.09891

Zentner A. R., Semboloni E., Dodelson S., Eifler T., Krause E., Hearin A. P., 2013, *Phys. Rev. D*, 87, 043509

Zheng X., et al., 2024, *A&A*, 681, A77

Zhou Y., Mitsuda K., Yamasaki N. Y., 2022, *The Astrophysical Journal*, 929, 128

Zou F., Yu Z., Brandt W. N., Tak H., Yang G., Ni Q., 2024, *The Astrophysical Journal*, 964, 183

van Daalen M. P., Schaye J., Booth C. M., Dalla Vecchia C., 2011, *MNRAS*, 415, 3649

van Daalen M. P., McCarthy I. G., Schaye J., 2020, *MNRAS*, 491, 2424

## APPENDIX A: X-RAY EMISSION IN FLAMINGO

In this appendix we show the impact of the ROSAT response matrix, along with other key choices relating to computing the X-ray emission from both hot gas and point sources (AGN and XRBs), on the ROSAT-like X-ray all-sky maps and X-ray–lensing cross-correlations described in §3.

In Fig. A1 we show the ratio between the X-ray–lensing cross-correlations when the X-ray emission from hot gas is ( $C_{\ell}^{x \times k}$ ) and is not ( $C_{\ell}^{xk}$ ) convolved with the ROSAT response matrix. We present this ratio in each tomographic bin for the cluster gas fraction variations of the fiducial L1\_m9 simulation. For a given feedback variation, the ratio between the convolved and ‘normalised’ cross-correlations is fairly consistent across all tomographic bins. Furthermore, the offset of each feedback variation from the fiducial model is also consistent across all tomographic bins.

As described in §3.1.1, when constructing new X-ray all-sky maps from a PLC we exclude the X-ray emission from particles that have been recently heated by AGN emission (recently heated particles; RHPs), correct the scale used to identify if smoothing should be applied to the map and rotate the all-sky maps to avoid replicating the same structures along the line of sight. Particles that have been recently heated by AGN feedback can temporarily have high temperatures and densities, leading to them being unrealistically X-ray bright (further details given by relevant sections of Braspenning et al. 2024; Schaye et al. 2023). When constructing smoothed all-sky maps gas particle properties are smoothed on the sky, where all pixels whose centres lie within a search radius  $\theta_s$  may be updated based on a weighting function as described in Appendix A2 of Schaye et al.

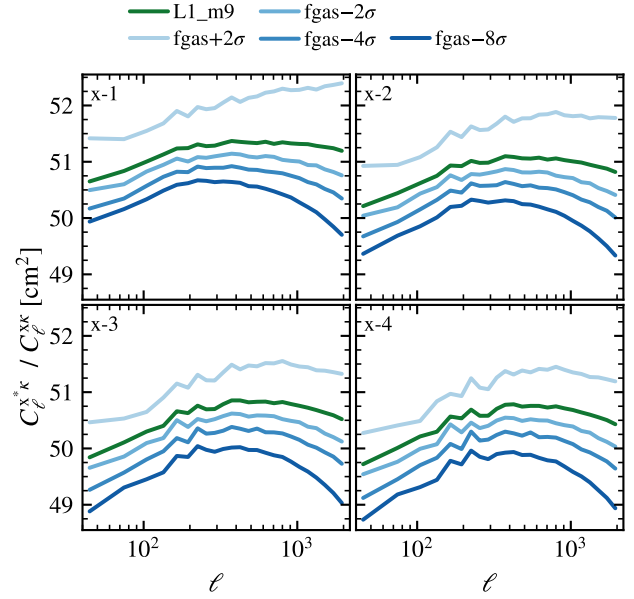


**Figure A1.** The ratio of the X-ray–lensing cross-correlation for the L1\_m9 cluster gas fraction variations (indicated by colour), in each tomographic bin, when the X-ray emission from hot gas is convolved with the ROSAT response matrix ( $C_{\ell}^{x \times k}$ ) and when it is not ( $C_{\ell}^{xk}$ ). The tomographic bin is indicated in the upper left corner of each panel.

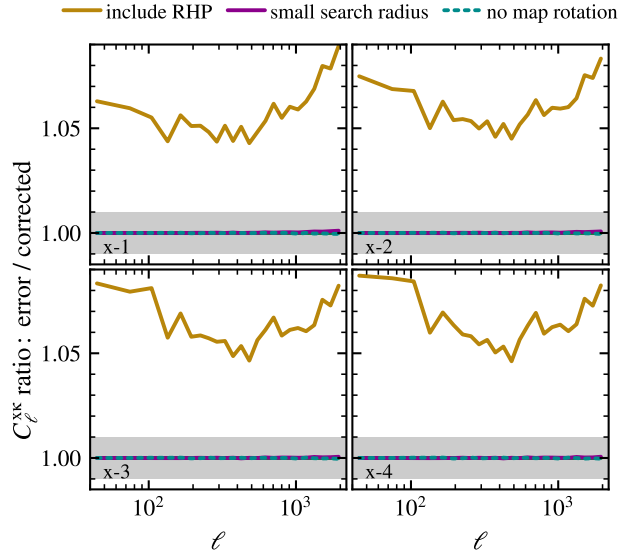


**Figure A2.** The ratio between the X-ray–lensing cross-correlation of the L1\_m9 simulation when only the X-ray emission from hot gas is included and for when the X-ray emission from recently heated particles (RHPs) is included (gold curve), the smoothing search radius is not corrected (i.e. too small: purple curve), and when the all-sky maps are not rotated to avoid replication of structures when integrating the X-ray emission along the line-of-sight (cyan dotted curve). The tomographic bin is indicated in the lower left corner of each panel. The X-ray emission is not convolved with the ROSAT response matrix.

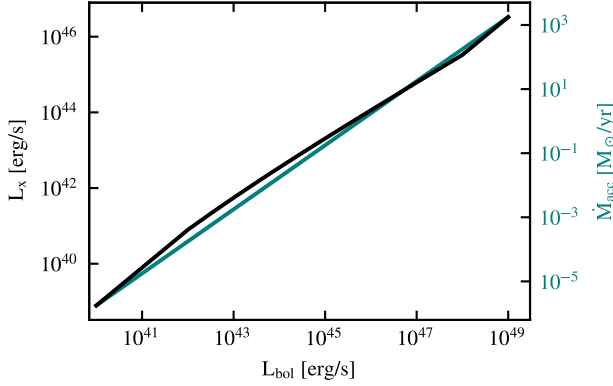


**Figure A3.** The relation of the X-ray Luminosity ( $L_x$ ) and Bolometric Luminosity ( $L_{\text{bol}}$ ) given by the adopted bolometric correction factor (as detailed in the text). Additionally, the relation between the black hole mass accretion rate ( $\dot{M}_{\text{accr}}$ ) and Bolometric Luminosity is shown by the cyan curve and right-most y-axis.

(2023). The search radius is given by

$$\theta_s = \gamma \arctan(h/r) \quad (\text{A1})$$

where  $h$  is the particle's SPH smoothing length,  $r$  is the distance from the particle to the observer and  $\gamma$  is the radius at which the SPH smoothing kernel falls to zero in units of smoothing length. The all-sky smoothed HEALPix maps were created on-the-fly and erroneously used a search radius computed with  $\gamma = 1$  when comparing the search radius to the angular radius of a pixel to identify if smoothing should be applied for a given gas particle.  $\gamma = 1$  is smaller than  $1$  in this instance  $\gamma = 1$  is smaller than the correct values and the smaller search radius results in a fraction of particles that would otherwise have been smoothed, updating only a singular pixel instead. For example, the correct value of  $\gamma$  of the fiducial L1\_m9 simulation is larger by a factor of 1.8 and therefore particles with  $\theta_s = 1$ -1.8 times the maximum pixel radius would not have been smoothed, when they otherwise should have. As the size of the search radius only affected whether or not smoothing was applied for a given particle it did not affect how, or which, pixels were updated when smoothing was applied. In our work we adopt the correct values of  $\gamma$ , which has a minimal effect on the resultant cross-correlations as seen in Fig. A1.

In Fig. A2 we present the ratio between the X-ray-lensing cross-correlation computed for the fiducial L1\_m9 simulation, as shown in Fig. 4, and the cross-correlations when we include the X-ray emission from RHPs (gold curve), do not correct the small search radius (purple solid curve) or do not rotate the all-sky maps whilst integrating along the X-ray emission along the line-of-sight (cyan dotted curve). The ratio is shown for each tomographic bin and the X-ray emission from hot gas was not convolved with the ROSAT response matrix. As can be seen, for the range of angular scales we consider in this paper, rotating the X-ray all-sky maps to avoid the replication of structures along the line of sight and correcting the size of the smoothing kernel have almost no impact. However, by comparison, filtering out recently heated gas particles has a small but a noticeable effect on the resultant X-ray-lensing cross-correlation.

As described in §3.1.2, we estimate the photon count rate of AGN from the bolometric luminosities ( $L_{\text{bol}}$ ) of BH particles, which we convert to X-ray luminosities ( $L_x$ ) in the soft band (0.5–2 keV) using a bolometric correction factor. We adopted the bolometric correction factor given by equation 5 and the parameters (for the soft X-ray band) in Table 1 of Shen et al. (2020). Additionally, as detailed in

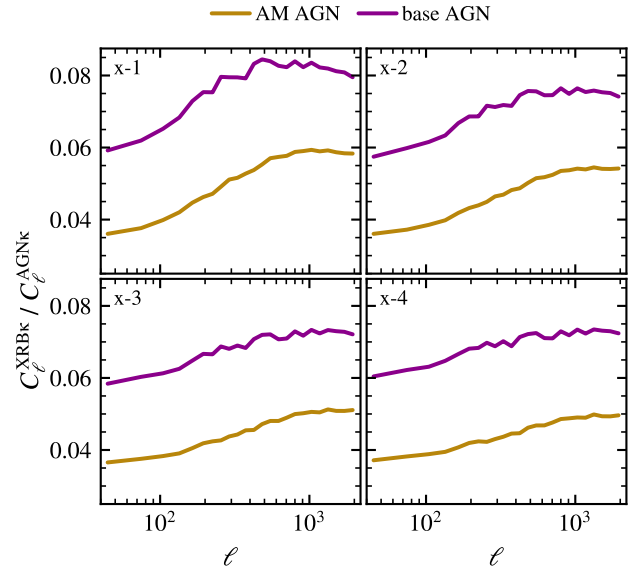


**Figure A4.** The ratio between the X-ray-lensing cross-correlation of the L1\_m9 simulation when the X-ray emission is only from X-ray binaries (XRBs) and when the X-ray emission is only from unresolved AGN, either AM AGN (gold curves) or base AGN (purple curves). The X-ray emission from X-ray binaries (XRBs) is described in the text. The contribution of unresolved AGN to the X-ray-lensing cross-correlation is more than an order of magnitude greater than that of XRBs. The tomographic bin is indicated in the upper left corner of each panel.

§3.1.2, we extended this function to allow for bolometric luminosities both higher and lower than the fit by Shen et al. (2020). The resultant relation between X-ray and bolometric luminosity given by the correction function is shown in Fig. A3. Furthermore, in Fig. A3 we also show the relation between the bolometric luminosity and the mass accretion rate of the BHs ( $L_{\text{bol}} = \dot{M}_{\text{accr}} \epsilon c^2$ ).

In Fig. A4 we demonstrate, with the fiducial L1\_m9 simulation, that X-ray emission from XRBs makes a negligible contribution to the X-ray-lensing cross-correlation in comparison to the X-ray emission from unresolved AGN. We construct all-sky maps of the X-ray emission from XRBs for redshifts  $z \leq 3$  from the all-sky stellar mass HEALPix maps and the star formation rates of gas within  $R_{200c}$  of haloes identified in the halo-lightcone. We estimate the X-ray emission from XRBs as given by equation 5 (or model 5 in table 2) of Aird et al. (2017). The X-ray-lensing cross-correlation of the fiducial L1\_m9 simulation when the X-ray emission is from only XRBs ( $C_ell^XRBK$ ) is more than an order of magnitude weaker than the corresponding cross-correlation when X-ray emission is from either the base AGN (purple curve) or AM AGN (gold curve).

## APPENDIX B: QUASAR LUMINOSITY AND MAXIMUM CIRCULAR VELOCITY FUNCTIONS

In this appendix we examine the quasar luminosity function (QLF) in one lightcone of the fiducial L1\_m9 simulation and show the convergence of the maximum circular velocity function with resolution, which both relate to the abundance matching approach that we use to model unresolved AGN, as described in §3.2.

The QLFs for the suite of FLAMINGO simulations are presented, at multiple redshifts, by Ding et al. (2025). Specifically, Ding et al.

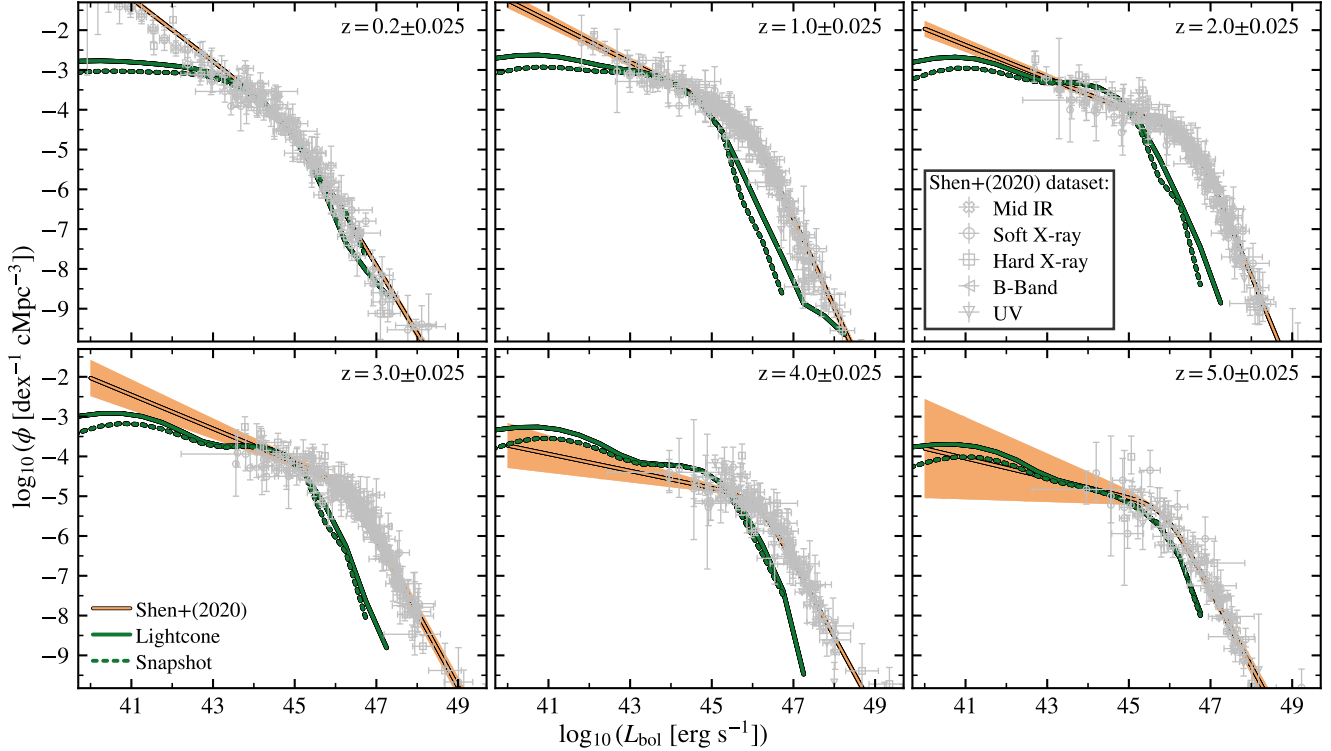


**Figure B1.** The bolometric quasar luminosity functions for the FLAMINGO L1\_m9 simulation computed from the particle lightcone (solid green curve) and the most massive black hole per subhalo from the snapshot data (dotted green curve) compared to the [Shen et al. \(2020\)](#) fits to observations (solid orange curve) and their compilation of observational datasets (grey markers). The shaded region gives the associated  $\pm 1\sigma$  uncertainty for each fit to the observed QLF. The redshift of each QLF is indicated in the upper right corner of each panel, with the  $\pm$  showing the sampled redshift range from the lightcone.

(2025) showed that L1\_m9 underestimates the abundance of bright quasars for redshifts  $z \gtrsim 1$ .

In Fig. B1 we confirm that the underabundance of bright and faint quasars shown by [Ding et al. \(2025\)](#) for the fiducial L1\_m9 simulation snapshots (with the simulations full volume) is also present in the lightcones. Here, we construct QLFs from the base BHs of the L1\_m9 PLC using redshift bin widths of  $\Delta z = 0.05$  centred on  $z = 0.2, 1, 2, 3, 4$  and  $5$ , within which we use 20 evenly log-spaced bins of the range  $10^{40} \leq L_{\text{bol}} \leq 10^{50} \text{ erg s}^{-1}$ . We compare the QLFs for the lightcone (solid green curve) with those computed from the snapshots (using the most massive BH per subhalo, as in [Ding et al. \(2025\)](#); dotted green curve) and the observations given by [Shen et al. \(2020\)](#) (solid orange curve, the shaded region indicates  $\pm\sigma$ ). These observed QLFs are the ones we sample from in our abundance matching scheme, described in §3.2.2. Additionally, in Fig. B1, we overlay the observed datasets compiled by [Shen et al. \(2020\)](#).

The lightcone QLFs have a greater abundance of faint quasars than the snapshot QLFs, because the lightcone QLFs include all BH particles in the lightcone whereas the snapshot QLFs include only the most massive BH (MMBH) per subhalo. For redshifts  $z \leq 1$  the lightcone QLF has an underabundance of bright quasars relative to the snapshots due to cosmic variance. Compared to the observations, both sets of FLAMINGO QLFs underestimate the abundance of both bright and faint quasars which, as discussed by [Ding et al. \(2025\)](#), is likely due to the limited temporal and spatial resolution of FLAMINGO.

The top panel of Fig. B2 presents the maximum circular velocity ( $v_{\text{max}}$ ) function, at redshift  $z = 0.1$ , for the low, intermediate and high resolution 1 Gpc box size simulations (L1\_m10, L1\_m9 and

L1\_m8, respectively). For each resolution we show the fiducial dark matter only (DMO; dashed curves) and hydrodynamic (HYDRO; solid curves) variations. The  $v_{\text{max}}$  function was computed from all haloes with at least 100 particles in a snapshot at  $z = 0.1$  using 100 equal width logarithmic bins for  $v_{\text{max}} < 10^4 \text{ km s}^{-1}$ . The shaded regions indicate the  $1\sigma$  Poisson error for the corresponding hydrodynamic simulation (indicated by colour). The bottom panel depicts the total halo mass ( $M_{200c}$ ) of central haloes as a function of  $v_{\text{max}}$  at  $z = 0.1$  for the same simulations as in the top panel. Each curve indicates the median halo mass,  $M_{200c}$ , per velocity bin, whilst shaded regions outline the 16<sup>th</sup> to 84<sup>th</sup> percentiles. As shown in Fig. B2,  $v_{\text{max}}$  is well converged with resolution and is a robust indicator of the total dynamical mass within a subhalo, especially for haloes with  $M_{200c} > 10^{13} \text{ M}_{\odot}$ .

## APPENDIX C: SUPPLEMENTARY RESULTS

In this appendix we provide supplementary results and repeat figures presented in §4, but showing all tomographic bins instead of only the third tomographic bin (x-3). For each of the figures shown, the conclusions drawn from the corresponding figures in the main text (§4) hold when looking at all tomographic bins.

Figs. C1, C2 and C3, corresponding to Fig. 3, 4 and 5 in §4.2, respectively, show the idealised cross-spectra (where we only include the X-ray emission from hot gas and do not convolved with the ROSAT response matrix) in each tomographic bin. In Fig. C4 we repeat the comparisons between FLAMINGO and the observations shown in Fig. 6 but now for each tomographic bin. Here we show

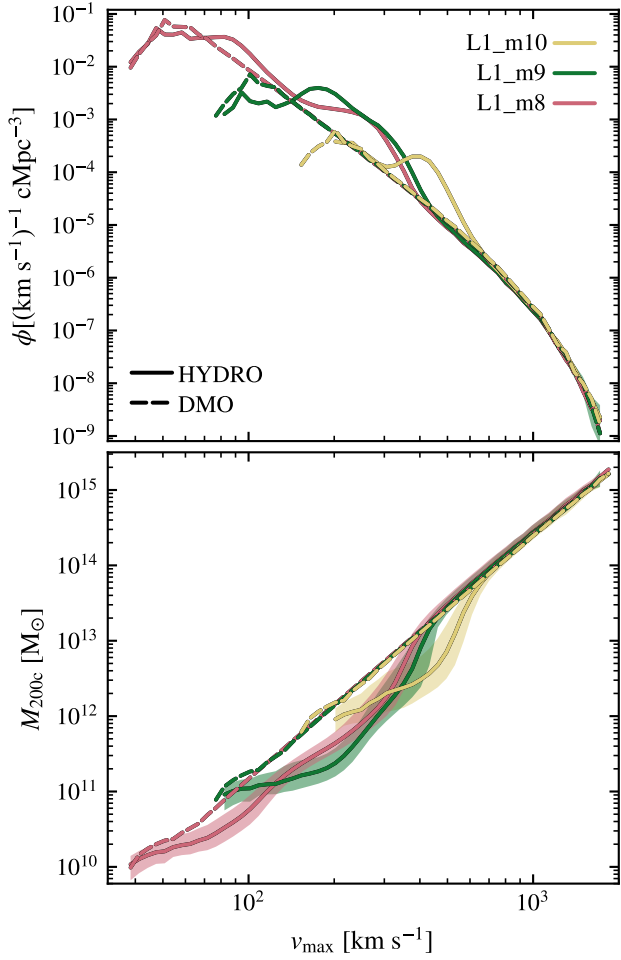


**Figure B2.** *Top:* The maximum circular velocity ( $v_{\max}$ ) functions ( $\phi$ ) at redshift  $z = 0.1$  for both the fiducial hydrodynamic (HYDRO; solid curves) and dark matter only (DMO; dashed curves) (1 Gpc) $^3$  box simulations at each of the available resolutions. These  $v_{\max}$  functions include all subhaloes with at least 100 particles. There is good convergence between the low (L1\_m10), intermediate (L1\_m9) and high resolutions (L1\_m8) at redshift  $z = 0.1$ . *Bottom:* The median (solid and dashed lines) mass of central haloes ( $M_{200c}$ ) as a function of  $v_{\max}$ . The shaded regions indicates the 16<sup>th</sup> – 84<sup>th</sup> percentiles per  $v_{\max}$  bin.

the predicted FLAMINGO X-ray-lensing cross-correlation when we include the X-ray emission from only hot gas (left column), when the X-ray emission is contaminated by unresolved AGN given by the base BHs (centre column) or AM BHs (right column). For each simulation we compute the  $\chi^2$  value between the predicted X-ray-lensing cross-correlation and the measurements of Ferreira et al. (2024) (black points and error bars). In each panel we print the corresponding  $\chi^2$  value for the fiducial L1\_m9 simulation and in parentheses we show the difference in  $\chi^2$  ( $\Delta\chi^2$ ) for each feedback variation and the fiducial L1\_m9 simulation. As discussed in §4.1, we see that the impact of unresolved AGN increases in more distant tomographic bins and the noise of the measured dataset is greatest in the first tomographic bin.

Table C1 presents the sum of  $\chi^2$  values (top panel) and number of standard deviations ( $N_\sigma$ ; bottom panel) of the  $\Delta\text{AM}$  AGN contaminated X-ray-lensing cross-correlations (as shown in Figs. 8 and 9) with respect to the measurements of Ferreira et al. (2024). Each column lists the summary statistics ( $\chi^2$  and  $N_\sigma$ ) for each of the baryonic feedback variations shown in Fig. 9 when the  $\Delta\text{AM}$  AGN

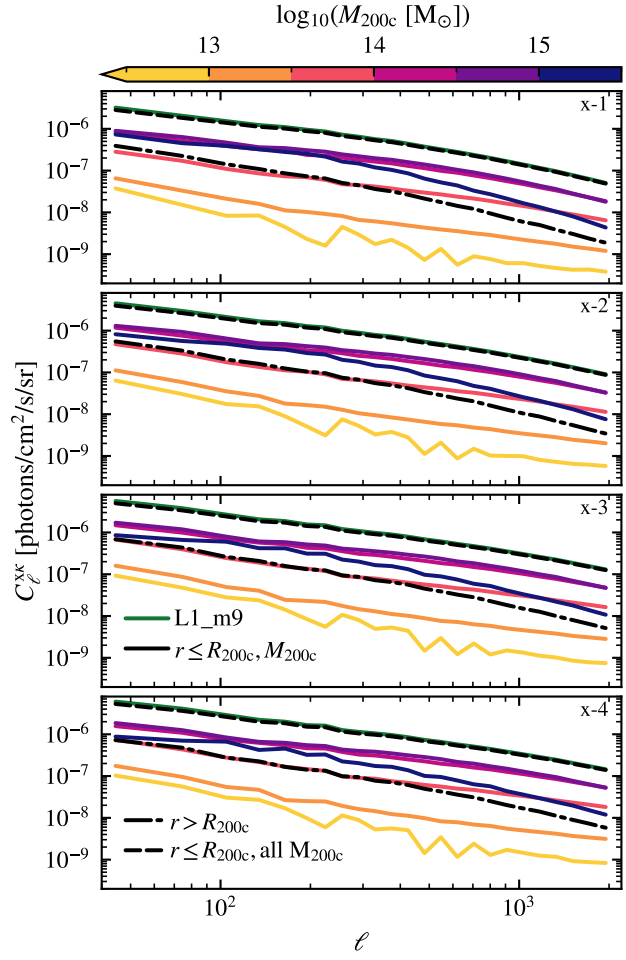


**Figure C1.** The same as Fig. 3, but repeated for each tomographic bin, which is indicated in the upper right corner of each panel.

contaminated cross-correlation is constructed with a given value of  $\sigma_r$ , the log-normal scatter imposed on the BH Luminosity – maximum circular velocity relation (see §3.2.2), which is indicated in the top row of the table.

#### APPENDIX D: SENSITIVITY TO BOX SIZE AND RESOLUTION: HALO SCALING RELATIONS

As shown by Fig. 5, the X-ray-lensing cross-correlation for FLAMINGO is converged with box size but not with resolution. In this appendix we use the cluster gas fraction – halo mass and X-ray luminosity – halo mass relations to demonstrate why the cross-correlation for the high-resolution (L1\_m8) FLAMINGO simulation is suppressed relative to the intermediate-resolution (L1\_m9) simulation.

In Fig. D1 we examine the convergence of the gas fraction ( $f_{\text{gas}, M_{500c}}$ ) – halo mass ( $M_{500c}$ ) scaling relation with resolution at  $z = 0.1, 0.25$  and  $0.5$  (the X-ray-lensing cross-correlation is dominated by X-ray emission from  $z \leq 0.5$ , see Fig. 2). The solid curves present the median relations for each resolution, at a fixed box size (1 Gpc), relative to the fiducial L1\_m9 simulation for clusters at redshifts  $z = 0.1$  (top panel),  $z = 0.25$  (middle panel) and  $z = 0.5$  (bottom panel). For comparison we overlay the  $+2\sigma$ ,  $-2\sigma$  and  $-8\sigma$

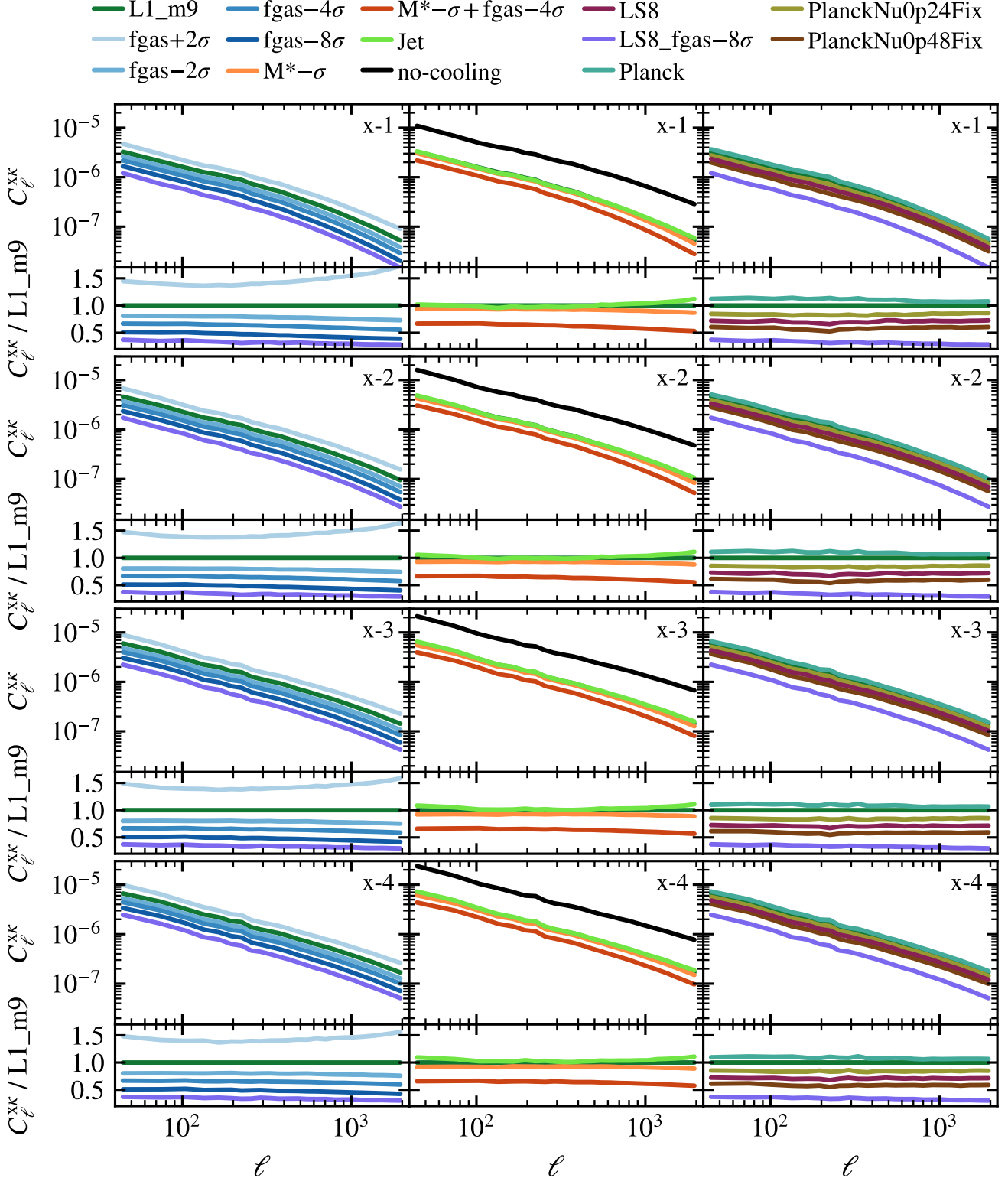


**Figure C2.** The same as Fig. 4, but for each tomographic bin, which is printed in the upper right corner of each main panel.

**Table C1.** The  $\chi^2$  (top panel) and  $N_\sigma$  (bottom panel) values (as computed for Table 3 discussed in §4.3) for the  $\Delta$ AM AGN contaminated cross-correlations of selected FLAMINGO L1\_m9 simulations with respect to the measurements of Ferreira et al. (2024). The populations of  $\Delta$ AM BHs are parametrised by  $\sigma_r$ , which describes the log-normal scatter imposed on the halo maximum circular velocities during abundance matching as described in §4.3.1. The left-most column lists the FLAMINGO simulation identifier, while each subsequent column gives the corresponding  $\chi^2$  (top panel) and  $N_\sigma$  (bottom panel) values, for the  $\sigma_r$  value listed at the top of the column.

Identifier	$\sigma_r$ [dex]												
	0.00	0.05	0.10	0.15	0.20	0.25	0.30	0.35	0.40	0.45	0.50	0.55	0.60
L1_m9	339	317	266	217	186	167	154	148	142	138	135	133	131
fgas+2 $\sigma$	740	711	649	583	541	510	493	483	471	466	458	452	449
fgas-2 $\sigma$	212	195	157	125	105	97.1	92.8	90.8	89.6	89.0	88.7	88.5	88.3
fgas-4 $\sigma$	153	140	114	95.8	89.1	88.8	90.3	92.2	94.0	95.4	96.7	97.8	98.7
fgas-8 $\sigma$	115	108	98	98	106	116	124	131	136	140	142	145	149
LS8_fgash-8 $\sigma$	108	109	120	141	165	184	198	207	214	220	225	228	231
L1_m9	11.1	10.4	8.52	6.59	5.18	4.27	3.62	3.26	2.97	2.74	2.57	2.46	2.34
fgas+2 $\sigma$	21.2	20.6	19.3	17.8	16.8	16.0	15.5	15.3	15.0	14.8	14.6	14.4	14.4
fgas-2 $\sigma$	6.37	5.62	3.77	1.94	0.70	0.13	0.00	0.00	0.00	0.00	0.00	0.00	0.00
fgas-4 $\sigma$	3.56	2.82	1.27	0.04	0.00	0.00	0.00	0.00	0.00	0.01	0.10	0.17	0.24
fgas-8 $\sigma$	1.36	0.88	0.15	0.16	0.76	1.37	1.90	2.30	2.59	2.82	2.97	3.11	3.22
LS8_fgash-8 $\sigma$	0.89	0.97	1.62	2.90	4.15	5.09	5.75	6.15	6.47	6.71	6.90	7.05	7.18

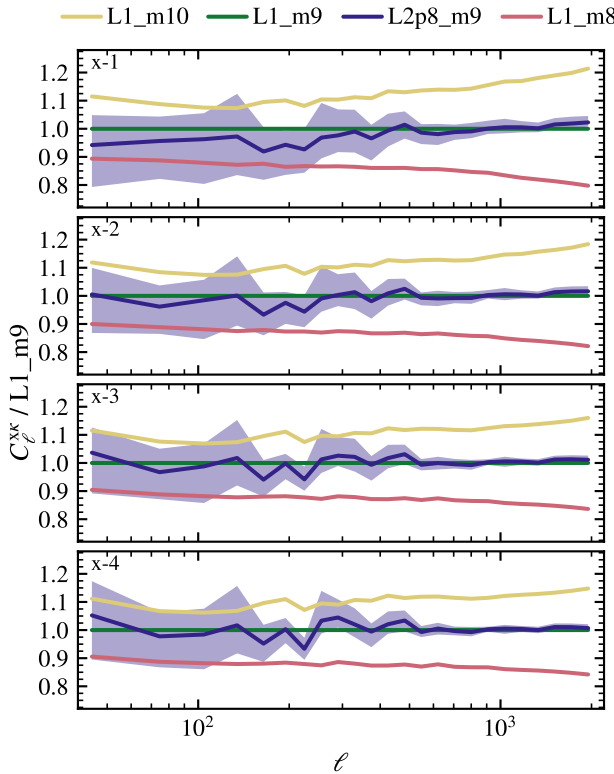


**Figure C3.** The same as lower panel of Fig. 5, but repeated for each tomographic bin, which is indicated in the upper left corner of each panel.

cluster gas fraction (fgas+2 $\sigma$ , fgas-2 $\sigma$  and fgas-8 $\sigma$  respectively) variations of the L1\_m9 simulation. The high resolution (L1\_m8) simulation has a slightly lower gas fraction relative to the fiducial L1\_m9 simulation for halo masses  $M_{500c} \gtrsim 1.5 \times 10^{14} M_\odot$ , i.e., the halo masses which dominate the X-ray component of the cross-correlation (see Fig. 3). Given the X-ray-lensing cross-correlation's clear dependence on cluster gas fraction (as shown in §4.2.2) and the juxtaposition of the fgas-2 $\sigma$  simulation, it should not be a surprise that the predicted cross-correlation for L1\_m8 is suppressed

relative to that of L1\_m9. The minor divergence of L1\_m8 from L1\_m9 occurs for masses above the range that L1\_m8 was calibrated on ( $M_{500c} = 10^{13.5} - 10^{13.75} M_\odot$ ). These same arguments can be extended to describe the elevation of the cross-correlation for the low-resolution simulation (L1\_m10) relative to the fiducial L1\_m9 simulation.

In Fig. D2, we present the X-ray luminosity ( $L_{X,M_{500c}}$ ) – halo mass ( $M_{500c}$ ) relation, where the X-ray luminosity is in the soft band (0.5 - 2.0 keV). The X-ray luminosity – halo mass scaling relations are not identical for each model because of the different hot gas profiles that come from the imperfect recalibration of subgrid prescriptions at each resolution. The layout of Fig. D2 is the same as that of Fig. D1. The X-ray luminosities of haloes with  $M_{500c} \gtrsim 5 \times 10^{14} M_\odot$  in the fgas-2 $\sigma$  and L1\_m8 simulations are very similar for the redshifts shown. Hence, the cross-correlations of the two simulations are similar, because the haloes that dominate the X-ray component of the cross-correlation have similar X-ray luminosities.

## APPENDIX E: MASKING POINT SOURCES

In this appendix we present additional analysis related to the masking of point sources and the impact of unresolved AGN on the measured X-ray-lensing cross-correlation.

Fig. E1 presents the masked fraction of the total X-ray emission from AM AGN (see §3.2.2), for the fiducial L1\_m9 simulation, as a function of the photon flux limit down to which pixels containing AGN are masked. The grey shaded region corresponds to flux limits above that of ROSAT (0.02 photons/s). We repeat this masking of the AM AGN all-sky maps using an  $N_{\text{side}}$  of 8192 (dotted curves), 4096 (dashed curves) and 2048 (solid curves). For each resolution the total X-ray emission on the sky is conserved. Pixels in lower  $N_{\text{side}}$  maps cover a larger area on the sky (e.g. the area of the pixel in steradians  $A_{\text{pixel}} = 4\pi/(12 \times N_{\text{side}}^2)$ ), meaning that, at a fixed flux limit, for every resolved AGN a larger area on the sky is masked and a greater portion of the total X-ray emission on the sky is covered.

In Fig. E2 we examine the effect of varying the photon flux limit used for masking AGN point sources. We recompute the AM AGN contaminated X-ray-lensing cross-correlation for the L1\_m9 simulation in each tomographic bin (indicated in the upper left corner of each panel), but vary the flux limit ( $f_{\text{lim}} = 0.02 \text{ photons/s}$ ) by factors

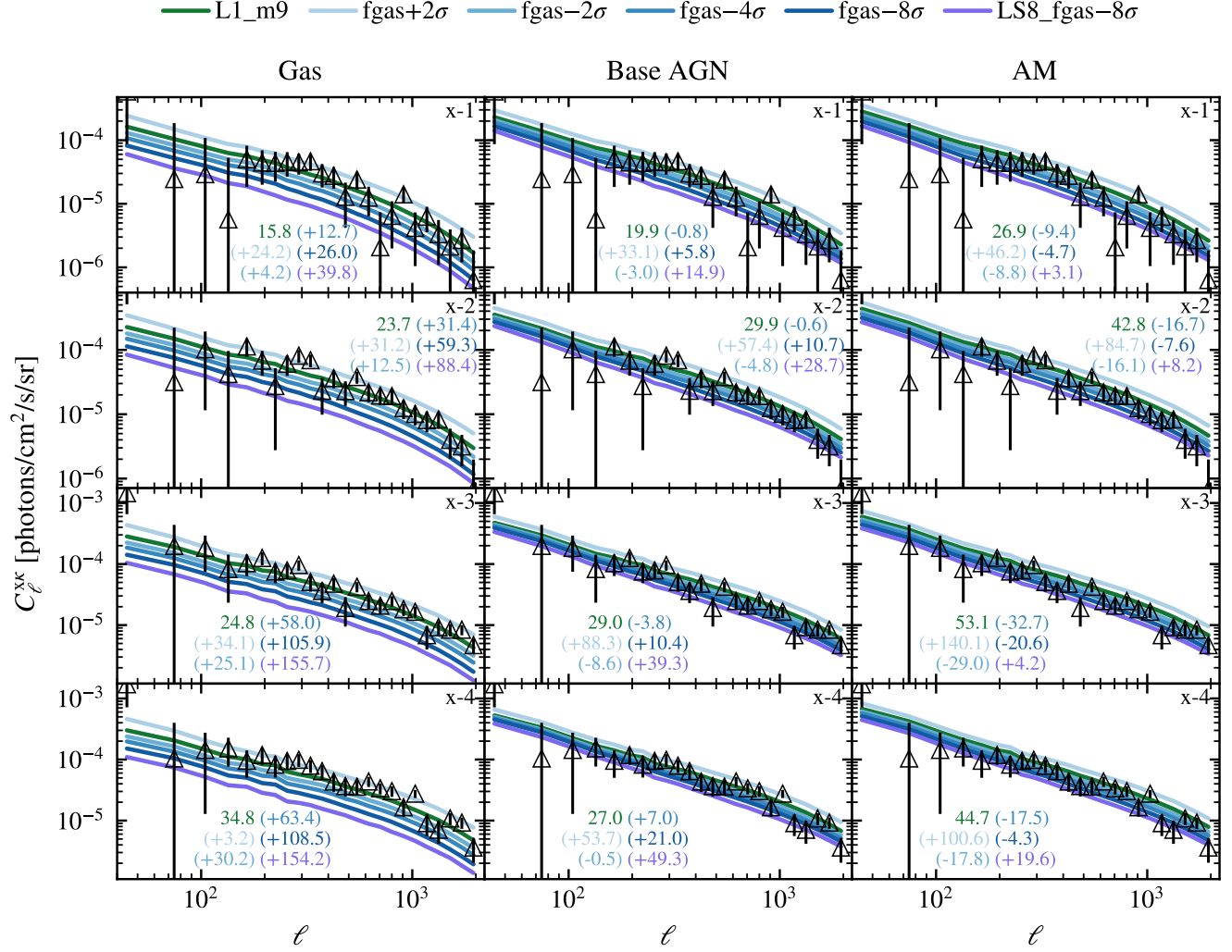


**Figure C4.** The same as Fig. 6, but for each tomographic bin, which is indicated in the top right corner of each panel.

of 10, 1, 0.1 and 0.01 (magenta, black, cyan and gold curves). We compare the X-ray–lensing cross-correlations for when we include X-ray emission from both hot gas and AM AGN to when we only include X-ray emission from hot gas. Reducing  $f_{\text{lum}}$  increases both the number of resolved point sources and the number of masked pixels, which leads to more pixels containing information about the distribution of hot gas being masked. Reducing the flux limit by at least an order of magnitude results in the contaminated cross-correlation having less power than its uncontaminated counterpart for some values of  $\ell$ , implying a net loss of information about the distribution of diffuse gas.

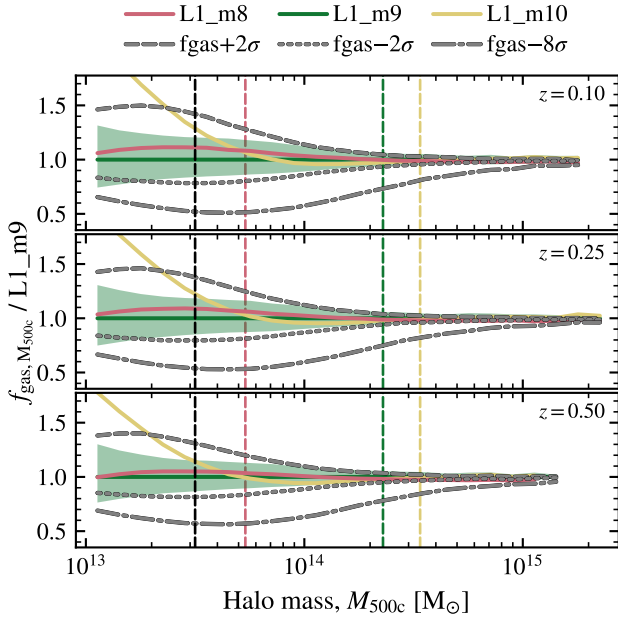


**Figure D1.** The median cluster gas mass fraction within  $R_{500c}$  as a function of halo mass,  $M_{500c}$ , at redshift  $z = 0.1$  (top panel),  $z = 0.25$  (middle panel) and  $z = 0.5$  (bottom panel) for different resolutions and box sizes relative to the result for the L1\_m9 simulation. The shaded region outlines the 16th to 84th percentile scatter of the L1\_m9 simulation. The  $+2\sigma$ ,  $-2\sigma$  and  $-8\sigma$  cluster gas fraction variations of the L1\_m9 simulation are overlaid in grey (dashed, dotted and dot-dashed, respectively). The vertical dashed lines give the lower (black) and upper (coloured) mass bounds used for the calibration of subgrid models to X-ray observations at redshift  $z \approx 0.1$  (Kugel et al. 2023) of each resolution.

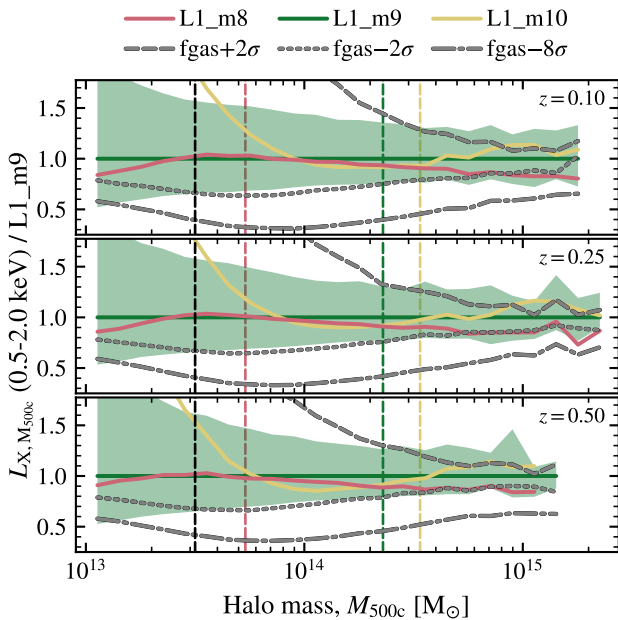


**Figure D2.** As Fig. D1, but for the median soft X-ray luminosity (0.5 - 2.0 keV).

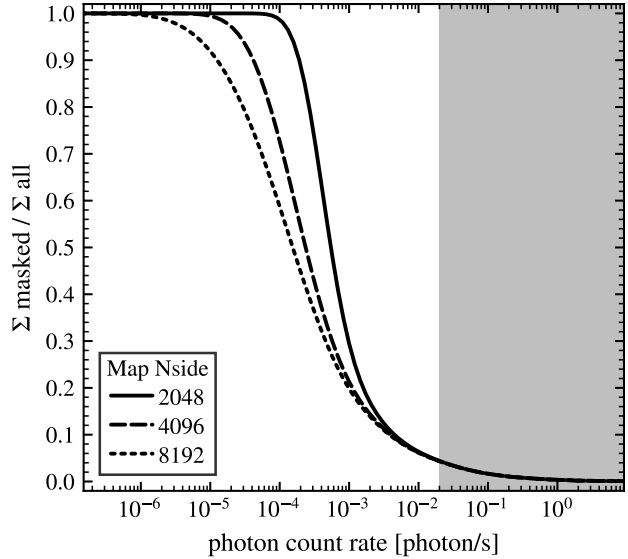


**Figure E1.** The fraction of the total X-ray emission in the all-sky AM AGN map, for the fiducial L1\_m9 simulation, from masked pixels as a function of the photon flux limit. Pixels are masked if they contain an AGN point source above the flux limit. We perform this masking with maps of  $N_{\text{side}} = 8192$  (dotted curves), 4096 (dashed curves) and 2048 (solid curves). The grey shaded region corresponds to flux limits above that of ROSAT (0.02 photons/s).

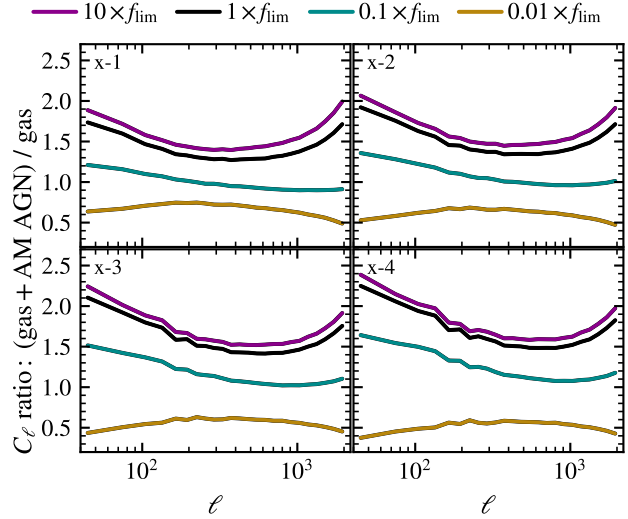


**Figure E2.** The change in ratio between the AM AGN contaminated X-ray-lensing cross-correlation and the gas only cross-correlation, when point sources in the contaminated X-ray all-sky map (with an  $N_{\text{side}} = 2048$ ) are masked for different flux limits. Each panel corresponds to the cross-correlations in a different tomographic bin. The black solid curve corresponds to the ROSAT-like all-sky flux limit ( $f_{\text{lim,RASS}} = 0.02$  photons/s). The coloured curves indicate the effect of multiplying this flux limit by a factor of 10, 0.1 and 0.01 (magenta, cyan, gold), whilst the black dashed curve is for the eROSITA-like flux limit ( $f_{\text{lim,eRASS}} = 5 \times 10^{-14}$  erg s $^{-1}$ ).